

PDF MODELING OF TURBULENT COMBUSTION

AFOSR Grant FA-9550-06-1-0048
Principal Investigator: Stephen B. Pope

Mechanical & Aerospace Engineering
Cornell University
Ithaca, NY 14853

FINAL TECHNICAL REPORT
1/1/2006 – 11/30/2008

Abstract

The overall objective of the research was to advance and extend methodologies for the modeling and simulation of turbulent combustion. Probability density function (PDF) calculations were performed of piloted jet turbulent non-premixed flames to demonstrate the ability of the approach to represent local extinction and re-ignition and to characterize the performance of different sub-models. PDF calculations were performed of lifted flames in vitiated co-flows, and the results were analyzed to show that the stabilization mechanism is auto-ignition. Time-averaging strategies were shown to be very effective in reducing bias in the Monte Carlo methods used to solve the PDF equations. Strategies were developed for implementing combustion chemistry on parallel computers, resulting in speed-ups of up to a factor of five (relative to the straightforward purely-local strategy). The method was shown to scale up to 4096 cores. Algorithms and codes were developed to implement the combined methodology of large-eddy simulation (LES) and filtered density function (FDF). Second-order schemes were developed and demonstrated for particle tracking, which (in contrast to standard methods) also accurately represent the evolution of the particle number density, and second-order accurate splitting schemes were developed for the stochastic differential equations that arise in LES/FDF.

20090429219

REPORT DOCUMENTATION PAGE

Public reporting burden for this collection of information is estimated to average 1 hour per response, including the time for reviewing data needed, and completing and reviewing this collection of information. Send comments regarding this burden estimate or any other aspect of this collection of information, including suggestions for reducing this burden to Department of Defense, Washington Headquarters Services, Directorate for Information Operations and Reports (0704-0188), 1215 Jefferson Davis Highway, Suite 1204, Arlington, VA 22202-4302. Respondents should be aware that notwithstanding any other provision of law, no person shall be subject to any penalty for failing to comply with a collection of information if it does not display a currently valid OMB control number. **PLEASE DO NOT RETURN YOUR FORM TO THE ABOVE ADDRESS.**

1. REPORT DATE (DD-MM-YYYY) 23-2-2009		2. REPORT TYPE Final Performance Report		3. DATES COVERED (From - To) 1-1-2006-31-11-2008	
4. TITLE AND SUBTITLE (U) PDF Modelling of Turbulent Combustion				5a. CONTRACT NUMBER	
				5b. GRANT NUMBER FA9550-06-1-0048	
				5c. PROGRAM ELEMENT NUMBER 61102F	
6. AUTHOR(S) Stephen B. Pope				5d. PROJECT NUMBER 2308	
				5e. TASK NUMBER BX	
				5f. WORK UNIT NUMBER	
7. PERFORMING ORGANIZATION NAME(S) AND ADDRESS(ES) Cornell University Upson Hall Ithaca NY 14853				8. PERFORMING ORGANIZATION REPORT NUMBER	
9. SPONSORING / MONITORING AGENCY NAME(S) AND ADDRESS(ES) AFOSR/NA 875 Randolph St Suite 325, Room 3112 Arlington VA 22203-1768				10. SPONSOR/MONITOR'S ACRONYM(S)	
				11. SPONSOR/MONITOR'S REPORT NUMBER(S)	
12. DISTRIBUTION / AVAILABILITY STATEMENT Approved for public release; distribution is unlimited					
13. SUPPLEMENTARY NOTES					
14. ABSTRACT The overall objective of the research was to advance and extend methodologies for the modeling and simulation of turbulent combustion. Probability density function (PDF) calculations were performed of piloted jet turbulent non-premixed flames to demonstrate the ability of the approach to represent local extinction and re-ignition and to characterize the performance of different sub-models. PDF calculations were performed of lifted flames in vitiated co-flows, and the results were analyzed to show that the stabilization mechanism is auto-ignition. Time-averaging strategies were shown to be very effective in reducing bias in the Monte Carlo methods used to solve the PDF equations. Strategies were developed for implementing combustion chemistry on parallel computers, resulting in speed-ups of up to a factor of five (relative to the straightforward purely-local strategy). The method was shown to scale up to 4096 cores. Algorithms and codes were developed to implement the combined methodology of large-eddy simulation (LES) and filtered density function (FDF). Second-order schemes were developed and demonstrated for particle tracking, which (in contrast to standard methods) also accurately represent the evolution of the particle number density, and second-order accurate splitting schemes were developed for the stochastic differential equations that arise in LES/FDF.					
15. SUBJECT TERMS Propulsion, combustion, PDF methods					
16. SECURITY CLASSIFICATION OF:			17. LIMITATION OF ABSTRACT UL	18. NUMBER OF PAGES 62	19a. NAME OF RESPONSIBLE PERSON Julian M. Tishkoff
a. REPORT Unclassified	b. ABSTRACT Unclassified	c. THIS PAGE Unclassified			19b. TELEPHONE NUMBER (include area code) (703) 696 8478

CONTENT

EXECUTIVE SUMMARY	3
RANS/PDF CALCULATIONS OF TURBULENT FLAMES	4
PDF CALCULATIONS OF PILOTED JET FLAMES.....	4
PDF CALCULATIONS OF LIFTED TURBULENT FLAMES	7
TIME-AVERAGING STRATEGIES IN PDF METHODS.....	8
EFFICIENT PARALLEL IMPLEMENTATION OF IN SITU ADAPTIVE TABULATION	9
ALGORITHMS FOR LES/FDF	10
ACCURATE PARTICLE TRACKING	10
TIME SPLITTING SCHEMES	14
PUBLICATIONS.....	16
OTHER REFERENCES	16
PERSONNEL SUPPORTED.....	18
DEGREES GRANTED	18
MEETING PARTICIPATION	18
INTERACTION WITH AFRL	19
TECHNOLOGY TRANSITIONS AND TRANSFERS.....	20
HONORS AND AWARDS	20
INVENTIONS AND PATENTS	20

EXECUTIVE SUMMARY

In both space and aircraft applications, the design of combustors in propulsion systems remains a significant technical challenge. Given the cost, difficulty, and time consumed in experimental testing, it is recognized well that computer modeling is essential to exploring different design concepts and to reducing the cost and time of the design cycle. While many phenomena may be involved – sprays, radiation, combustion dynamics, etc. – a central problem is that of modeling turbulent-chemistry interactions in turbulent combustion. The PDF approach to turbulent combustion has the advantages of fully representing the turbulent fluctuations of species and temperature and of allowing realistic combustion chemistry to be implemented (e.g., of order 50 species). This methodology also is being applied in conjunction with large-eddy simulations, in which case it is referred to as LES/FDF.

The research performed and findings obtained are summarized here and given in more detail in the subsequent sections and in the listed publications.

Turbulent flames were studied using probability density function (PDF) methods. The influence of the mixing sub-models was investigated for a series of piloted jet non-premixed flames. Only one of the frequently used models (EMST, Subramaniam & Pope 1998) was capable of predicting the correct levels of both the degree of local extinction and the level of turbulent fluctuations.

A Lagrangian study of the performance of different turbulent mixing models was performed for lifted jet flames in vitiated co-flows. This study revealed that the stabilization mechanism in these flames is autoignition, following the turbulent mixing of the jet and coflow. In contrast to conventional lifted flames, no diffusive transport against the flow was needed for stabilization.

Computational algorithms were developed to accelerate parallel combustion chemistry calculations. For serial calculations, the method of *in situ* adaptive tabulation (ISAT) was able to accelerate chemistry calculations by three orders of magnitude. For parallel computations there were serious load-balancing problems. Several different algorithms were implemented and evaluated, which partially resolved this problem. Speed-ups of up to five were obtained, and scalability to at least 4096 cores.

Advances have been made in the development of accurate and efficient computational algorithms for PDF and LES/FDF methods. Time-averaging strategies in PDF methods were shown to be very effective in reducing the bias error. New interpolation schemes and a modified Runge Kutta scheme were shown to yield superior performance for particle tracking in LES/FDF. These schemes are second-order accurate in time and space and cause the particle number density to evolve accurately. Second-order accurate splitting schemes were developed for the stochastic differential equations that arise in LES/FDF.

The grant provided support for the PI and for three Ph.D. students: Liuyan Lu, Haifeng Wang and Pavel Popov. Lu received her Ph.D. in 2008.

RANS/PDF CALCULATIONS OF TURBULENT FLAMES

PDF CALCULATIONS OF PILOTED JET FLAMES

The Barlow & Frank (1998) piloted jet flames are recognized well as providing an excellent test of turbulent combustion models, in particular of their ability to describe local extinction and re-ignition. There is a sequence of flames *A–F*, with *D*, *E*, and *F* being fully turbulent, with increasing amounts of local extinction. While there are many successful modeling studies of flame *D* – which has little local extinction – there are far fewer modeling studies for the more challenging flames *E* and *F*.

PDF methods previously have been applied successfully to these flames by the Cornell group (Xu & Pope, 2000, Tang *et al.*, 2000) and the Imperial College group (Lindstedt *et al.*, 2000). Both groups reported accurate calculations of these flames but with different sub-models. The former calculations use an augmented reduced mechanism based on the GRI mechanism and the EMST mixing model with model constant $C_\phi = 1.5$. The latter calculations use Lindstedt's reduced mechanism and the modified Curl mixing model with model constant $C_\phi = 2.3$. Since the two groups use different mixing models and different chemical mechanisms, questions arise as to the dependence and sensitivity of the calculations to these ingredients. Some progress has been made in understanding the relative behavior of the different mixing models (see, e.g., Ren & Pope 2004). We now have concluded a series of PDF calculations addressing these issues. Cao & Pope (2005) describe joint PDF calculations of these flames using 7 different chemical mechanisms for methane, ranging from a 5-step reduced mechanism to the 53-species GRI 3.0 mechanism. The results show that the GRI mechanisms (and the augmented reduced mechanisms based on them) are capable of accurately representing the observed local extinction and re-ignition. In contrast, C_1 skeletal mechanisms and 5-step reduced mechanisms prove to be inaccurate. (Lindstedt's mechanism was not included in the study due to its lack of availability at the time.)

This work has been followed up by a study (Cao *et al.* 2006) of the influence of the turbulent mixing models used in the PDF model calculations. The principal finding is that (with a different value of the mixing-model constant) all three commonly used models (IEM, MC and EMST) are capable of yielding the observed level of local extinction, but only the EMST model produces, simultaneously, the observed level of mixture fraction fluctuations.

After Lindstedt's mechanisms became available publicly on the TNF workshop website (<http://public.ca.sandia.gov/TNF/chemistry.html>), we further investigated the apparent discrepancies in previous PDF model calculations of the Barlow & Frank flames (Wang and Pope, 2007). A comparison is made between non-premixed flame calculations using the GRI 3.0 and Lindstedt detailed mechanisms and with different mixing models. Additional insights are provided by autoignition and non-premixed strained laminar flame calculations. Figure 1 shows the ignition delay times given by different mechanisms for a stoichiometric methane/air mixture as a function of the initial temperature. For temperatures above 1,400K, the Lindstedt mechanism exhibits a shorter ignition delay time. A series of calculations was performed of strained non-premixed laminar flames with the same fuel and oxidant used in the Barlow & Frank flames (i.e., the fuel-air ratio is 1:3 methane/air, and the oxidant is air). Figure 2 shows

the peaks of various quantities in these flames as functions of the imposed strain rate. While the Lindstedt and GRI mechanisms yield comparable properties at low strain rates, the Lindstedt mechanism exhibits a greater resilience to extinction.

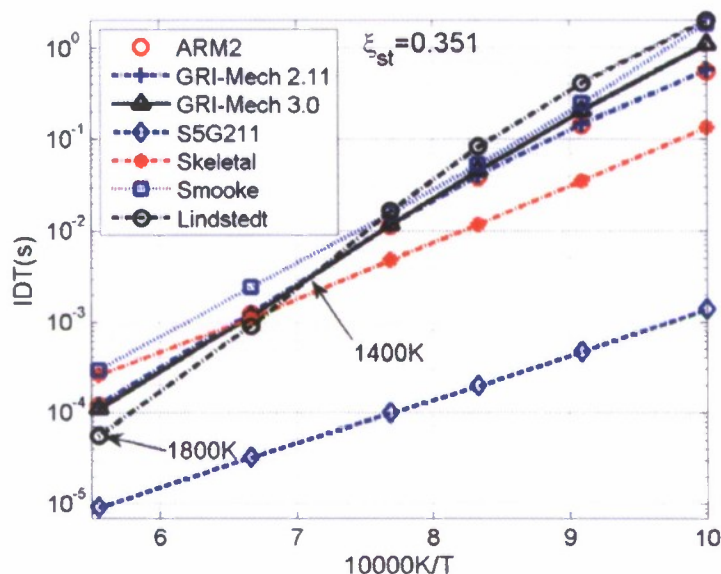


Figure 1 Ignition delay times (IDTs) of different mechanisms at different initial temperatures T .

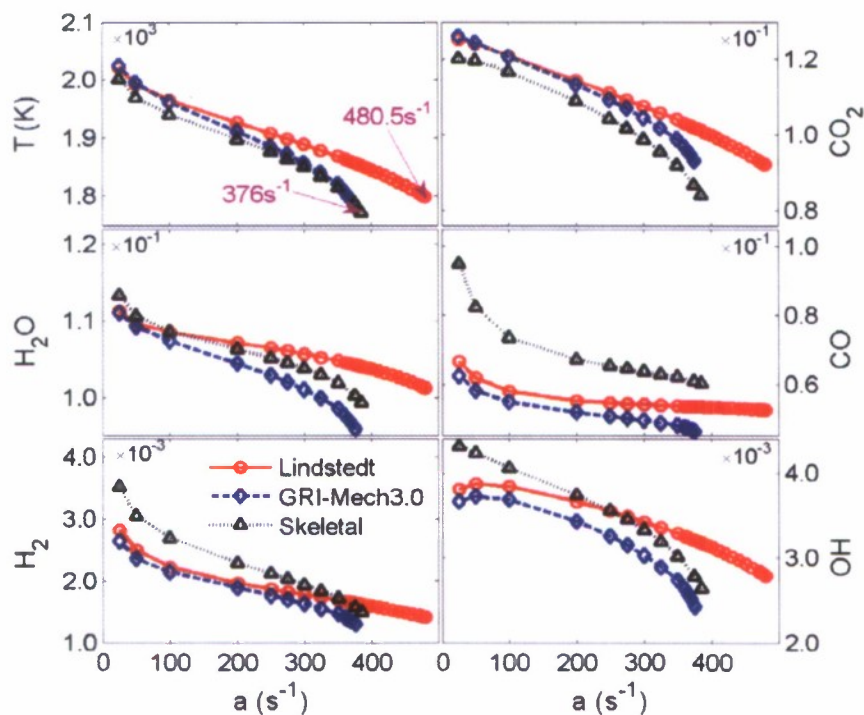


Figure 2 The peak values of the temperature and the mass fractions of CO_2 , H_2O , CO , H_2 , and OH against the nominal strain rate a in the opposed laminar jet non-premixed flames computed with different reaction mechanisms.

A set of 28 PDF calculations of the Barlow & Frank flames have been performed, with both chemical mechanisms, three mixing models, and a range of values of the mixing model constant C_ϕ . Figure 3 shows some of the results on “burning indices” (BIs) at an axial location of 7.5 fuel jet diameters. (The burning index is zero for complete extinction and one for complete combustion.) There are two fundamental observations from these results. First, for a given mixing model and value of C_ϕ , the Lindstedt mechanism uniformly yields higher values of BI than does the GRI mechanism. This result is consistent with the previously observed shorter ignition delay time and higher extinction strain rate of the Lindstedt mechanism. Second, the two calculations closest to those of Xu & Pope (2000) and Lindstedt et al. (2000) (i.e., GRI, EMST, $C_\phi = 1.5$ and Lindstedt, modified Curl, $C_\phi = 2.3$) yield very similar values of BI, which are generally in agreement with the experimental data (though less so for H_2O and OH). This result, then, provides a full explanation for the similar calculations in 2000 using different submodels.

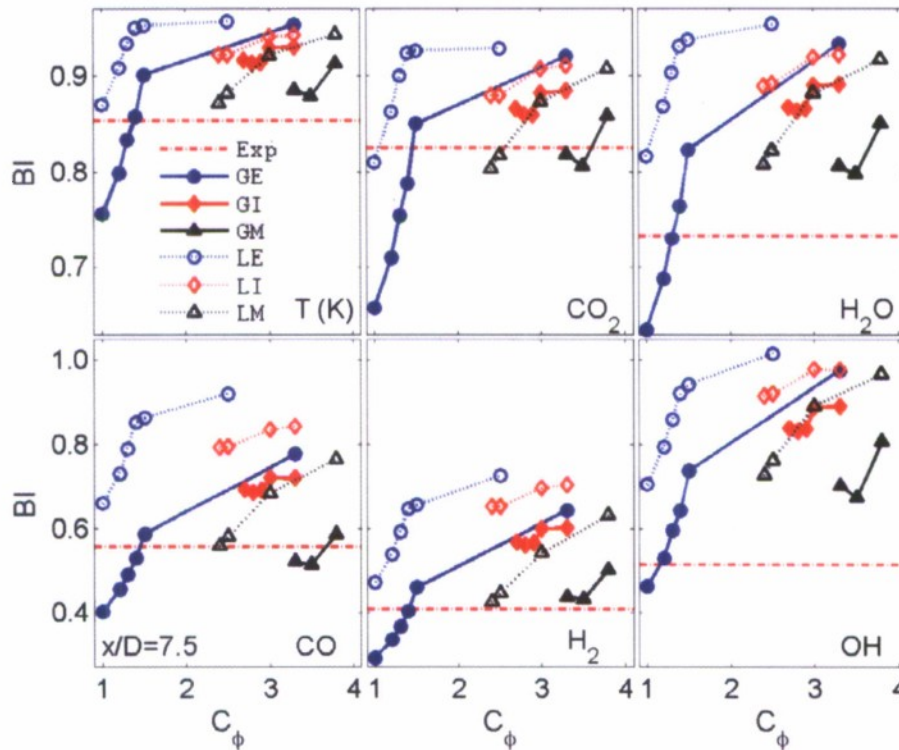


Figure 3 The burning indices of the temperature and the mass fractions of CO_2 , H_2O , CO , H_2 , and OH against C_ϕ at the location of $x/D = 7.5$ in the Sandia flame. The two letters in the legend identify the combination of the mixing models (E: ESMT, I: IEM, and M: modified Curl) and the reaction mechanisms (G: GRI-Mech 3.0, L: Lindstedt mechanism).

The present work reveals significant differences in the predictions of the two mechanisms but does not determine which (if either) is accurate under the conditions investigated. There are experimental data for non-premixed laminar flame with the flame E fuel (methane/air mixture Barlow *et al.* 2001), but these are at very low strain rates. It would be extremely valuable to

investigate experimentally the properties of strained laminar flames of this fuel close to the extinction strain rate.

It was claimed later by Lindstedt (private communication) that the Lindstedt mechanism provided on the TNF web site and used in the above investigation includes incorrect specifications of reaction parameters. As a consequence, the above conclusions on the comparison between the GRI and the Lindstedt mechanisms are compromised. The difference between the two sets of PDF calculations in 2000 unfortunately remains unexplained, and further investigation is needed.

PDF CALCULATIONS OF LIFTED TURBULENT FLAMES

In laboratory experiments on turbulent flames, for obvious reasons, air at atmospheric conditions generally is used as the oxidant. In practical applications, however, the re-circulating flows used for flame stabilization generally lead to some mixing between the air stream and hot combustion products, and in thrust augmentors the oxidant stream is simply the lean combustion products from the turbine.

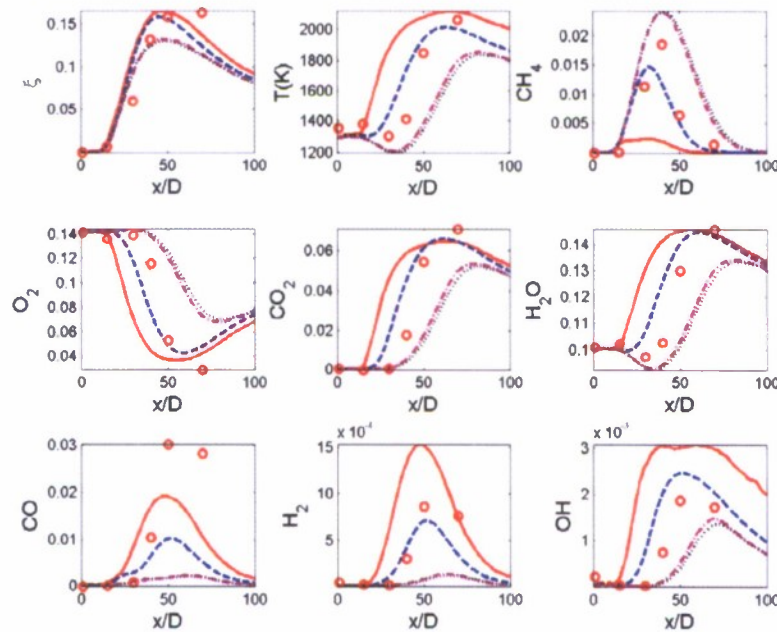


Figure 4 Axial profiles (off the axis at $r=15\text{mm}$) of mean mixture fraction, temperature, and mass fractions of CH_4 , O_2 , CO_2 , H_2O , CO , H_2 and OH . Symbols: Measurement by Cabra *et al.* 2005; Solid lines: Joint PDF calculations with ISAT error tolerance $\varepsilon_{\text{etol}} = 5 \times 10^{-4}$; Dashed lines: $\varepsilon_{\text{etol}} = 1 \times 10^{-4}$; Dash-dotted lines: $\varepsilon_{\text{etol}} = 1 \times 10^{-5}$; Dotted lines: $\varepsilon_{\text{etol}} = 5 \times 10^{-6}$.

Motivated by these observations, a series of experiments has been performed (at Berkeley, Sandia, and Sydney) on various jet flames in vitiated co-flows. Previously we have performed two PDF studies of the lifted hydrogen flames studied experimentally by Cabra *et al.* (2002). These two studies are based on the composition PDF method incorporated in Flucnt (Masri *et al.*

2004) and on the velocity-frequency-composition joint PDF method (Cao, Popc & Masri 2005). In both cases, detailed 9-species mechanisms for hydrogen arc used.

In this study, we investigate the lifted methane flames studied by Cabra *et al.* (2002, 2005). The calculations are based on the joint PDF method used previously, with the modified Curl mixing model and the ARM1 mechanism. Figure 4 shows the comparison between experimental data and PDF results with different values of the ISAT (Popc, 1997) error tolerance. In order to obtain accurate PDF results of the lifted methane flames, the ISAT error tolerance needs to be decreased to at least $\varepsilon_{\text{etol}} = 1 \times 10^{-5}$ for these flames. Similar to the lifted hydrogen flames, strong sensitivity of the results to the coflow temperature is observed in the calculations.

TIME-AVERAGING STRATEGIES IN PDF METHODS

Computationally, PDF methods usually are implemented using Lagrangian particle Monte Carlo methods. With N being the number of particles used, these methods incur a statistical error of order $N^{-1/2}$ and a bias error of order N^{-1} . At first sight, the statistical error appears dominant; however, unlike the bias, the statistical error has zero mean, and for statistically-stationary problems it can be reduced at will by time averaging. Hence, in PDF methods, bias can be the more serious source of numerical error.

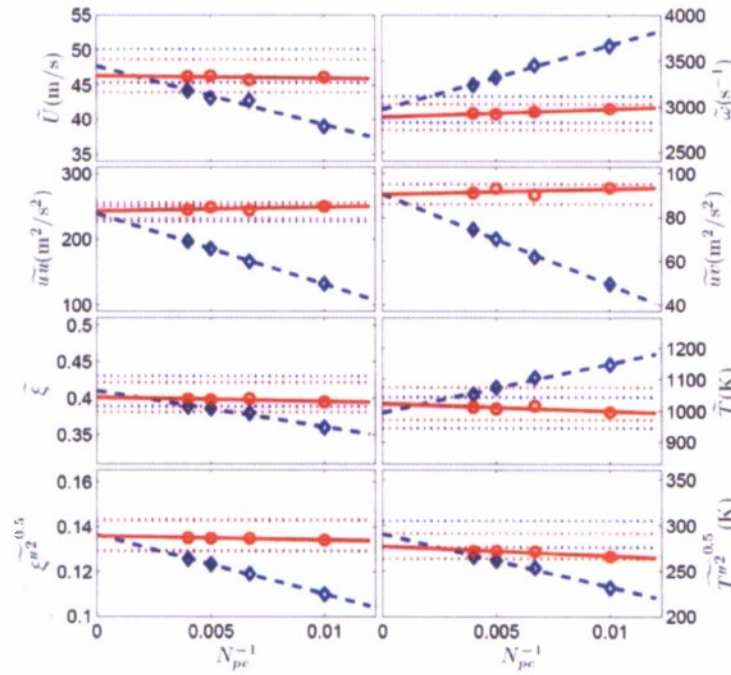


Figure 5 The means of the axial velocity U , the turbulence frequency ω , the Reynolds stresses uu and uv , and the means and rms of the mixture fraction and temperature against N_{pc}^{-1} at the location of $(15D, 1D)$ in the Cabra lifted H_2/N_2 jet flame. Circles, with time-averaging; diamonds, without time-averaging

Wang & Pope (2008b) show how the bias can be reduced dramatically in the velocity-composition PDF method. In this approach the PDF considered is for the fluctuating component of velocity (and composition). A correction is applied to enforce the consistency condition that the mean of the velocity fluctuation is zero. This correction can be applied based either on the

instantaneous mean of the fluctuating particle velocities or on the time average of this quantity. As demonstrated, the use of time averaging all but eliminates the substantial bias which is otherwise incurred.

EFFICIENT PARALLEL IMPLEMENTATION OF IN SITU ADAPTIVE TABULATION

The PDF method calculations presented above demonstrate current capabilities, e.g., using a mechanism with order 50 species. Such calculations are possible because of the ISAT algorithm (Pope 1997) and the availability of parallel computers. As we work towards combining PDF methods with large eddy simulation (LES), larger parallel clusters are needed, and the efficient parallel implementation of ISAT becomes crucial.

If there are P processors, then the load associated with solving the LES equations is balanced well if the solution domain is partitioned into P sub-domains, each containing approximately the same number of cells. Further, with such a decomposition, the computational particles used in the PDF algorithm are distributed approximately equally among the processors; hence, there is good load balancing of particle tracking and of mixing. The load associated with reaction (i.e., incrementing the particle compositions due to reaction over the time step) that can dominate the CPU time can be poorly balanced. For example, the particles on one processor may be inert (e.g., cold air) and hence require negligible time to evaluate their reaction, whereas the particles on another processor may be highly reactive. Even using ISAT, reactive particles take much longer to treat, especially if retrieving from a full table is not possible; hence, a direct integration of the stiff ODEs is required.

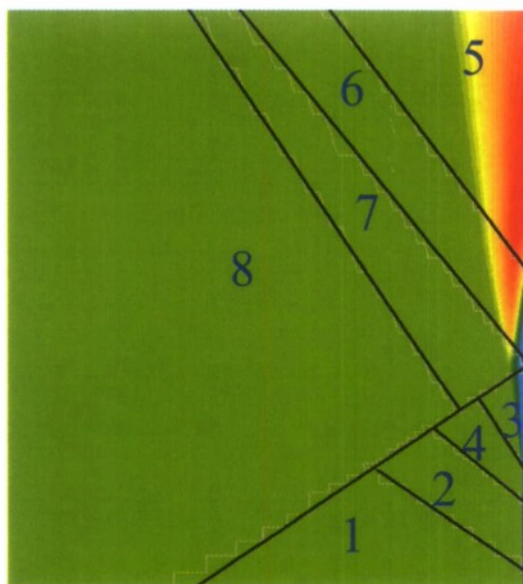


Figure 6 Contour plot of mean temperature in PDF calculations of a lifted hydrogen jet flame, showing the sub-domains used in the Fluent parallel computation.

Following the preliminary work of Lu *et al.* (2005), we are continuing to develop and evaluate parallel strategies for implementing ISAT. One of the test problems considered is the composition PDF method in Fluent applied to the lifted hydrogen jet flame described above. Figure 6 shows the solution domain and its decomposition into the eight sub-domains used in the

parallel computation (using 8 processors). Figure 7 shows the CPU and wall-clock times per particle step required by three different parallel strategies. The first is PLP (purely local processing) in which no message passing is performed, but each processor invokes ISAT independently for all of the particles in its sub-domain. As may be seen from the CPU times, there is considerable load imbalance with processor 6 requiring significantly more time. The corresponding sub-domain is the base of the flame, which involves the most challenging ignition chemistry. The two (non-trivial) parallel strategies lead to speed-ups (relative to PLP) of about 2.5 and 5.

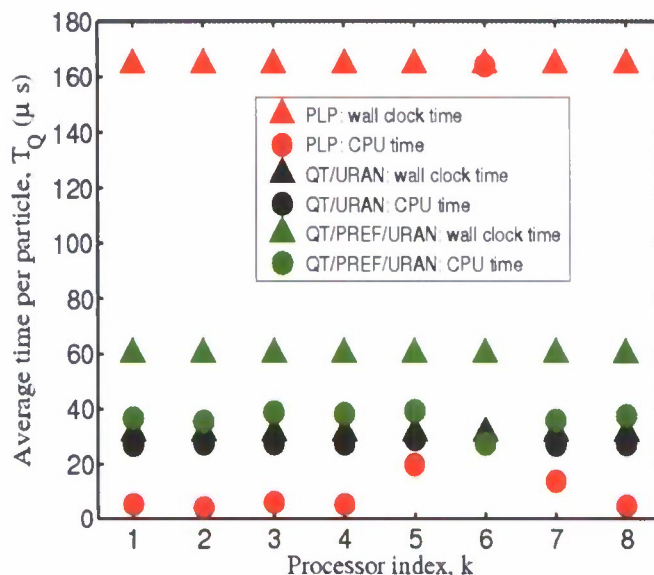


Figure 7 Average wall clock and CPU times (per particle per reaction fractional step) for parallel Fluent computations of the lifted hydrogen flame, with different parallel ISAT strategies.

An adaptive pairing algorithm (Lu *et al.*, 2008) balances the cost of direct evaluations and the communication time for distributing particles among processors. This algorithm performs groupings of processors based on the probability of retrieving from those ISAT tables, the cost of distributing the particles, and the cost of performing direct evaluations. Particles are distributed among the processors in the groups using the aforementioned parallel strategies. Partially-stirred reactor test cases have shown functionality and scalability on up to 4,096 cores on Ranger at the Texas Advanced Computing Center.

ALGORITHMS FOR LES/FDF

The bulk of the research effort has been devoted to developing algorithms and code for the application of the LES/FDF approach to turbulent flames. Here we report two important algorithms in FDF, namely accurate tracking of particles through a given velocity/diffusivity field and weak second-order time splitting schemes for solving the particle stochastic differential equations. The development and testing of the in-house FDF code is close to being finished and will be brought to the full LES/FDF studies of turbulent combustion soon.

ACCURATE PARTICLE TRACKING

One important issue in LES/FDF numerical methods is the consistency between particle number density, which can be thought of as the expected number of particles in a unit volume, and the LES filtered density. To ensure the validity of the LES/FDF methodology, these two redundant forms of density must be equal. It is because of this fact that particle tracking schemes that preserve the consistency between these two fields, either explicitly or implicitly, have received much attention in recent years.

To illustrate the issues and advances made, we consider the simplest case of fluid particles that move according to an incompressible velocity field, $\mathbf{U}(\mathbf{x}, t)$, with no turbulent diffusivity. This problem, albeit being a simplification from the general stochastic differential equation that governs particle transport (see Eqs. (6) and (7) below), is important in the LES/FDF context, where a significant part of the turbulent transport is carried out by the resolved velocity field. The particle position $\mathbf{X}(t)$ evolves by the ODE

$$\frac{d\mathbf{X}(t)}{dt} = \mathbf{U}(\mathbf{X}(t), t) \quad (1)$$

Let $q(\mathbf{x}, t)$ denote the particle number density, and let this be initially uniform, $q(\mathbf{x}, 0) = q_0$. Just like the fluid density, the particle number density satisfies the conservation equation.

$$\frac{\partial q}{\partial t} + \nabla \cdot (q\mathbf{U}) = 0, \quad (2)$$

which can be re-expressed as

$$\left(\frac{\partial}{\partial t} + \mathbf{U} \cdot \nabla \right) \ln q = -\nabla \cdot \mathbf{U} \quad (3)$$

Thus, given $\nabla \cdot \mathbf{U} = 0$, it follows that an initially uniform distribution remains uniform.

The above results pertain to an exact implementation. In practice the velocity field is represented discretely on a grid, and Eq. (1) is integrated numerically, with $\mathbf{U}(\mathbf{X}(t), t)$ being approximated by some interpolation. Consider 2D for simplicity, and suppose that (as is usually the case) bilinear interpolation is used. This interpolation scheme implies that the velocity experienced by the particles inside each grid cell is of the form

$$\begin{aligned} u &= u_0 + u_x x + u_y y + u_{xy} xy, \\ v &= v_0 + v_x x + v_y y + v_{xy} xy. \end{aligned} \quad (4)$$

Evidently, the implied velocity divergence is

$$\nabla \cdot \mathbf{u} = \frac{\partial u}{\partial x} + \frac{\partial v}{\partial y} = u_x + u_{xy} y + v_y + v_{xy} x, \quad (5)$$

Which, in general (i.e., $u_{xy} \neq 0, v_{xy} \neq 0$), cannot be zero.

Figure 8 shows the result of a simple test in which particles (initially uniform) are tracked through an incompressible velocity field using bilinear interpolation. Clearly, the non-zero velocity divergence experienced by the particles leads to a decidedly non-uniform distribution.

To overcome this problem, McDermott & Pope (2008) devised a “parabolic edge reconstruction method” of interpolation (PERM) that (for the case considered) yields an interpolated velocity field of zero divergence; thus, if the fluid particles are advanced accurately in time, the uniform initial distribution is preserved.

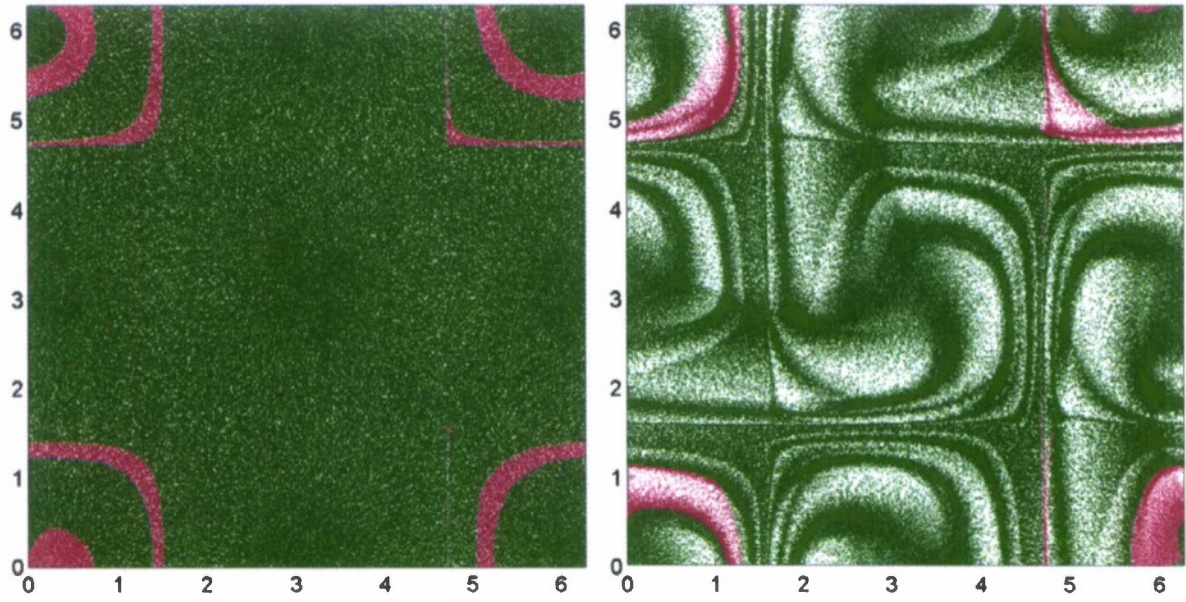


Figure 8 Left: Exact solution for an incompressible 2D flow. Right: numerical solution for the same flow, using bilinear velocity interpolation

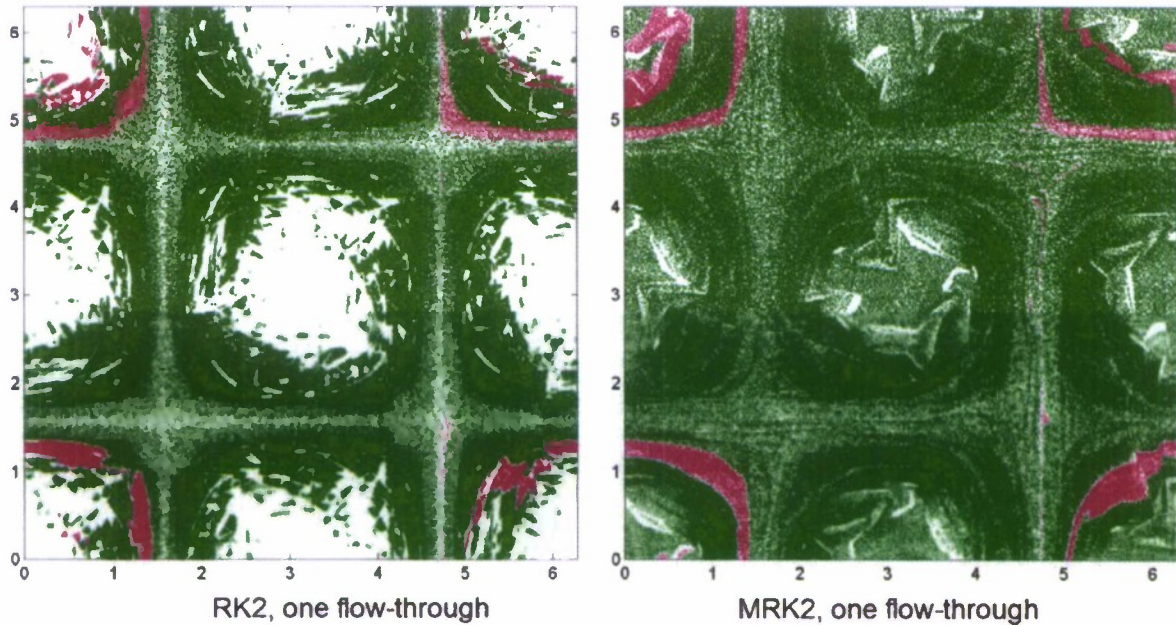


Figure 9 Particles tracked through a 2D incompressible flow field using PERM interpolation and (a) (left) second-order Runge-Kutta (b) (right) MRK2. The Courant number is 1.0. In both cases the non-uniformity decreases as the Courant number decreases.

The PERM velocity field, by construction, has excellent divergence properties; however, it also results in small velocity discontinuities between cells (that decrease quadratically as the cell size is decreased). It follows that a standard numerical scheme for integrating Eq. (1) reverts to first-order accuracy in the time step Δt (because of the discontinuities). To remedy this problem, Popov *et al.* (2008) have devised a modified Runge-Kutta scheme (MRK2) that restores second-order accuracy even with the type of discontinuity caused by PERM. Figure 9 shows the particle

distribution for a test case using (a) standard second-order Runge-Kutta, and (b) MRK2. As may be seen, MRK2 results in a much more uniform number density.

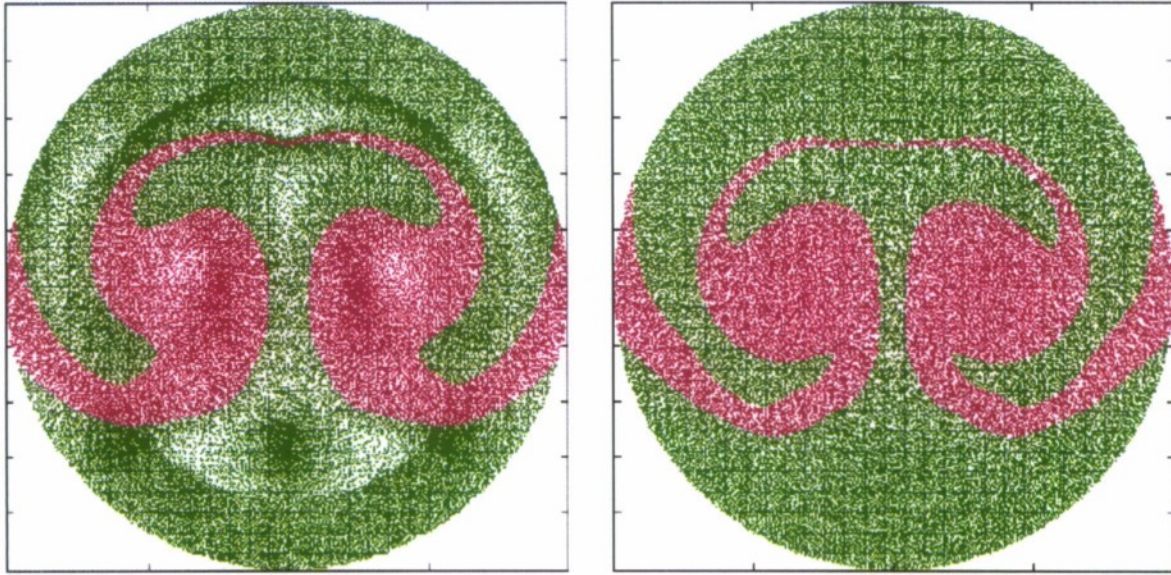


Figure 10 Left: Solution for an incompressible flow on a circular domain, using bilinear velocity interpolation in polar coordinates. Right: Solution for the same flow using the PPERM velocity reconstruction

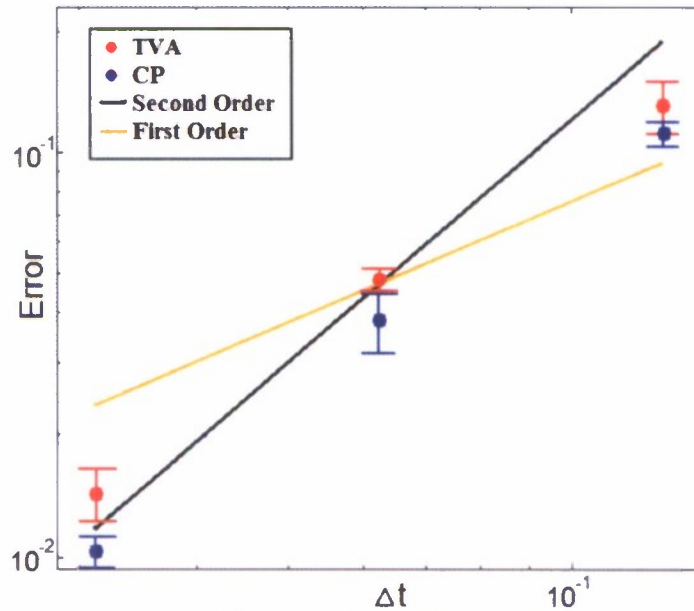


Figure 11 Overall numerical error of the particle tracking scheme, composed of the velocity and scalar interpolation schemes, and the SDE time integration schemes developed by Cao and Pope (CP, red dots), and Tocino and Vigo-Aguiar (TVA, blue dots). The vertical bars represent 95% confidence intervals.

Because a cylindrical grid is the most natural choice for many turbulent combustion simulations, recent efforts have included the adaption of the PERM velocity reconstruction algorithm (that is designed for Cartesian grids) to cylindrical grids. Because such a grid is inherently singular at its axis, care must be taken to avoid singularities in the reconstructed velocity, or else a decrease in

the order of accuracy of the scheme is suffered, close to the grid axis. The new, polar version of PERM (called PPERM), avoids these complications and yields an interpolated velocity field whose accuracy and regularity properties are identical to those of PERM. The performance of the PPERM scheme is depicted on Figure 10, which shows results from a test analogous to the one illustrated on Figure 9, performed on a circular domain.

Additional efforts in particle tracking have included testing of the overall accuracy of the combination of interpolation and time advancement schemes for the general, stochastic particle tracking problem. In the majority of composition LES/FDF methods, the particle positions evolve by the stochastic differential equation

$$d\mathbf{X}(t) = \left(\mathbf{U} + \frac{\nabla \Gamma}{\tilde{\rho}} \right) dt + \sqrt{\frac{2\Gamma}{\tilde{\rho}}} d\mathbf{W} \quad (6)$$

where Γ is the effective diffusivity, $\tilde{\rho}$ is the LES filtered density, the final term in Eq. (6) has the standard meaning of integration with respect to a Wiener process. Velocity is interpolated with the PPERM reconstruction scheme, and the diffusivity and density fields are interpolated with a third-order accurate scheme, called the multilinear gradients (MLG) scheme. Two alternative SDE time advancement schemes, developed respectively by Cao and Pope (2003) and Tocino and Vigo-Aguiar (2002), have been tested, and results have been reported by Popov and Pope (2008). As can be seen on Figure 11, the overall scheme attains the desired second-order accuracy using either of these SDE schemes.

TIME SPLITTING SCHEMES

The Lagrangian Monte Carlo particle methods (Pope, 1985) are the most efficient numerical algorithm to solve PDF/FDF transport equations. In these methods, the continuous PDF is discretized by a finite number of nominal particles, and each particle is governed by a system of stochastic differential equations (SDE) as follows (including an Ito SDE for particle position and a scalar random equation) to describe the underlying physical and chemical processes.

$$\begin{cases} d\mathbf{X}(t) = \mathbf{D}(\mathbf{X}(t), t) dt + b(\mathbf{X}(t), t) d\mathbf{W}(t), \\ d\phi(t) = \mathbf{A}(\mathbf{X}(t), \phi(t), t) dt, \end{cases} \quad (7)$$

where $\mathbf{X}(t)$ and $\phi(t)$ are particle position and scalars (e.g., species mass fractions and enthalpy), $\mathbf{D}(\mathbf{X}(t), t)$ and $b(\mathbf{X}(t), t)$ denote drift and diffusion in physical space, and $\mathbf{A}(\mathbf{X}(t), \phi(t), t)$ denotes rate of change of scalars (e.g., production rate of species or heat release rate). Eq. (6) is a specific version of the Ito SDE in Eq. (7), with $\mathbf{D}(\mathbf{X}(t), t) = (\mathbf{U} + \nabla \Gamma / \tilde{\rho})$ and $b(\mathbf{X}(t), t) = \sqrt{2\Gamma / \tilde{\rho}}$.

To solve the coupled SDE system (7) accurately, special care is needed. All the well developed high-order ODE schemes are not applicable to this system. No second-order time splitting schemes have been developed previously for this system and have been applied in the RANS/PDF or LES/FDF practice.

A class of weak second-order time splitting schemes is developed in Wang *et al.* (2008). Four primary contributions are made in this work:

- I. Establish that the coefficients in (7) can be frozen at the mid-time while preserving second-order accuracy. The use of frozen coefficients avoids any interpolation of the coefficients in time when using different SDE schemes, and greatly simplifies the

solution algorithms. Moreover, it guarantees the applicability of many autonomous SDE schemes to (7).

- II. Examine the performance of three existing schemes for integrating the SDE for particle position: the mid-point scheme of Cao and Pope (2003); the predictor-corrector scheme of Kloeden and Platen (1992); and the Runge-Kutta scheme of Tocino and Vigo-Aguiar (2002). The latter two are derivative-free schemes, and the Kloeden and Platen scheme is for autonomous SDEs only.
- III. Develop and evaluate different time splitting schemes (that treat particle motion, reaction, and mixing on different sub-steps). The second-order accuracy of the schemes is verified by the test cases.
- IV. Develop the method of manufactured solutions (MMS) (Roache, 2002) to assess the convergence of Monte Carlo particle methods. This method is a general way of generating test cases with analytical solutions. The MMS method is used to demonstrate the convergence and order of accuracy of the developed splitting schemes.

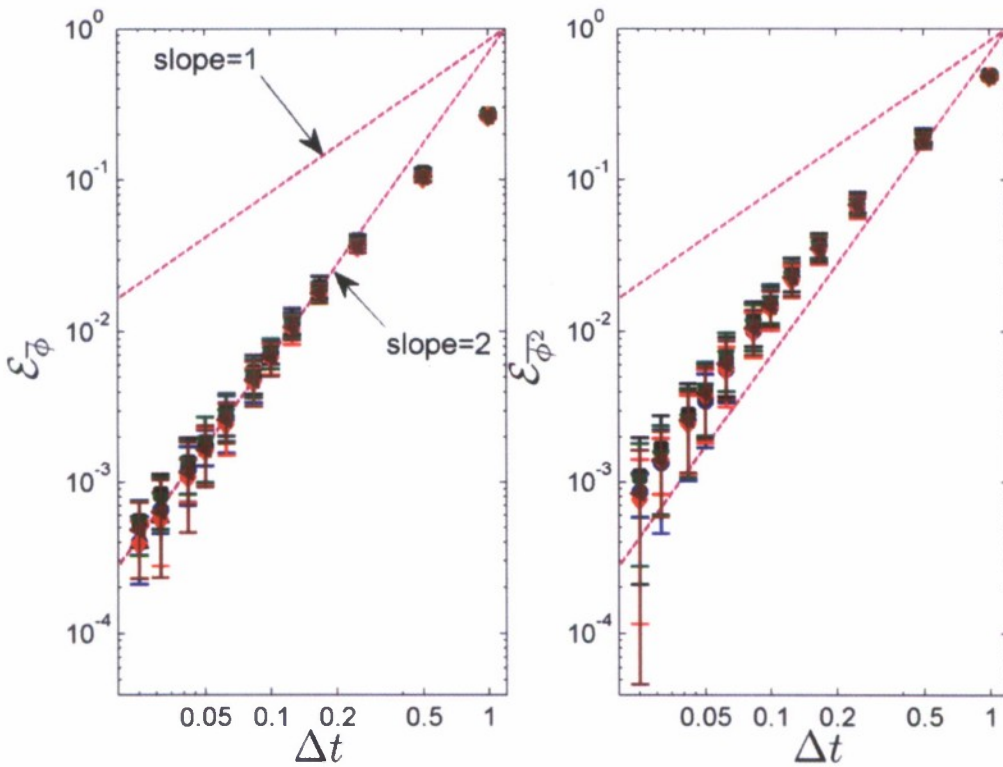


Figure 12 The convergence of the errors of scalar mean $\varepsilon_{\bar{\phi}}$ and scalar square mean $\varepsilon_{\bar{\phi}^2}$ against the time step Δt for splitting of type Mix-Tran-React-Tran-Mix combined with the Cao and Pope scheme (circles), with the Cao and Pope scheme with frozen coefficients (diamonds), with the Tocino and Vigo-Aguiar scheme (squares), with the Tocino and Vigo-Aguiar scheme with frozen coefficients (down triangles), and with the Kloeden and Platen scheme with frozen coefficients (left triangles). (The error bars indicate 95% confidence intervals.)

Different splitting schemes with or without freezing the coefficients are compared. In general, freezing the coefficients reduces the numerical errors. Otherwise no significant differences are observed in the performance of the different SDE schemes and splitting schemes. Figure 12 shows the comparison of one type of splitting (Mix-Tran-React-Tran-Mix, which means taking

half step of mixing first, then half step of transport, and full step of reaction, then another half step of transport followed by another half step of mixing) with different SDE schemes and with or without freezing the coefficients. All the schemes shown on the plot demonstrate second-order convergence with respect to time step size, and the difference among the different schemes is small.

PUBLICATIONS

The following papers stemming from the current AFOSR program were written or published in 2006-08. (They are available in pdf format at <http://eccentric.mae.cornell.edu/~tcg/pubs.html>.)

- [1] B. Merci, D. Roekaerts, B. Naud and S.B. Pope (2006) "Comparative study of micro-mixing models in transported scalar PDF simulations of turbulent non-premixed bluff body flames," *Combustion and Flame*, 146, 109-130.
- [2] R.L. Gordon, A.R. Masri, S.B. Pope and G.M. Goldin (2007a) "A Numerical Study of Auto-ignition in Turbulent Lifted Flames Issuing into a Vitiated Co-flow," *Combustion Theory and Modelling*, 11 (3), 351-376.
- [3] R.L. Gordon, A.R. Masri, S.B. Pope and G.M. Goldin (2007b) "Transport budgets in turbulent lifted flames of methane auto-igniting in a vitiated co-flow," *Combustion and Flame*, 151 (3), 495-511.
- [4] M.R.H. Sheikhi, P. Givi and S.B. Pope (2007) "Velocity-scalar filtered mass density function for large eddy simulation of turbulent reacting flows," *Physics of Fluids* 19 (9), 095106.
- [5] H. Wang and S.B. Pope (2008a) "Lagrangian investigation of local extinction, re-ignition and auto-ignition in turbulent flames," *Combustion Theory and Modelling*, *Combustion Theory and Modelling* 12(5), 857-882.
- [6] H. Wang and S.B. Pope (2008b) "Time averaging strategies in the finite-volume/particle algorithm for the joint PDF equation of turbulent reactive flows," *Combustion Theory and Modelling*, *Combustion Theory and Modelling* 12(3), 529-544.
- [7] L. Lu, S. R. Lantz, Z. Ren and S. B. Pope (2008) "Computationally efficient implementation of combustion chemistry in parallel PDF calculations," *Journal of Computational Physics*, (submitted).
- [8] P.P. Popov, R. McDermott and S.B. Pope (2008) "An accurate Time Advancement Algorithm for Particle Tracking," *Journal of Computational Physics*, Volume 227, Issue 20, pp. 8792-8806.
- [9] H. Wang, P. P. Popov, and S. B. Pope (2008) "Weak Second Order Splitting Schemes for Lagrangian Monte Carlo Particle Methods for the Composition PDF/FDF Transport Equations," *Journal of Computational Physics*, (submitted).

OTHER REFERENCES

- [1] R.S. Barlow and J.H. Frank (1998) "Effects of Turbulence on Species Mass Fractions in Methane/Air Jet Flames," *Proc. Combust. Inst.* 27, 1087-1095.
- [2] J. Xu, and S.B. Pope (2000) "PDF calculations of turbulent nonpremixed flames with local extinction," *Combust. Flame* 123, 281-307.
- [3] Q. Tang, J. Xu and S.B. Pope (2000) "PDF calculations of local extinction and NO production in piloted-jet turbulent methane/air flames," *Proceedings of the Combustion Institute*, 28, 133-139.

- [4] R.P. Lindstedt, S.A. Louloudi, and E.M. Vaos (2000) "Joint scalar probability density function modeling of pollutant formation in piloted turbulent jet diffusion flames with comprehensive chemistry," *Proc. Combust. Inst.* 28, 149-156.
- [5] R.S. Barlow, A.N. Karpetis, J.H. Frank, J.Y. Chen, (2001) "Scalar profiles and NO formation in laminar opposed-flow partially premixed methane/air flames," *Combust. Flame* 127, 2102-2118.
- [6] R. Cabra, T. Myhrvold, J.Y. Chen, R.W. Dibble, A.N. Karpetis, and R.S. Barlow (2002) "Simultaneous laser raman-rayleigh-lif measurements and numerical modeling results of a lifted turbulent H₂/N₂ jet flame in a vitiated coflow," *Proc. Combust. Inst.* 29, 1881-1888.
- [7] A.R. Masri, R. Cao, S.B. Pope and G.M. Goldin (2004) "PDF Calculations of Turbulent Lifted Flames of H₂/N₂ issuing into a vitiated co-flow," *Combust. Theory Modelling*, 8, 1-22.
- [8] R. Cabra, J.-Y. Chen, R.W. Dibble, A.N. Karpetis and R.S. Barlow (2005) "Lifted methane-air jet flames in a vitiated coflow," *Combustion and Flame*, 143, 491-506.
- [9] R. Cao and S.B. Pope (2005) "The influence of chemical mechanisms on PDF calculations of nonpremixed piloted jet flames," *Combustion and Flame*, 143, 450-470.
- [10] R. Cao, H. Wang and S.B. Pope (2005) "The effect of mixing models in PDF calculations of piloted jet flames," *Proc. Combust. Inst.*, 31, 1543-1550.
- [10] R. Cao, S.B. Pope and A.R. Masri (2005) "Turbulent lifted flames in a vitiated coflow investigated using joint PDF calculations," *Combustion and Flame*, 142, 549-568.
- [11] S.B. Pope (1997) "Computationally efficient implementation of combustion chemistry using in situ adaptive tabulation," *Combust. Theory Modelling* 1, 41-63.
- [11] L. Lu, Z. Ren, S.R. Lantz, V. Raman, S.B. Pope and H. Pitsch (2005) "Investigation of strategies for the parallel implementation of ISAT in LES/FDF/ISAT computations," 4th Joint Meeting of the U. S. Sections of the Combustion Institute, Philadelphia, PA.
- [12] Z. Ren, and S.B. Pope (2004) "An investigation of the performance of turbulent mixing models," *Combust. Flame* 136, 208-216.
- [13] H. Wang, S.B. Pope (2007) "Comparison of detailed reaction mechanism in non-premixed combustion," 5th Joint Meeting of the U. S. Sections of the Combustion Institute, UCSD, San Diego, March 26-28.
- [14] R. McDermott and S.B. Pope (2008), "The Parabolic Edge Reconstruction Method (PERM) for Lagrangian Particle Advection," *Journal of Computational Physics*, 227 (10), 5447-5491.
- [15] R. Cao and S.B. Pope (2003) "Numerical Integration of Stochastic Differential Equations: Weak Second-Order Mid-Point Scheme for Applications in the Composition PDF Method," *Journal of Computational Physics*, 185, 194-212.
- [16] A. Tocino and J. Vigo-Aguiar (2002) "Weak Second Order Conditions for Stochastic Runge-Kutta Methods," *SIAM Journal on Scientific Computing*, 24 (2), 507-523.
- [17] P.P. Popov and S.B. Pope (2008) "Stochastic Particle Advection in Hybrid Large Eddy Simulation/Filtered Density Function Methods," 61st Annual Meeting of the American Physical Society, Division of Fluid Dynamics, San Antonio, November 23-25, 2008.
- [18] S.B. Pope (1985) "PDF methods for turbulent reactive flows," *Progress in Energy and Combustion Science*, 11, 119-192.
- [19] P.E. Kloeden, E. Platen (1992) "Numerical Solution of Stochastic Differential Equations," Springer-Verlag, Berlin.
- [20] P.J. Roache (2002) "Code verification by the method of manufactured solutions," *J. Fluids Eng.* 124 (1), 4-10.
- [21] S. Subramaniam and S.B. Pope (1998) "A mixing model for turbulent reactive flows based on Euclidean minimum spanning trees," *Combustion and Flame*, 115, 487--514.

PERSONNEL SUPPORTED

Prof. Stephen B. Pope, PI
Liuyan Lu, Ph. D. student
Haifeng Wang, Ph.D. student
Pavel Popov, Ph.D. student

DEGREES GRANTED

Liuyan Lu, Ph.D., Mechanical Engineering, 2008.

MEETING PARTICIPATION

11th International Conference on Numerical Combustion, Granada, Spain, April 23-26, 2006.
Two contributed talks.

27th Annual Combustion Research Meeting, DOE/BES, Wintergreen, VA, May 30-June 2, 2006.

ARO/AFOSR Contractors' Meeting, in Chemical Propulsion, Arlington, VA, June 12-14, 2006.

7th World Congress on Computational Mechanics, Los Angeles, CA, July 16-22, 2006. Invited keynote lecture.

8th International Workshop on Measurement and Computation of Turbulent Nonpremixed Flames, Heidelberg, Germany, August 3-5, 2006.

31st International Symposium on Combustion, Heidelberg, Germany, August 6-11, two contributed papers.

59th Annual Meeting of the American Physical Society, Division of Fluid Dynamics, November 19-21, 2006, Tampa, FL. Five contributed talks.

Johns Hopkins University, April 13, 2007, Seminar.

NSF Panel, Washington, D.C., May 1, 2007.

28th Annual Combustion Research Meeting, DOE/BES, Airlie, VA, May 29-June 1, 2007.

ARO/AFOSR Contractors' Meeting in Chemical Propulsion, Boulder, CO, June 11-13, 2007.

Royal Society, New Fellows Seminar, London, July 11-12, 2007.

ECCOMAS Conference on Computational Combustion, Delft, Netherlands, July 18-20, 2007.
Invited talk.

Air Force Research Laboratories, Wright-Patterson Air Force Base, Dayton, OH, August 8, 2007. Seminar and visit.

Pennsylvania State University, Air Products Distinguished lecture, October 9, 2007.

APS/DFD Annual Meeting, Salt Lake City, November 18-20, 2007.

Delft University, Netherlands, The Burgers Lecture, January 10, 2008.

SIAM 12th International Conference on Numerical Combustion, Monterey, March 31-April 2, 2008.

DOE 29th Annual Combustion Research Conference, Airlie, May 27-30, 2008.

Symposium on Fluid Science and Turbulence, Johns Hopkins University, May 30-31, 2008.

AFOSR-ARO Contractors Meeting: Chemical Propulsion, Arlington, June 16-18, 2008.

TNF9: Ninth International Workshop on Measurement and Computation of Turbulent Nonpremixed Flames, Montreal, July 31-August 2, 2008.

32nd International Symposium on Combustion, Montreal, August 3-8, 2008.

DLES7: ERCOFTAC Workshop on Direct and Large-Eddy Simulation, Trieste, Italy, September 8-10, 2008.

DNS and LES of Reacting Flows, Maastricht, Netherlands, October 22-24, 2008.

61st Annual Meeting of the American Physical Society, Division of Fluid Dynamics, San Antonio, November 23-25, 2008.

INTERACTION WITH AFRL

At the ARO/AFOSR Contractors' Meeting (June 12-14, 2006) I discussed with Dr. J. T. Edwards the possible application to AFRL scramjet computations of chemistry dimension reduction techniques developed at Cornell. Following Dr. Edwards' suggestion, I then had an e-mail correspondence with Dr. Campbell Carter to provide further information on the technique, and to suggest how it might be applied. AFRL are currently considering the possibilities.

On August 8, 2007, the PI visited AFRL and presented a seminar on "Computational Modeling of Turbulence-Chemistry Interactions in Combustion." In addition to touring several of the facilities, he discussed ongoing research with Cam Carter, Mel Roquemore, Doug Davis, Susan Cox-Stouffer, among others. This included discussions on the modeling of turbulence-chemistry interactions in computations of scramjet engines. Since the AFOSR-ARO Contractors meeting in June 2008, the PI has contacted Drs. Campbell Carter, Bish Ganguly, Skip Williams and James Gord in order to continue the dialog on combustion modeling at AFRL.

On October 16, 2008, the PI hosted a visit to Cornell by Dr. Barry Kiel of AFRL. Dr. Kiel made a presentation on augmentor research, and had discussions with the PI and his research group on this topic. Subsequently, the PI provided Dr. Kiel with a written assessment of the role of LES/FDF methods in augmentor simulations.

TECHNOLOGY TRANSITIONS AND TRANSFERS

Over the years, the PI has successfully transferred several aspects of PDF methods and their numerical implementation to Fluent, Inc. As Fluent is the most widely used CDF code, this is an effective way to transition PDF capabilities to the aerospace (and other) industries. For example, the combustor design group at GE Aircraft Engines is using the PDF capability in Fluent. There is, however, no direct technology transfer to document this period.

HONORS AND AWARDS

Zeldovich Gold Medal, The Combustion Institute
Fellow of the Royal Society
Fellow of the American Academy of Arts and Sciences
Fellow of the American Physical Society
Fellow of the Institute of Physics
Associate Fellow of AIAA

INVENTIONS AND PATENTS

There were no inventions or patents during the reporting period.

Lagrangian investigation of local extinction, re-ignition and auto-ignition in turbulent flames

Haifeng Wang* and Stephen B. Pope

Sibley School of Mechanical and Aerospace Engineering, Cornell University, Ithaca, NY 14853, USA

(Received 15 April 2007)

Lagrangian PDF investigations are performed of the Sandia piloted flame E and the Cabra H_2/N_2 lifted flame to help develop a deeper understanding of local extinction, re-ignition and auto-ignition in these flames, and of the PDF models' abilities to represent these phenomena. Lagrangian particle time series are extracted from the PDF model calculations and are analyzed. In the analysis of the results for flame E, the particle trajectories are divided into two groups: continuous burning and local extinction. For each group, the trajectories are further sub-divided based on the particles' origin: the fuel stream, the oxidizer stream, the pilot stream, and the intermediate region. The PDF calculations are performed using each of three commonly used models of molecular mixing, namely the EMST, IEM and modified Curl mixing models. The calculations with different mixing models reproduce the local extinction and re-ignition processes observed in flame E reasonably well. The particle behavior produced by the IEM and modified Curl models is different from that produced by the EMST model, i.e., the temperature drops prior to (and sometimes during) re-ignition. Two different re-ignition mechanisms are identified for flame E: auto-ignition and mixing-reaction. In the Cabra H_2/N_2 lifted flame, the particle trajectories are divided into different categories based on the particles' origin: the fuel stream, the oxidizer stream, and the intermediate region. The calculations reproduce the whole auto-ignition process reasonably well for the Cabra flame. Four stages of combustion in the Cabra flame are identified in the calculations by the different mixing models, i.e., pure mixing, auto-ignition, mixing-ignition, and fully burnt, although the individual particle behavior by the IEM and modified Curl models is different from that by the EMST model. The relative importance of mixing and reaction during re-ignition and auto-ignition are quantified for the IEM model.

Keywords: PDF method, particle tracking, particle trajectories, mixing models, local extinction, re-ignition, auto-ignition

1. Introduction

Flame extinction and ignition are fundamental phenomena in combustion problems. The occurrence of extinction and ignition in turbulent reactive flows, due to intensive non-linear turbulence-chemistry interactions, is a challenge to modern turbulent combustion models. The probability density function (PDF) transport equation method [1–3] is increasingly found to be able to account accurately for the turbulence-chemistry interactions, e.g., local extinction and re-ignition [4, 5]. In engineering practice, the statistics of the turbulent velocity and composition fields are of primary concern in the context of Reynolds averaged Navier–Stokes (RANS) simulations. In PDF methods, the modeled PDF transport equation is usually solved numerically by a Lagrangian

*Corresponding author. Email: hw98@cornell.edu

particle method, and much more information can be extracted from the particle properties. Particle scatter plots (or joint PDFs) contain the most detailed information about the distribution of properties at a given position and time. All previous PDF calculations of turbulent flames have focused on Eulerian statistics and their comparison with experimental data, e.g., conditional or unconditional statistics of compositions, particle scatter plots and conditional PDFs of compositions. Scatter plots of particle properties are able to illustrate qualitatively different kinds of complicated turbulent combustion phenomena such as local extinction and re-ignition. To explore the PDF calculation results comprehensively, and to understand the turbulence-chemistry interactions more deeply, here we extract and analyze Lagrangian time series of particle properties from the PDF calculations. The particle trajectories are presented to illustrate the dynamic evolution of complicated turbulent combustion processes, i.e., local extinction and re-ignition in the turbulent non-premixed piloted jet flame, and auto-ignition in the turbulent lifted jet flame.

Lagrangian properties are important physical properties relevant not only to the PDF method, but also to real turbulence and combustion problems. Many Lagrangian investigations have been performed of turbulence using direct numerical simulations (DNS). Yeung [6, 7] studied the Lagrangian characteristics of turbulence and passive scalar transport in stationary isotropic turbulence with uniform mean scalar gradients. The Lagrangian properties of the scalars investigated are important to molecular mixing models. Mitarai *et al.* [8] performed DNS of an idealized non-premixed flame in decaying isotropic turbulence for conditions where flame extinction and re-ignition occur. In that work, the fluid particles are tracked to investigate flame extinction and re-ignition. Different categories of particles are identified, e.g., continuous burning and local extinction. Also investigated are Lagrangian properties of the conditional scalar diffusion, which appears as an unclosed term in the PDF transport equation. The same methodology is used to investigate the performance of flamelet models [9] and the performance of different mixing models [10]. Sripakagorn *et al.* [11] performed Lagrangian flame element tracking along the stoichiometric surface in decaying isotropic turbulence to investigate flame extinction and re-ignition. Three major scenarios of re-ignition in non-premixed combustion are identified, i.e., the independent flamelet scenario, re-ignition via edge flame propagation, and re-ignition through engulfment by hot neighbouring fluid. These Lagrangian investigations are helpful to provide insights into the dynamic evolution of turbulent combustion processes. Because of the formidable practical difficulties there are no experimental data on Lagrangian quantities in turbulent reactive flows. Experimental data are, however, becoming available on Lagrangian velocity and acceleration statistics in non-reactive flows [12–14].

The Lagrangian PDF method [2] represents the turbulent flow, transport and reaction processes via the time evolution of nominal Monte Carlo particles representing the joint PDF of velocity, turbulence frequency and compositions. Eulerian statistics obtained from PDF calculations have been explored extensively before, and are generally found to be in good agreement with the experimental data. It would be valuable to extract the Lagrangian time series which contains the whole history of the particle evolution in the multi-dimensional sample space. This work is dedicated, as a first effort, to explore the Lagrangian properties of the Monte Carlo particles in the PDF simulations of turbulent flames containing local extinction and re-ignition, and auto-ignition. The two flames studied are the Sandia non-premixed piloted jet flame E [15], and the lifted H_2/N_2 jet flame in a vitiated coflow [16], referred to as the Cabra flame.

In PDF methods, the closed form of the chemical reaction source term facilitates the exact treatment of detailed combustion chemistry. The modeling of the unclosed molecular mixing term in the PDF equation remains one of the major efforts of model development. Three mixing models are extensively used, i.e. the Euclidean minimum spanning tree (EMST) model [21], the interaction by exchange with the mean (IEM) model [18] (or the least-mean-square estimator

(LMSE) model [19]), and the modified Curl model [20, 22]. All the mixing models can represent local extinction and re-ignition to some extent [4, 5, 23], although the EMST model is usually thought to be superior in this respect. The simplicity of the IEM and modified Curl models makes them quite popular. In spite of the complexity of the EMST model, the public availability of a FORTRAN implementation [24] makes it easy to use. A desirable property of mixing models is "localness" [21]. All the models are local in physical space; only the EMST model is local in composition space; and none is local in velocity space. There is some recent progress in the development of more sophisticated mixing models, e.g., the multiple mapping conditioning (MMC) model [25], and the interaction by exchange with the conditional mean (IECM) mixing model [26–29], which is local in velocity space. The present work focuses on the three traditional mixing models (EMST, IEM and modified Curl) and evaluates their relative performance from the Lagrangian viewpoint.

The primary aim of PDF methods is to calculate accurately one-point, one-time Eulerian quantities. It is well understood [1] that this objective can be achieved using stochastic Lagrangian models, even if the multi-time properties of the models are not physically accurate. While the multi-time behavior of the stochastic models for position and velocity are physically realistic, those of the mixing models are not. For example Curl's model involves jumps in compositions; and (for the simplest homogeneous turbulence) the IEM model yields a deterministic relaxation to the mean, with no fluctuations along Lagrangian trajectories. Hence, while this study is valuable in shedding light on the models' behavior and performance, a close correspondence between the models' Lagrangian trajectories and those in the flame (could they be measured!) should not be expected.

The remaining sections of this paper are organized as follows. In Section 2, Eulerian scatter plots of particle properties are presented for the Sandia piloted flame E [15] and for the Cabra H_2/N_2 lifted jet flame [16]. The illustrations of local extinction and re-ignition, and of auto-ignition are reviewed by reference to the Eulerian particle data. The limitations of the Eulerian data are discussed. In Section 3, the particle tracking and particle sampling procedures are presented. In Sections 4 and 5 (for the Sandia flame E and the Cabra lifted flame, respectively), the Lagrangian time series obtained from the PDF calculation using the different mixing models are analyzed to study the models' representation of extinction, re-ignition and auto-ignition. The relative roles of mixing and reaction during re-ignition and auto-ignition are quantified for the IEM model in Section 6. Conclusions are drawn in the final section.

2. Particle calculations and Eulerian scatter plots

Comprehensive PDF model investigations of the Sandia piloted flames and the Cabra H_2/N_2 lifted jet flame have been described elsewhere [4, 5, 16, 23, 30–32]. In this section, PDF calculations of the Sandia flame E and the Cabra lifted jet flame are repeated to review the Eulerian particle scatter plots. As in [23, 30], a PDF code called HYB2D is used, in which a hybrid finite volume (FV)/particle algorithm is implemented for solving the joint PDF transport equation of the velocity, turbulence frequency and compositions [34]. The details of the simulations for the Sandia flame E and the Cabra lifted jet flame are identical to those in [35] and in [31], respectively, and are simply summarized in Table 1. (Quantities not listed in Table 1 can be found in [31] and [35].) Different values of the mixing model constant C_ϕ are specified for the different mixing models in the calculation of the Sandia flame E in order to achieve a stable burning flame with roughly the same amount of local extinction [23, 35] as observed experimentally. Similarly, different coflow temperatures are used in the calculation of the Cabra lifted flame with different mixing models in order to produce approximately the same flame lift-off height as observed experimentally [31].

Table 1. Details of the simulations for the Sandia flame E and the Cabra lifted H_2/N_2 jet flame.

Model parameters	Sandia flame E			Cabra lifted flame		
Turbulence frequency model constant [17], $C_{\omega 1}$	0.7			0.65		
Number of particles per cell, N_{pc}	100			100		
Chemistry	GRI-Mech 3.0 [37]			H_2 - O_2 mechanism [38]		
ISAT error tolerance [36], ϵ_{tol}	5.0×10^{-5}			6.25×10^{-6}		
Grid size	96×96			96×96		
	EMST	IEM	modified Curl	EMST	IEM	modified Curl
Mixing model constant, C_ϕ	1.5	2.7	3.3	1.5	1.5	1.5
Coflow temperature in Cabra lifted flame, T_c (K)	—	—	—	1033	1036	1036

Conventionally, the output from PDF calculations is Eulerian data for analysis at a fixed time (when the statistically stationary state has been reached) and at different locations. The conditional and unconditional statistics of the Eulerian data have been discussed extensively elsewhere [4, 5, 23, 30, 31] and will not be repeated here. In this section, we review the scatter plots of the particle temperature versus the mixture fraction in the Sandia flame E and the Cabra lifted flame. As previously discussed [4], it is difficult to make a rigorous quantitative comparison between scatter plots from experiment and model calculations, because of differences in the sampling and weighting of particles. Nevertheless, this comparison is useful in assessing, at least qualitatively, the ability of the models to represent the phenomena observed experimentally.

Figure 1 shows the scatter plots of the particle temperature against the mixture fraction at different axial locations in the Sandia flame E from measurements [15], and from the PDF simulations with different mixing models. The axial distance x is shown as x/D , where D is the diameter of the fuel jet. Two laminar flame temperature profiles (dashed lines in Figure 1) are also shown for reference. The laminar calculations are conducted by using OPPDIF [39] with two strain rates, $a = 10 \text{ s}^{-1}$ and 310 s^{-1} , and in the latter case, the temperature profile is shifted down by 300 K. Following [8], we use this shifted temperature profiles with $a = 310 \text{ s}^{-1}$ as a simple criterion to distinguish between burning particles (above the line) and extinguished particles (below the line). For simplicity, we call this line the “extinction line”, and the region above the “burning region”, and the region below the “extinction region”. There is of course an extinction limit of strain rate a_e ($a_e \approx 376 \text{ s}^{-1}$ for the current case) and its corresponding temperature profile in steady opposed laminar non-premixed jet flames, but we prefer not to use this extinction limit as our criterion. The extinction limit a_e applies only to steady laminar flames. In the unsteady case (e.g., laminar flames subject to the oscillation of strain rate), however, the instantaneous strain rate can exceed the extinction limit, without the flame being extinguished [40, 41]. Using the extinction limit of the steady laminar flame will somewhat over-estimate the amount of local extinction in this turbulent flame. Hence, as in [8], we use the shifted temperature profiles as a more conservative extinction limit. This criterion is somewhat arbitrary, but it is helpful for the qualitative analysis of the local extinction and re-ignition reported below.

From the experimental scatter plots in Figure 1, it may be seen that the number of the particles below the extinction lines decreases with increasing the axial distance from $x/D = 7.5$ to 45, indicating the evolution from local extinction to re-ignition. The PDF calculations with the three mixing models qualitatively reproduce this process to some extent. The scatter plots of the Eulerian particle data visually illustrate the level of local extinction at different locations. However, the Lagrangian evolution of the particle properties is not evident. Where do the locally

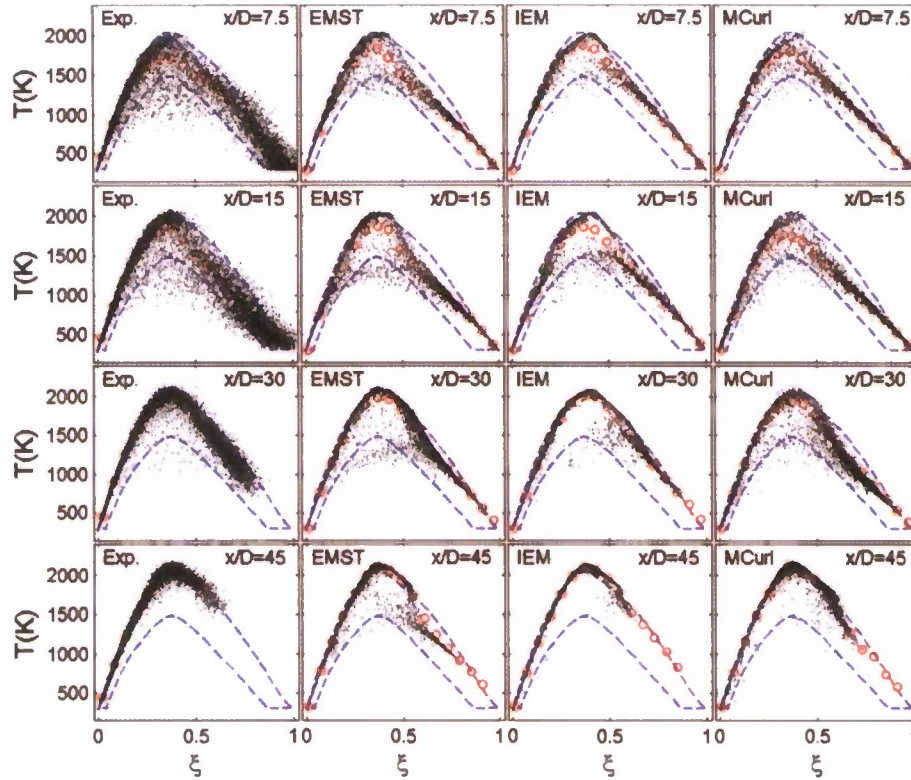


Figure 1. Scatter plots of temperature against the mixture fraction at the axial locations $x/D = 7.5, 15, 30$, and 45 in the Sandia piloted flame E from experimental data and from PDF calculations using three different mixing models (Open circles: conditional mean temperature; Dashed lines: temperature profiles in the opposed-jet laminar flame with strain rate $a = 10\text{s}^{-1}$ (upper lines); and with strain rate $a = 310\text{s}^{-1}$ (lower lines), shifted down by 300 K .)

extinguished particles come from? How do they return to the burning region (in composition space)? How do different mixing models cause the particles to move in the composition space? The current Eulerian data cannot answer these questions.

We now turn our attention to the Cabra H_2/N_2 lifted jet flame. Figure 2 shows the scatter plots of temperature versus mixture fraction at different axial locations in the flame. The equilibrium state calculated by using EQUIL [42] is also shown in the plots for reference. The initial enthalpy h and the species mass fractions \mathbf{Y} for the equilibrium calculation are taken to be linear in the mixture fraction ξ space, i.e.

$$h(\xi) = h_{\text{ox}} - (h_{\text{ox}} - h_{\text{fu}}) \cdot \xi \quad (1)$$

$$\mathbf{Y}(\xi) = \mathbf{Y}_{\text{ox}} - (\mathbf{Y}_{\text{ox}} - \mathbf{Y}_{\text{fu}}) \cdot \xi \quad (2)$$

where the subscript “fu” and “ox” denote the fuel stream and the oxidizer stream, respectively.

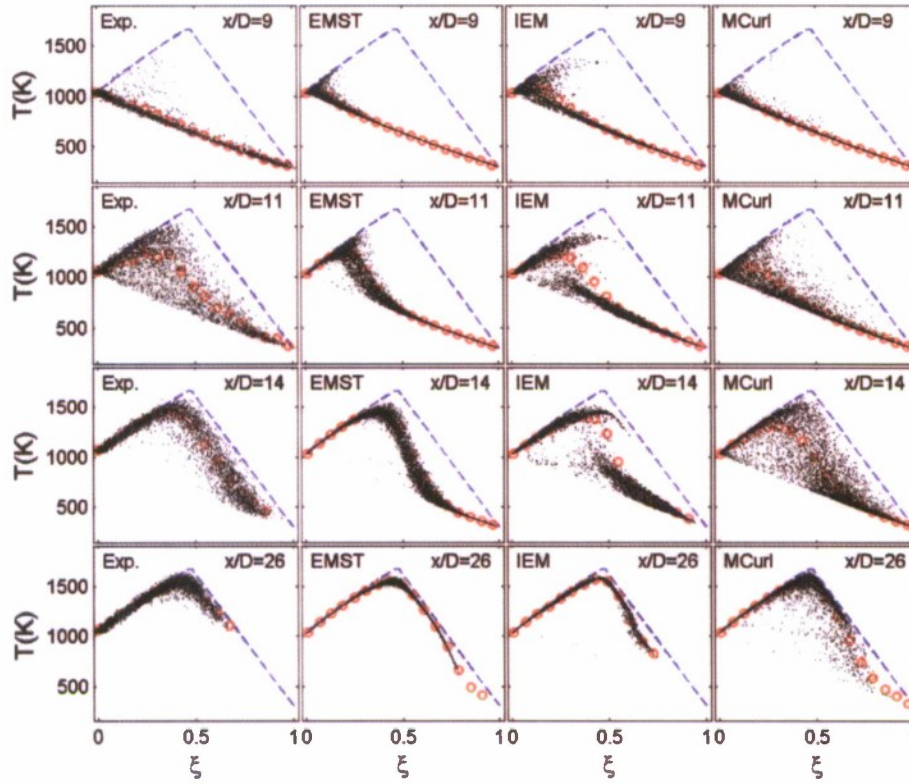


Figure 2. Scatter plots of particle temperature against mixture fraction at the axial locations $x/D = 9, 11, 14$, and 26 in the Cabra H_2/N_2 lifted flame from experimental data and from PDF calculations using three different mixing models (Open circles: conditional mean temperature; Dashed lines: equilibrium state.)

From the experimental data at $x/D = 9$ shown in Figure 2, it may be seen that the particles lie dominantly on the mixing line, with just a few rare particles with higher temperature. This combustion stage ($x/D \leq 9$) is called pure mixing. For $x/D \geq 11$, the particles leave the mixing line gradually, indicating an ignition process. By $x/D = 26$, almost all the particles have reached the fully burnt state, close to the equilibrium line. The PDF calculations using the three mixing models predict the mixing-ignition processes reasonably well. However, the scatter plots of temperature are different for the different mixing models. Similar questions arise, e.g., how do the different mixing models cause the particles to evolve through the mixing stage to the burning state? The Eulerian data cannot answer such questions.

3. Lagrangian particle tracking

The limitations of the Eulerian data from PDF calculations are evident. In this section, we discuss the extraction of Lagrangian time series from the PDF calculations, and these are analyzed for the Sandia flame E and the Cabra lifted flame in the following two sections.

In the Lagrangian PDF method [2], the modeled transport equation for the joint PDF of the velocity U , turbulence frequency ω , and the compositions ϕ is solved by a Monte Carlo particle method. A large number of Monte Carlo particles are released into the computational domain according to the Eulerian PDF initially. Each particle carries a full set of the fluid properties, i.e.,

U^* , ω^* , mass m^* , locations \mathbf{x}^* and ϕ^* etc. The evolution of the joint PDF is represented by the movement of the particles in the multi-dimensional space governed by the following stochastic differential equations [1–3]

$$dx_i^* = U_i^* dt, \quad (3)$$

$$dU_i^* = -\frac{1}{\langle \rho \rangle} \frac{\partial \langle p \rangle}{\partial x_i} dt - \left(\frac{1}{2} + \frac{3}{4} C_0 \right) \Omega (U_i^* - \tilde{U}_i) dt + (C_0 \tilde{k} \Omega)^{1/2} dW_i, \quad (4)$$

$$d\omega^* = -C_{\omega 3} \Omega (\omega^* - \tilde{\omega}) dt - S_{\omega} \Omega \omega^* dt + (2C_{\omega 3} C_{\omega 4} \tilde{\omega} \Omega \omega^*)^{1/2} dW, \quad (5)$$

$$\frac{d\phi_{\alpha}^*}{dt} = \mathcal{M}_{\alpha}(t) + S_{\alpha}(\phi^*(t)), \quad (6)$$

where ρ and p are the fluid density and pressure, respectively; “ $\langle \rangle$ ” denotes the conventional mean; “ $\tilde{}$ ” denotes the Favre mean; C_0 , $C_{\omega 3}$ and $C_{\omega 4}$ are model constants; \mathbf{W} is an isotropic vector-valued Wiener process; W is another independent Wiener process; \tilde{k} is the turbulent kinetic energy; S_{ω} and S_{α} are the source term for ω and the reaction source term for ϕ_{α} , respectively; $\mathcal{M}_{\alpha}(t)$ denotes the mixing model; Ω is the conditional mean turbulence frequency defined as

$$\Omega \equiv C_{\Omega} \frac{\langle \rho^* \omega^* | \omega^* \geq \tilde{\omega} \rangle}{\langle \rho \rangle}, \quad (7)$$

where the constant C_{Ω} is chosen so that Ω equals $\tilde{\omega}$ in a fully turbulent region [17].

The correspondence between the statistics of the Monte Carlo particles and those of the underlying turbulent reactive flow needs careful consideration [1, 3]. A primary aim of the modeling is for the one-point, one-time joint PDF of the particles to accurately represent the same joint PDF of the fluid in the reactive flow. On the other hand, two-point, one-time statistics are radically different: in the particle system the properties at two points are statistically independent (in the infinite particle limit), and indeed two particles may have the same location \mathbf{x}^* but completely different properties. Of particular relevance in the present study, is the question of correspondence of Lagrangian statistics. The Langevin equation model for velocity (Equation 4) has been constructed to be consistent with the Lagrangian velocity autocorrelation. However, the mixing models have been developed based solely on one-time Eulerian statistics, and the extent to which they represent Lagrangian statistics has not been evaluated even in simple non-reactive flows.

The solution procedure for the above equations is implemented in the code HYB2D which implements the consistent FV/particle algorithm [34]. The HYB2D code has been fully tested and validated in various papers, e.g. [23, 31, 34, 35]. This work slightly extends the HYB2D code to output the Lagrangian data.

A non-uniform mesh is used for both the FV solver and the particle tracking. The quantities at the mesh level are interpolated onto particles as needed. The statistics of particle properties on the mesh are formed from particles associated with the cell. The mixing between particles is performed within each grid cell.

The flames we are interested in are statistically stationary. The solution procedure implemented in HYB2D is a pseudo-time marching procedure. (A local time-stepping algorithm [43] is used for the marching procedure.) Starting from a “reasonable” initial condition, we march in time steps until a statistically stationary state is achieved. We continue the calculation for further time steps in order to output quantities of interest. At any time after the statistically stationary state

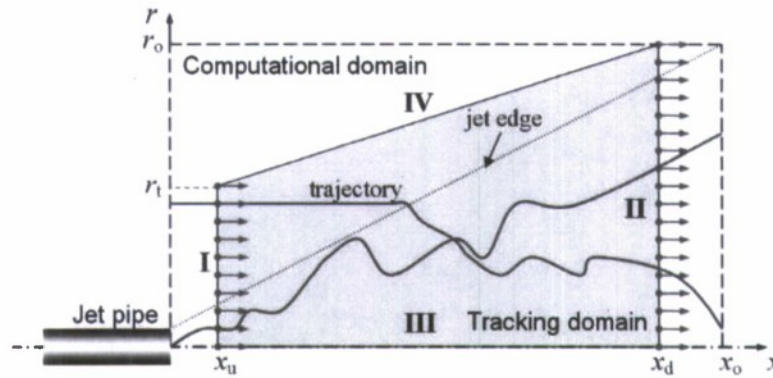


Figure 3. The computational domain and the tracking domain (consisting of four sides: I, II, III, and IV) for the jet flames.

is reached, the joint PDF is represented by a set of particles which (to some extent) model fluid particles.

Conventionally, in the PDF calculations only Eulerian data are output for postprocessing, i.e., the data at a particular time step after the statistically stationary state has been reached. Due to the Lagrangian nature of the numerical method, it is a simple matter to explore the Lagrangian data by simply exporting the particle data for many time steps after the stationary state has been reached, so that the Lagrangian particle trajectories can be formed.

Once the statistically stationary state is reached, we track a representative number N_t of particles through the active part of the flame defined as the tracking domain as shown in Figure 3. The geometry of the computational domain and the tracking domain, and the values of N_t are shown in Table 2 for the Sandia flame E and the Cabra lifted H_2/N_2 jet flame.

In the particle method, there is a particle cloning and clustering algorithm designed to maintain an approximately uniform number of particles per cell. This algorithm creates some complications for particle tracking. When a tracked particle is cloned, it splits into two or more (initially) identical particles of less weight. We arbitrarily select just one of the clones to continue the particle trajectory. When several light particles are clustered to form one heavier particle, the initial identities are lost. To prevent this problem, we suppress clustering of tracked particles (at a small cost in computational accuracy and efficiency).

Examination of the particle trajectories in physical space revealed some problems with the velocity-frequency model and its numerical implementation. These are discussed in the Appendix where a method of alleviating the problem is described.

Table 2. Geometry of the computational domain and the tracking domain, and the number of tracked particles N_t for the Sandia flame E and the Cabra lifted H_2/N_2 jet flame. See Figure 3 for definition of locations.

	x_u/D	x_d/D	x_o/D	r_t/D	r_o/D	N_t
Sandia flame E	3.0	45	80	10	20	2000
Cabra lifted flame	3.0	30	50	10	15	2000

4. Particle trajectories in Sandia flame E

PDF calculations of the Sandia flame E are performed by using the three mixing models, EMST, IEM and modified Curl. The Lagrangian tracking of particles is conducted to investigate the roles of reaction and mixing in the regions of local extinction and re-ignition. We focus on the particle behavior based on the evolution of the particle temperature in the mixture fraction space. As in the scatter plots of particles in Figures 1 and 2, and similar to the DNS analysis in [8], we divide the particle trajectories into two groups: continuous burning and local extinction. For continuous burning, the whole particle trajectory remains within the burning region (i.e., above the “extinction line”). For local extinction, some segment of the particle trajectory lies in the extinction region (below the “extinction line”). Physically, continuous burning corresponds to a stretched and distorted yet still continuous non-premixed laminar flame front, and the local extinction produces holes in the flame front [44, 45]. It should be appreciated, however, that in PDF methods there is no representation of the instantaneous flame structure. For ease of analysis, in each group, we further sub-divide the particles into different categories based upon their mixture fraction at the trajectory’s initial position x_u (see Figure 3 and Table 2 for details), i.e., fuel region ($\xi < 0.1$), oxidizer region ($\xi > 0.9$), pilot stream region ($0.22 < \xi < 0.55$), and the intermediate region (all other values of ξ).

In the flames considered here, the particle axial distance $x^*(t)$ is an increasing function of time t . To some extent, the axial distance can be viewed as a time-like variable since the particles do not flow backwards in the axial direction. Since we are more interested in local extinction and re-ignition at different axial locations, it is more revealing to explore the particle time series with respect to the axial distance x/D rather than with respect to time.

4.1. Trajectories of continuously burning particles

The trajectories of continuously burning particles from the fuel region in flame E are shown in Figures 4–6 for PDF calculations using the different mixing models. Only 25 particles randomly chosen from the tracking dataset are shown for each category. The circles in the plots show the current compositions of particles, and the lines connect their past compositions. For each figure of particle trajectories (such as Figures 4–6), the supplementary material includes a corresponding animation. These animations show the evolution with axial distance of all tracked particles’ compositions. In the temperature-mixture fraction 2-D plane in Figures 4–6, chemistry can only change the particle positions vertically due to element conservation during reaction (conservation of mixture fraction ξ), while mixing can move the particles both vertically and horizontally.

The general observations on the trajectories of the continuously burning particles calculated using the different mixing models are the following. First, the mixture fraction of particles can vary in the whole mixture fraction range, e.g., initially ξ^* is greater than 0.9 for all particles, while later ξ^* is less than 0.1 for some particles in Figures 4–6. As discussed before, this change is solely caused by mixing, indicating the important role of mixing in turbulent combustion. Second, different particles have completely different trajectories as expected in a turbulent flow. Third, at different stages of the particle evolution, the roles of reaction and mixing are different. In Figures 4–6, the particles from the fuel region tend to come close to the extinction line when first approaching the stoichiometric condition ($\xi = 0.351$). At around the stoichiometric condition in Figures 4–6, we can observe that some particles suddenly shoot upward (e.g., at $x/D=18$, some particle trajectories become nearly vertical). Apparently, in this stage, the reaction time scale is much less than the mixing time scale, and reaction becomes dominant. A quantitative presentation of the relative roles of mixing and reaction is discussed in Section 6.

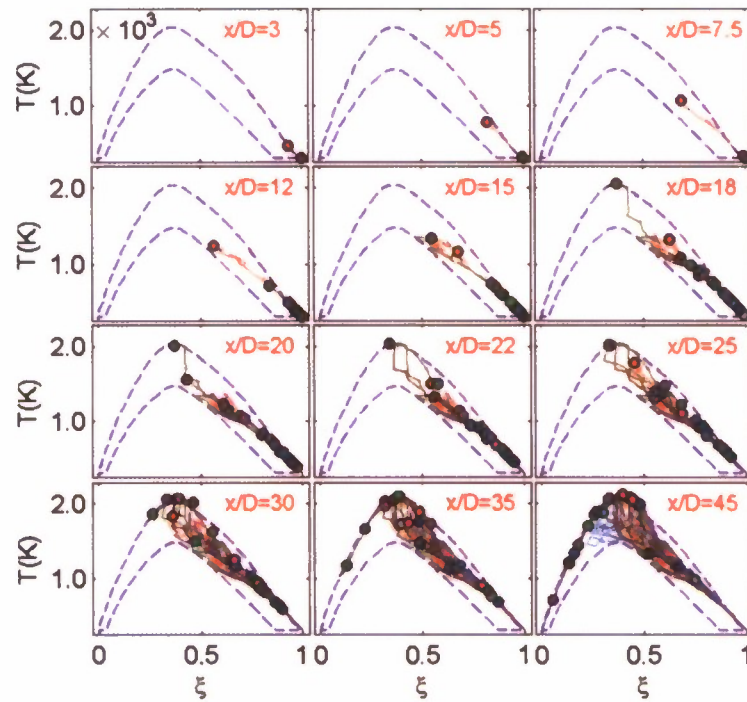


Figure 4. The continuous burning particle trajectories from the fuel region in flame E by the EMST model. (This [link](#) provides an animation of these particle trajectories.)

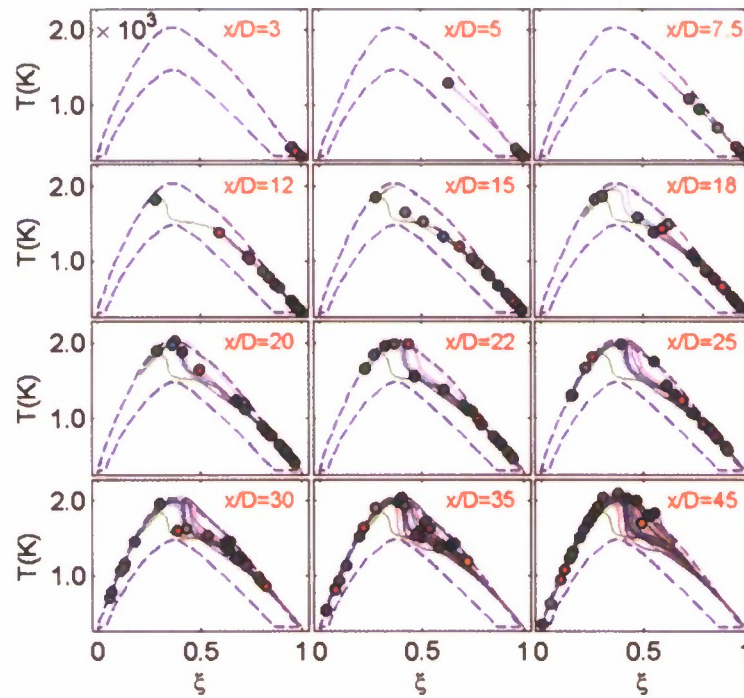


Figure 5. The continuous burning particle trajectories from the fuel region in flame E by the IEM model. (This [link](#) provides an animation of these particle trajectories.)

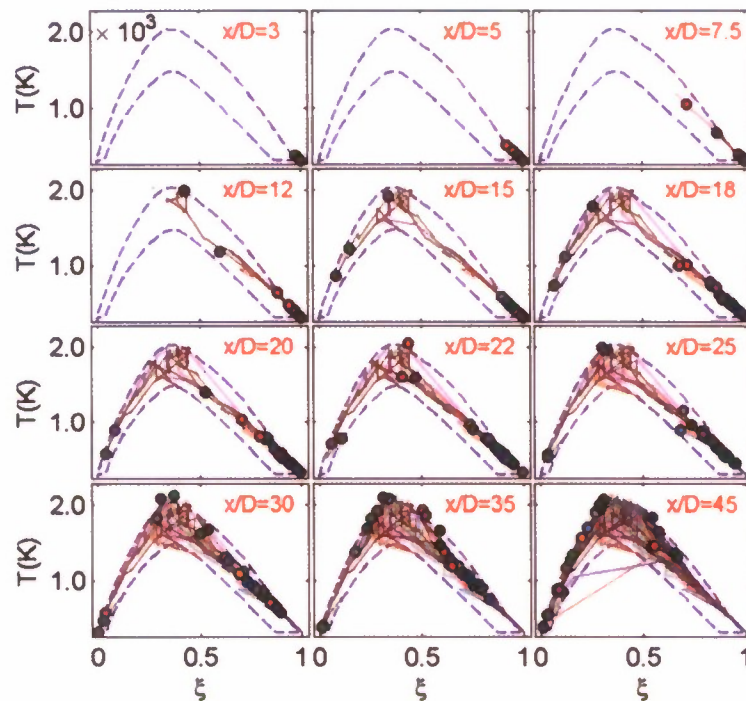


Figure 6. The continuous burning particle trajectories from the fuel region in flame E by the modified Curl model. (This [link](#) provides an animation of these particle trajectories.)

The particle behavior simulated by the different mixing models is qualitatively different. The particle trajectories produced by the EMST model are continuous but non-differentiable [21]. These trajectories are not smooth in Figure 4. The trajectories by the IEM model are continuous and differentiable, and the simulated trajectories are smooth and are clear in Figure 5. It is easy to follow each particle from the plot, making the observation and analysis much easier. The trajectories arising from the modified Curl model are discontinuous. The particles jump in composition space, possibly resulting in the direct mixing of a cold fuel particle and a cold oxidizer particle. This can be observed at $x/D = 45$ in Figure 6. Two particles with very lean and very rich mixtures are connected, indicating the jumping of the particle from the one side to the other side instantaneously. (For continuously burning particles, by definition, their compositions at no time lie in the extinction region, which means the straight lines across the extinction region at $x/D = 45$ in Figure 6 correspond to an instantaneous jump in particle composition.) This jump behavior by the modified Curl makes the particle trajectories difficult to follow.

Similar observations can be made from the trajectories of continuously burning particles from other categories (oxidizer region, pilot stream region and the intermediate region). Due to space limitations, these trajectories are not shown here.

4.2. Trajectories of locally extinguished particles

4.2.1. Particle trajectories from the EMST model

The locally extinguished particle trajectories originating from different regions in calculations using the EMST mixing model are shown in Figures 7–9.

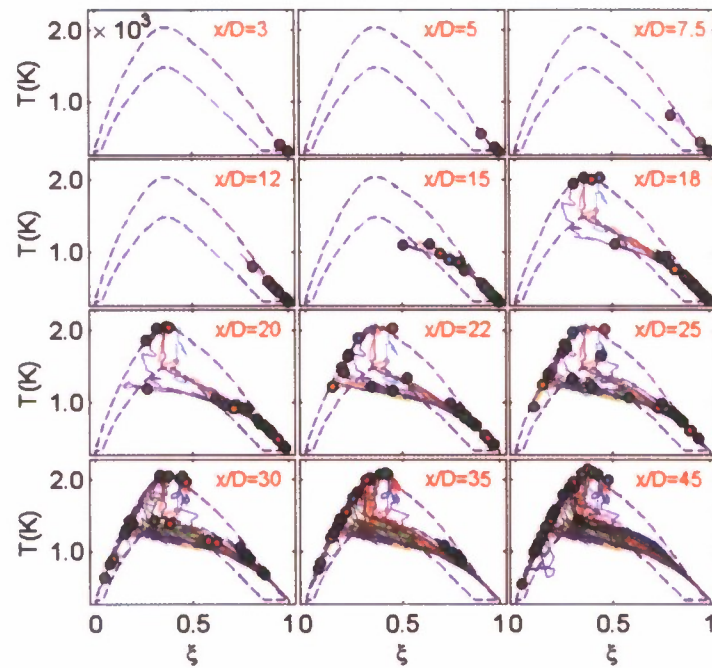


Figure 7. Trajectories of locally extinguished particles from the fuel region in flame E by the EMST model. (This [link](#) provides an animation of these particle trajectories.)

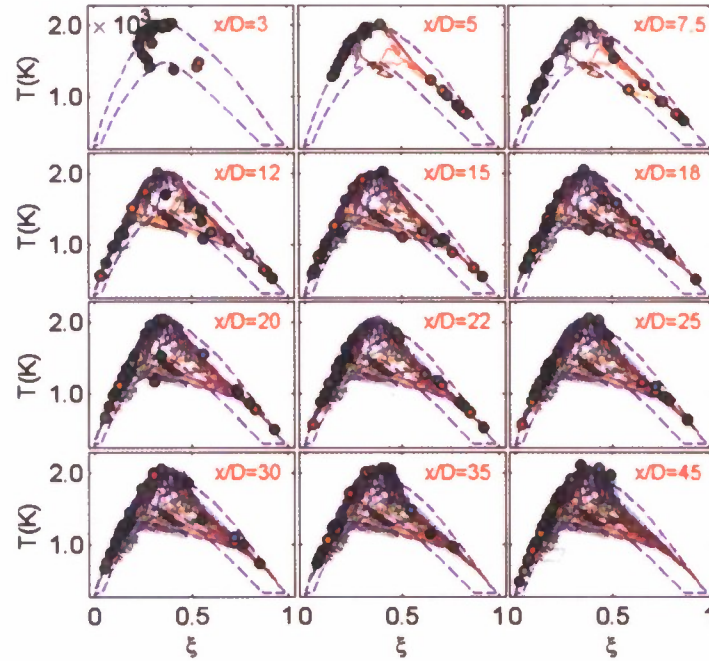


Figure 8. Trajectories of locally extinguished particles from the pilot stream region in flame E by the EMST model. (This [link](#) provides an animation of these particle trajectories.)

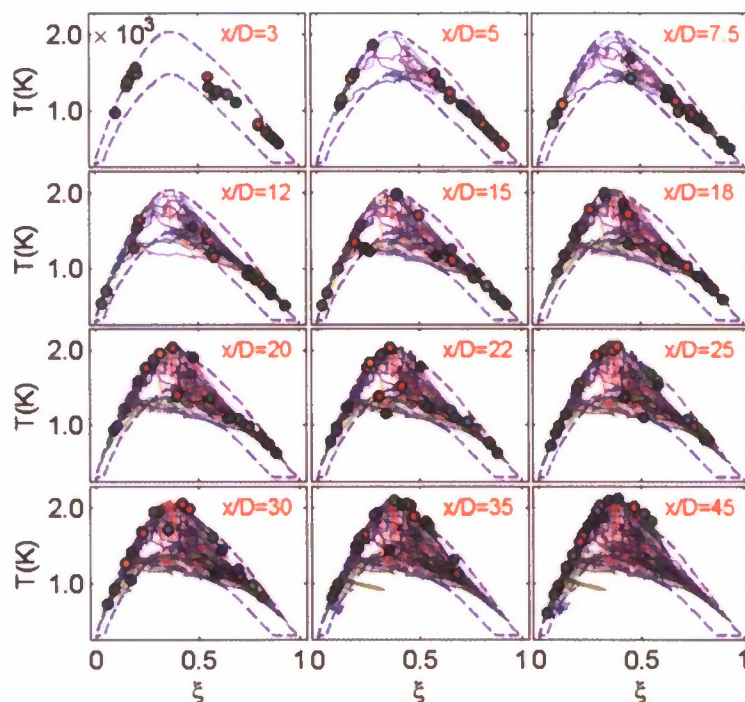


Figure 9. Trajectories of locally extinguished particles from the intermediate region in flame E by the EMST model. (This [link](#) provides an animation of these particle trajectories.)

Figure 7 shows the trajectories of particles initially from the fuel region. In the temperature-mixture fraction space, the mixture fraction of particles first decreases, and the particles come close to the extinction line. Around $\xi = 0.6$, the particles enter the extinction region, and become locally extinguished according to our criterion for extinction. The particle trajectories inside the extinction region become nearly horizontal (little temperature rise), implying that mixing is at least as rapid as reaction. The return of the particles to the burning region corresponds to re-ignition. From Figure 7, two different re-ignition processes can be observed. First, at around the stoichiometric condition, some trajectories of extinguished particles turn and move upward to return to the burning state, e.g., at $x/D = 18$ in Figure 7 we can observe four trajectories of extinguished particles moving dominantly upward to return to the burning state. During this re-ignition process, the mixture fraction of the particles changes slightly while the temperature rises by more than 600 K. Although re-ignition is the result of mixing and reaction, reaction seems dominant in this re-ignition process, which is similar to auto-ignition. The local extinction induced by the mixing causes the coexistence of fuel and oxidizer in the same particle, and the temperature of these particles is greater than 1000 K, e.g., one particle in the extinction region at $x/D = 15$ in Figure 7. Given appropriate conditions (e.g., induction period and a relatively long mixing time scale), the auto-ignition brings the particles back to the burning state. We refer to this re-ignition mechanism as an auto-ignition mechanism. Second, instead of auto-ignition, the other extinguished particles keep moving in the same direction (nearly horizontally to the left) and re-enter the burning state on the lean side of stoichiometric, e.g., from $x/D = 20$ to 45. During this process, mixing is at least as rapid as reaction. We call this mechanism the mixing-reaction mechanism. It is worth mentioning that the above two re-ignition mechanisms are identified in

the DNS study [11]. The particles from the oxidizer region (not shown) behave similarly to the particles from the fuel region. The two different re-ignition processes are also observed there.

Figure 8 shows the trajectories of the particles from the pilot stream region in flame E when using the EMST model. The pilot stream is used to stabilize the flame. From Figure 8, for this subset of particles (all of which enter the extinction region at some time), they dominantly enter the extinction region from the lean and rich sides, after there has been mixing essentially along the fully burnt line. Only one or two particles enter the extinction region from above around stoichiometric.

In Figure 9 are shown the trajectories of the particles from the intermediate region in flame E using the EMST model. Initially ($x/D \leq 7.5$) the particle composition changes due to mixing and reaction and remains, predominantly, in the burning region. The local extinction observable for $12 \leq x/D \leq 25$ occurs dominantly by mixing drawing rich and lean particles nearly horizontally into the extinction region.

In summary, the local extinction and re-ignition processes in the Sandia flame E are illustrated by tracking particles using the EMST model. Two different re-ignition mechanisms are observed in the flame by using the EMST model, i.e. auto-ignition and mixing-reaction. The investigation of the mixing models in conjunction with the large eddy simulations using the DNS data by Mitarai *et al.* [10] demonstrates the very good performance of the EMST mixing model in predicting the particle behavior in the regions of local extinction and re-ignition. The above observed particle behavior by the EMST is expected to represent the actual situation qualitatively.

4.2.2. Particle trajectories using the IEM and modified Curl models

The trajectories of the particles from the fuel region in flame E using the IEM model are shown in Figure 10. Following each particle trajectory, we can observe the similar local extinction and re-ignition processes as in the case of the EMST model (shown in Figure 7). The two re-ignition mechanisms can also be identified: auto-ignition and mixing-reaction. The re-ignition process for the IEM model, however, is somewhat different from that for the EMST model in Figure 7. In Figure 7, the re-igniting particles for the EMST model tend to move almost horizontally first with a slight temperature rise, and then either move upward due to the auto-ignition mechanism or keep moving horizontally due to the mixing-reaction mechanism without an obvious temperature drop before entering the burning region. In Figure 10, however, some of the re-igniting particles induced by the auto-ignition mechanism experience a temperature drop before ignition. Almost all the re-igniting particles induced by the mixing-reaction mechanism tend to decrease their temperature significantly before entering the burning region. For the IEM model at the early stages of re-ignition, this behavior is explained by the fact that the mean temperature (to which the particle temperature relaxes) is lower than that of the particles, which are about to re-ignite, since these are the hottest particles in the ensemble. To some extent this reflects the physics of the problem in that conduction cools fluid at a local temperature maximum. The trajectories of the particles from the other regions in flame E using the IEM model (not shown) show similar behavior to those from the fuel region in Figure 10.

Figure 11 shows the particle trajectories from the fuel region using the modified Curl model. The jumps in the particle properties make the understanding of particle behavior more difficult. The particle evolution is generally quite similar to the IEM model. Local extinction and re-ignition are predicted, and the two re-ignition mechanisms can be observed. However, similar to the IEM model, the re-igniting particles tend to have some temperature drop before or during the re-ignition, which is not observed in the EMST results. The trajectories of the particles from the other regions in flame E using the modified Curl model (not shown) show similar behavior to those from the fuel region in Figure 11.

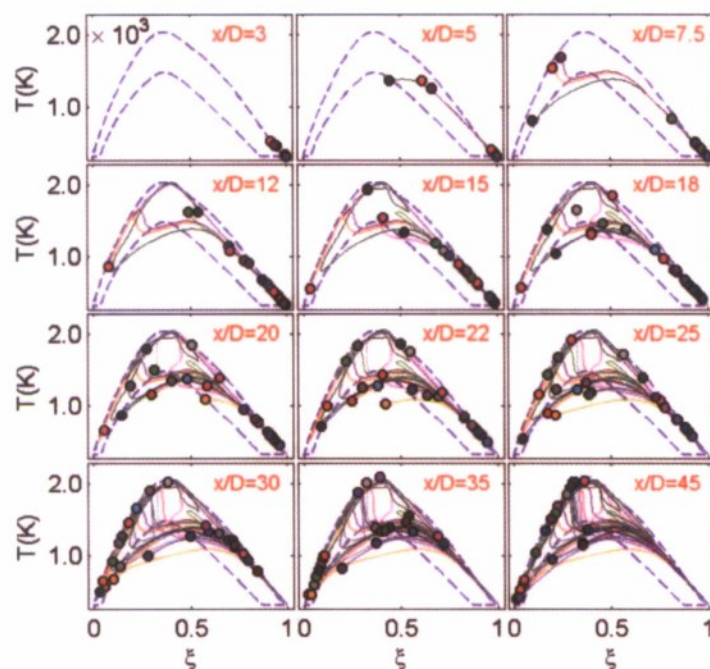


Figure 10. Trajectories of locally extinguished particles from the fuel region in flame E using the IEM model. (This [link](#) provides an animation of these particle trajectories.)

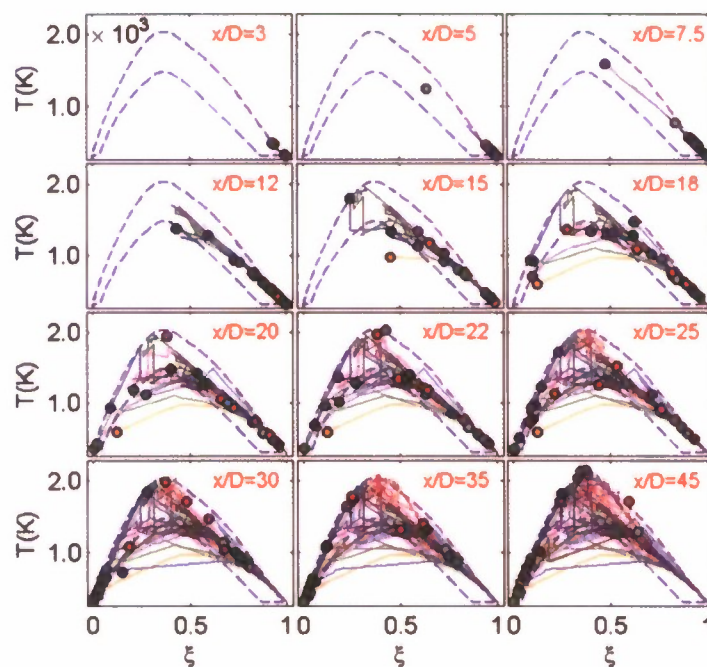


Figure 11. Trajectories of locally extinguished particles from the fuel region in flame E using the modified Curl model. (This [link](#) provides an animation of these particle trajectories.)

In this sub-section, the local extinction and re-ignition processes in the Sandia flame E are illustrated by tracking particles using the IEM and modified Curl models. The two re-ignition mechanisms (auto-ignition and mixing-reaction) identified by using the EMST model in Figure 7 are also observed here by using these two mixing models. However, the re-igniting particles by these two mixing models have somewhat different behavior from those by the EMST model, i.e., a temperature drop before or during the re-ignition. This difference in re-ignition by the different mixing models is not clear yet because there is no experimental data on Lagrangian trajectories in the flame. Nevertheless, the two identified re-ignition mechanisms and the different particle behavior during the re-ignition by the different mixing models cannot be observed with the Eulerian particle data, and the observations contribute to our understanding of the performance of the models.

5. Particle trajectories in Cabra H_2/N_2 lifted flame

Previous studies [31, 32] suggest that auto-ignition is a dominant mechanism in the stabilization of the Cabra H_2/N_2 lifted flame. In addition, both experimentally [33] and in modeling studies [31], it is found that the flames are extremely sensitive to the temperature of the vitiated coflow. To further understand and characterize these processes, we first perform auto-ignition tests in which the ignition delay time (IDT) is calculated as a function of mixture fraction and coflow temperature. The initial condition of the tests satisfies Equations (1)–(2). The fuel stream and the oxidizer stream in the tests are the same as those in the Cabra lifted flame. The coflow (oxidizer) temperature varies from $T_c = 1022$ K to 1080 K. Figure 12 shows the IDTs of the mixture for different coflow temperatures. The IDT is defined here as the time when the mixture temperature reaches the mid-point between the initial temperature and the equilibrium temperature. The strong sensitivity of the IDTs to the coflow temperature is evident from the plot, which is consistent with the findings in [31]. The shortest IDTs occur at the very fuel-lean region, around $\xi = 0.04$. The stoichiometric condition is $\xi = 0.47$ in the flame. The IDTs varies by three orders of magnitude over the range of mixture fraction shown.

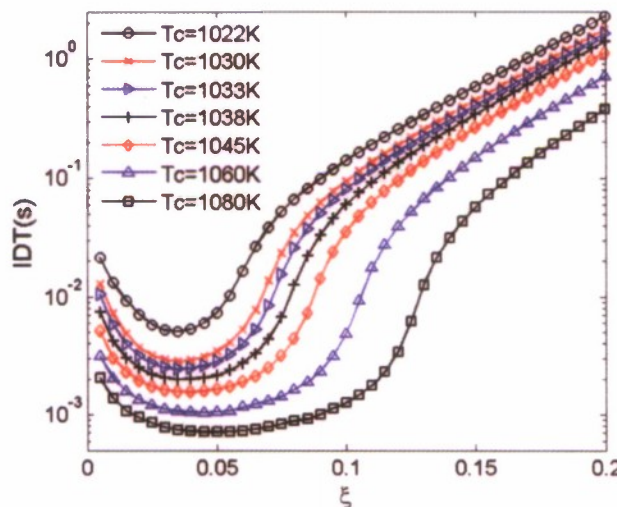


Figure 12. The ignition delay time (IDT) of $H_2/N_2/O_2$ mixture for different coflow temperature T_c .

The PDF calculations of the Cabra H_2/N_2 lifted flame are performed by using the three mixing models, EMST, IEM and modified Curl. The Lagrangian tracking of particles is conducted to investigate the roles of reaction and mixing in the flame. The tracking details are shown in Table 2. As in the analysis of flame E in Section 4, we focus on the particle behavior based on the evolution of the particle temperature in mixture fraction space. The particle trajectories are divided into different categories based upon their mixture fraction at the trajectory initial position x_u , i.e., fuel region ($\xi < 0.1$), oxidizer region ($\xi > 0.9$), and the intermediate region between the fuel and the oxidizer region. For each category, 100 particles randomly chosen from the tracking dataset are shown in the following figures, whereas all tracked particles are shown in the corresponding animations in the supplementary material.

Figure 13 shows the trajectories of the particles from the fuel region in the Cabra lifted flame using the EMST model. Initially, ($x/D \leq 9$) the particles move in the plane exclusively by mixing. A particle trajectory due to pure mixing is a nearly straight line between the cold fuel temperature and the hot coflow temperature. Pure mixing yields a partially premixed mixture of fuel and oxidizer at different mixture fractions. At about $x/D = 10$, some particles near the oxidizer side start to ignite first due to their short IDTs as shown in Figure 12. The ignition mechanism of the first few particles is expected to be auto-ignition, similar to the auto-ignition of the homogeneous mixture in Figure 12.

After the rapid auto-ignition of the first few particles, these relatively hot burnt particles at $x/D > 11$ in Figure 13 mix with adjacent particles in composition space, thus raising their temperature (and radical concentration) and hence promoting their auto-ignition. Therefore the ignition progressively moves to richer mixtures. This burning process is not exclusively the auto-ignition of the particles. Both reaction and mixing play important roles. A plausible physical picture of the processes involved in the Cabra flame is that some regions under the fuel-lean condition ignite first after the induction period given an appropriate mixing condition. These ignition spots are distributed in the physical space separately. After the high temperature ignition spots are formed, they propagate toward each other and merge into a connected premixed flame front. This picture is supported by the DNS study of the auto-ignition of mixing layers between cold fuel and hot oxidizer in an isotropic and homogeneous turbulence flow [46]. The evolution of the particles using EMST in Figure 13 is consistent with this picture, even though the spatial structure of the instantaneous flame is not explicitly represented. We simply name this ignition process as mixing-ignition. By $x/D = 30$ in Figure 13, all the particles shown reach the full burnt state close to the equilibrium line. From the particle trajectories in the Cabra lifted jet flame using the EMST model, we can observe the whole mixing-reaction process. Four stages of combustion can be identified, i.e. pure mixing, auto-ignition, mixing-ignition, and fully burnt. Apparently, this combustion detail cannot be observed from the Eulerian data like the scatter plot in Figure 2. The particles from the other regions in the Cabra lifted flame by using EMST model (not shown) show the similar ignition dynamics.

In Figure 14 are shown the trajectories of the particles from the fuel region in the Cabra lifted flame using the IEM model. Pure mixing occurs for $x/D < 10$. At the locations between $x/D = 10$ and 11, a few particles near the oxidizer side (brought there by mixing) start to auto-ignite. After the auto-ignition of the first few particles, the temperature of other particles in the rich region is raised through their mixing with the elevated mean, and the ignition of these particles is promoted. Mixing and reaction play important roles in this ignition process. As in the EMST model, this ignition process can be named as mixing-ignition. The particle behavior in this ignition process for the IEM model is slightly different from that for the EMST model in Figure 13. The EMST model is local in composition space. Hence the burnt particles at given ξ^* mix with particles around the same value of ξ^* . While in the IEM model all particles mix towards the mean. In spite of the different particle behavior, four stages of combustion can be identified

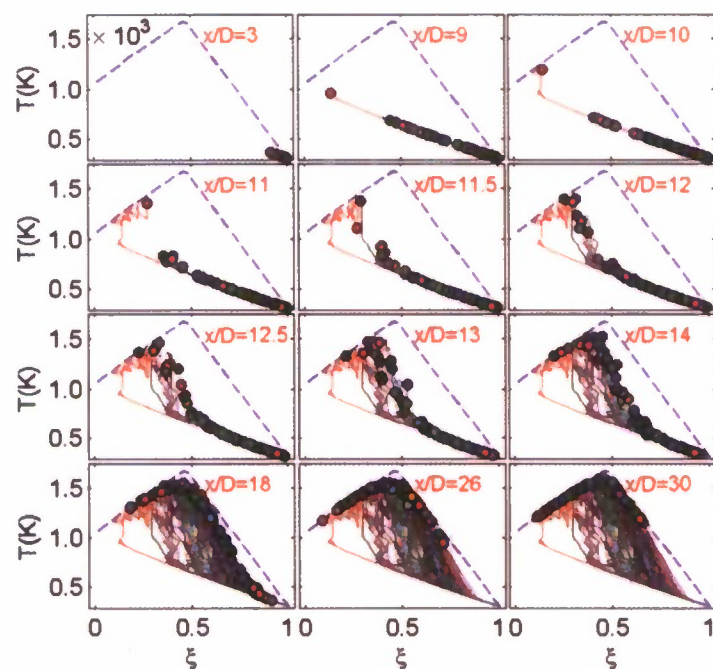


Figure 13. Particle trajectories from the fuel region in the Cabra lifted flame using the EMST model. (This [link] provides an animation of these particle trajectories.)

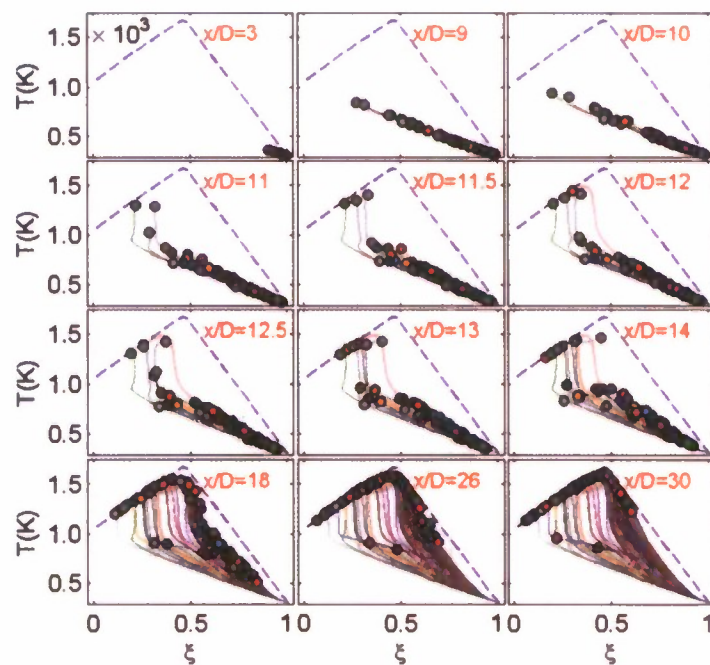


Figure 14. Particle trajectories from the fuel region in the Cabra lifted flame using the IEM model. (This [link] provides an animation of these particle trajectories.)

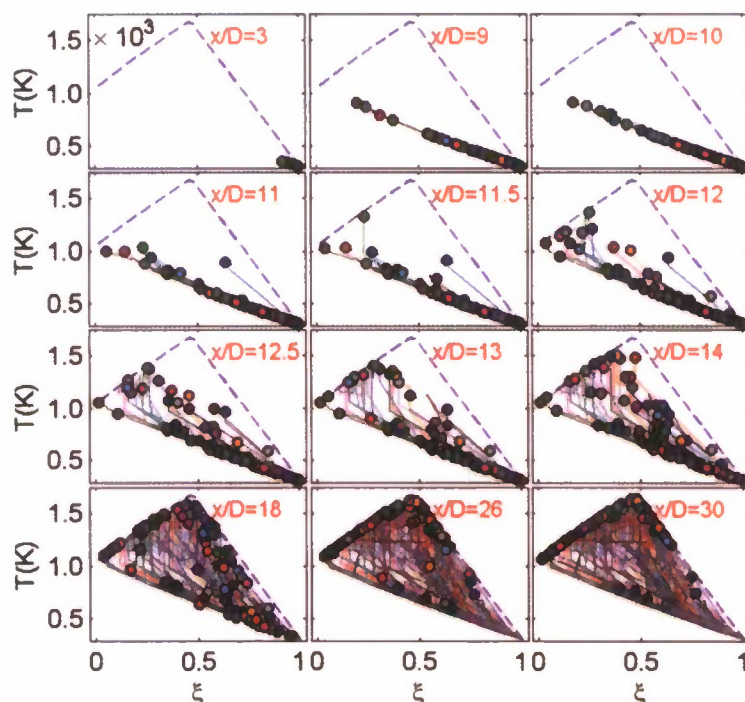


Figure 15. The particle trajectories from the fuel region in the Cabra lifted flame by the modified Curl model. (This [link](#) provides an animation of these particle trajectories.)

for the IEM as those in the EMST model. The trajectories of the particles from the other regions (not shown) show similar particle behavior for IEM model as in Figure 14.

In Figure 15 are shown the particle trajectories from the fuel region in the Cabra lifted flame using the modified Curl model. The modified Curl model can reproduce the same four combustion stages in the flame identified by the previous two mixing models. As in the IEM model, the particle behavior in the mixing-ignition stage by the modified Curl model is also different from that by the EMST model due to the non-localness of the model in the composition space. The particle trajectories from the other regions in the Cabra lifted flame using the modified Curl model (not shown) show the same behavior.

In this section, the particle trajectories using the different mixing models are investigated in the Cabra H_2/N_2 lifted flame. The particle behavior by the IEM and modified Curl models is different from that by the EMST model, because of the non-localness of the IEM and modified Curl models compared to the localness property of the EMST model. In spite of the different individual particle behavior, the overall combustion processes revealed by the different mixing models are similar, and four stages of combustion in the flame can be identified, i.e. pure mixing, auto-ignition, mixing-ignition, and fully burnt. In some sense, this finding is consistent with the DNS study of an auto-ignition problem in homogeneous isotropic turbulence [46], even though the particles do not provide a direct representation of spatial structure. This contributes to our understanding of the model performance in the turbulent lifted jet flames.

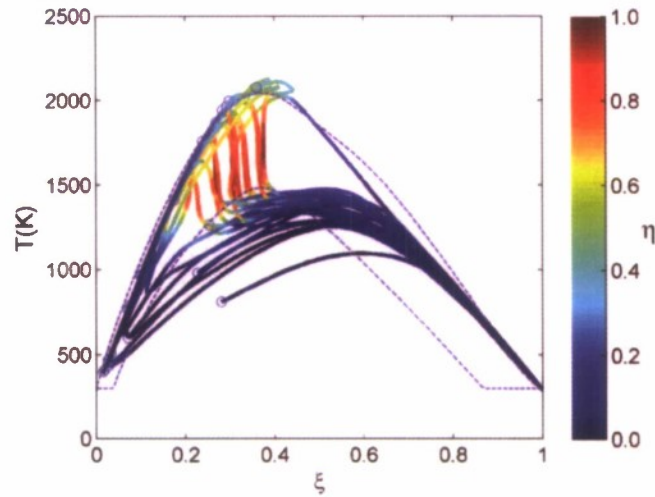


Figure 16. Trajectories (up to $x/D = 45$) color-coded by parameter η (Equation 10) of locally extinguished particles from the fuel region in flame E using the IEM model.

6. Roles of mixing and reaction during re-ignition and auto-ignition

In the previous sections, the roles of mixing and reaction during the particle evolution are discussed qualitatively. The relative importance of mixing and reaction for each particle as it evolves can be quantified by examining the mixing rate given by the mixing models relative to the reaction rate. For this purpose we define the mixing rate $\dot{\mathcal{M}}$ and reaction rate \dot{S} for each particle as,

$$\dot{\mathcal{M}} = \sqrt{\left(\frac{d\xi}{dt}\right)^2 + \left(\frac{1}{T_{ref}} \frac{dT}{dt}\right)^2} \bigg|_{\text{mix}}, \quad (8)$$

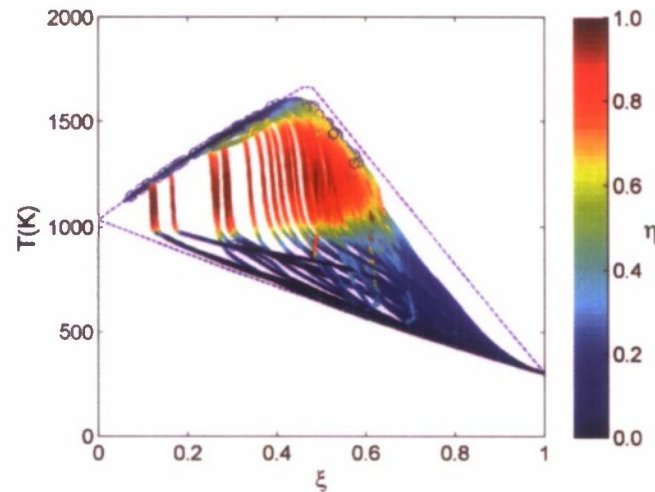


Figure 17. Particle trajectories (up to $x/D = 30$) color-coded by parameter η (Equation 10) from the fuel region in the Cabra lifted flame using the IEM model

and

$$\dot{S} = \left| \frac{1}{T_{ref}} \frac{dT}{dt} \right|_{\text{react}}, \quad (9)$$

where $T_{ref} = 2000$ K, and in Equations (8) and (9) the rates of change pertain solely to the effects of mixing and reaction, respectively. (In the computations, these quantities are readily evaluated based on the particle properties before and after the mixing and reaction fractional steps.)

The relative importance of mixing and reaction can be quantified by the parameter

$$\eta = \frac{S}{S + \mathcal{M}}, \quad (10)$$

which varies between zero (corresponding to no reaction) and one (corresponding to no mixing).

We focus our investigation on the IEM mixing model. For the modified Curl model, the composition changes discontinuously, and so $d\xi/dt|_{\text{mix}}$ is not well defined. For the EMST mixing model, $d\xi/dt|_{\text{mix}}$ exhibits large fluctuations of small time scale which obscure the picture.

Figure 16 shows, for flame E, trajectories color-coded by the parameter η of locally extinguished particles initially from the fuel region. From the figure, we can clearly see the relative importance of mixing and reaction during re-ignition. For the particles re-igniting due to auto-ignition mechanism, the reaction is dominant ($\eta \approx 1.0$) when the particles shoot upward at around stoichiometric condition. For those particles which re-ignite due to mixing-reaction, either both mixing and reaction are important (e.g., $\eta \approx 0.3$ for one particle entering the burning region at about $T = 1100$ K), or mixing is dominant due to the low temperature.

In Figure 17, the particle trajectories originating from fuel stream in the Cabra flame are shown. In the current simulation of the Cabra flame, the initial ignition process occurs when particles leave the pure mixing line between cold fuel and hot coflow. From the figure, it may be seen that the particle starting to ignite at fuel-lean side leave the pure mixing line dominantly by reaction, corresponding to the auto-ignition identified before. The particles leaving the pure mixing line on the fuel-rich side experience two stages: a mixing-dominant stage to raise the particle temperature to about 1000 K, and reaction-dominant stage to raise the particle temperature close to the equilibrium. Both mixing and reaction are important for the ignition of these particles, and they correspond to the previously identified mixing-ignition process. The particle trajectories along with the rates of mixing and reaction provide insights on the roles of mixing and reaction during re-ignition and auto-ignition.

7. Conclusion

Lagrangian PDF investigations of the Sandia piloted flame E and the Cabra H_2/N_2 lifted flame are performed to help obtain a deeper understanding of the modeling of local extinction, re-ignition and auto-ignition in these flames. Eulerian scatter plots (shown in Figures 1–2) of the two flames from the PDF calculations are reviewed to show the limitations of one-time statistics. A Lagrangian particle tracking procedure is implemented in the code HYB2D. Lagrangian particle data are extracted from the PDF calculations after the statistically stationary state is reached, in order to explore the PDF result more comprehensively.

Lagrangian particle tracking in the PDF calculations of Sandia flame E is performed for the different mixing models, EMST, IEM and modified Curl. The particle trajectories are divided into two groups, continuous burning and local extinction. For each group, the trajectories are further sub-divided into different categories based on the original particle locations: the fuel steam, the

oxidizer stream, the pilot stream, and the intermediate region. The particle trajectories given by the different mixing models are different, i.e., continuous but non-differentiable by EMST, continuous and differentiable by IEM, and discontinuous by modified Curl. All three mixing models reproduce the local extinction and re-ignition processes reasonably. Two different re-ignition mechanisms are identified, the auto-ignition mechanism and the mixing-reaction mechanism.

Homogeneous auto-ignition tests for the same condition as in the Cabra H_2/N_2 lifted flame are conducted. The lowest ignition delay time (IDT) occurs at a very fuel-lean condition for a range of coflow (oxidizer) temperatures. The strong sensitivity of the IDTs to the coflow temperature is observed, which is also reported in previous PDF calculations of the Cabra lifted flame [31].

Lagrangian particle tracking in the PDF calculations of the Cabra H_2/N_2 lifted is also performed for the different mixing models. The particle trajectories are divided into different categories based on the original particle locations: the fuel stream, the oxidizer stream, and the intermediate region. The models reproduce the whole auto-ignition process reasonably. Four stages of combustion in the Cabra flame are identified in the calculations, i.e., pure mixing, auto-ignition, mixing-ignition, and fully burnt.

The roles of mixing and reaction during re-ignition and auto-ignition are investigated by using IEM. The relative importance of mixing and reaction is quantified for particles during re-ignition and auto-ignition.

Acknowledgements

This work is supported by the Air Force Office of Scientific Research, Grant FA9550-06-1-0048 and by Department of Energy, Grant DE-FG02-90ER. Various suggestions from David A. Caughey, Zhuyin Ren and Steven R. Lantz are appreciated. This research was conducted using the resources of the Cornell Theory Center, which receives funding from Cornell University, New York State, federal agencies, foundations, and corporate partners.

References

- [1] Pope, S.B., 1985, PDF methods for turbulent reactive flows. *Progress in Energy and Combustion Science*, **11**, 119–192.
- [2] Pope, S.B., 1994, Stochastic Lagrangian models for turbulence. *Annual Reviews of Fluid Mechanics*, **26**, 23–63.
- [3] Pope, S.B., 2000, *Turbulent Flows* (Cambridge University Press, Cambridge, UK).
- [4] Xu, J., Pope, S.B., 2000, PDF calculations of turbulent nonpremixed flames with local extinction. *Combustion and Flame*, **123**, 281–307.
- [5] Lindstedt, R.P., Louloudi, S.A., Vaos, E.M., 2000, Joint scalar probability density function modeling of pollutant formation in piloted turbulent jet diffusion flames with comprehensive chemistry. *Proceedings of the Combustion Institute*, **28**, 149–156.
- [6] Yeung, P.K., 2001, Lagrangian characteristics of turbulence and scalar transport in direct numerical simulations. *Journal of Fluid Mechanics*, **427**, 241–274.
- [7] Yeung, P.K., 2002, Lagrangian investigations of turbulence. *Annual Reviews of Fluid Mechanics*, **34**, 115–142.
- [8] Mitarai, S., Riley, J.J., Kosaly, G., 2003, A Lagrangian study of scalar diffusion in isotropic turbulence with chemical reaction. *Physics of Fluids*, **15**, 3856–3866.
- [9] Mitarai, S., Kosaly, G., Riley, J.J., 2004, A new Lagrangian flamelet model for local flame extinction and reignition. *Combustion and Flame*, **137**, 306–319.
- [10] Mitarai, S., Riley, J.J., Kosaly, G., 2005, Testing of mixing models for Monte Carlo probability density function simulations. *Physics of Fluids*, **17**, 047101.
- [11] Sripakagorn, P., Mitarai, S., Kosaly, G., Pitsch, H., 2004, Extinction and reignition in a diffusion flame: a direct numerical simulation study. *Journal of Fluid Mechanics*, **518**, 231–259.

- [12] Voth, G.A., Satyanarayan, K., Bodenschatz, E., 1998, Lagrangian acceleration measurements at large Reynolds numbers. *Physics of Fluids*, **10**, 2268–2280.
- [13] La Porta, A., Voth, G.A., Crawford, A.M., Alexander, J., Bodenschatz, E., 2001, Fluid particle accelerations in fully developed turbulence. *Nature*, **409**, 1017–1019.
- [14] Mordant, N., Leveque, E., Pinton, J.-F., 2004, Experimental and numerical study of the Lagrangian dynamics of high Reynolds turbulence. *New Journal of Physics*, **6**, 116–159.
- [15] Barlow, R.S., Frank, J.H., 1998, Effects of turbulence on species mass fractions in methane-air jet flames. *Proceedings of the Combustion Institute*, **27**, 1087–1095.
- [16] Cabra, R., Myhrvold, T., Chen, J.-Y., Dibble, R.W., Karpetis, A.N., Barlow, R.W., 2002, Simultaneous laser Raman-Rayleigh-Lif measurements and numerical modeling results of a lifted turbulent H₂/N₂ jet flame in a vitiated coflow. *Proceedings of the Combustion Institute*, **29**, 1881–1888.
- [17] Van Slooten, P.R., Jayesh, Pope, S.B., 1998, Advances in PDF modeling for inhomogeneous turbulent flows. *Physics of Fluids*, **10**, 246–265.
- [18] Villermaux, J., Devillon, J.C., 1972, Représentation de la coalescence et de la redispersion des domaines de ségrégation dans un fluide per modèle d'interaction phénoménologique. In: *Proceedings of the Second International Symposia on Chemical Reaction Engineering*, Elsevier, New York.
- [19] Dopazo, C., O'Brien, E.E., 1974, An approach to the autoignition of a turbulent mixture. *Acta Astronautica*, **1**, 1239–1266.
- [20] Janicka, J., Kolbe, W., Kollmann, W., 1979, Closure of the transport-equation for the probability density function of turbulent scalar fields. *Journal of Non-Equilibrium Thermodynamics*, **4**, 47–66.
- [21] Subramaniam, S., Pope, S.B., 1998, A mixing model for turbulent reactive flows based on Euclidean minimum spanning trees. *Combustion and Flame*, **115**, 487–514.
- [22] Nooren, P.A., Wouters, H.A., Peeters, T.W.J., Roekaerts, D., Maas, U., Schmidt, D., 1997, Monte Carlo PDF modelling of a turbulent natural-gas diffusion flame. *Combustion Theory and Modelling*, **1**, 79–96.
- [23] Cao, R.R., Wang, H., Pope, S.B., 2007, The effect of mixing models in PDF calculations of piloted jet flames. *Proceedings of the Combustion Institute*, **31**, 1543–1550.
- [24] Ren, Z., Subramaniam, S., Pope, S.B., 2004, Implementation of the EMST mixing model, <http://eccentric.mae.cornell.edu/~tcg/emst>.
- [25] Klimenko, A.Y., Pope, S.B., 2003, A model for turbulent reactive flows based on multiple mapping conditioning. *Physics of Fluids*, **15**, 1907–1925.
- [26] Pope, S.B., 1994, On the relationship between stochastic Lagrangian models of turbulence and second-moment closures. *Physics of Fluids*, **6**, 973–985.
- [27] Fox, R.O., 1996, On velocity conditioned scalar mixing in homogeneous turbulence. *Physics of Fluids*, **8**, 2678–2691.
- [28] Pope, S.B., 1998, The vanishing effect of molecular diffusivity on turbulent dispersion: implications for turbulent mixing and the scalar flux. *Journal of Fluid Mechanics*, **359**, 299–312.
- [29] Sawford, B.L., 2004, Micro-Mixing Modelling of Scalar Fluctuations for Plumes in Homogeneous Turbulence. *Flow, Turbulence and Combustion*, **72**, 133–160.
- [30] Cao, R.R., Pope, S.B., 2005, The influence of chemical mechanisms on PDF calculations of non-premixed piloted jet flames. *Combustion and Flame*, **143**, 450–470.
- [31] Cao, R.R., Pope, S.B., Masri, A.R., 2005, Turbulent lifted flames in a vitiated coflow investigated using joint PDF calculations. *Combustion and Flame*, **142**, 438–453.
- [32] Masri, A.R., Cao, R., Pope, S.B., Goldin, G.M., 2004, PDF Calculations of Turbulent Lifted Flames of H₂/N₂ issuing into a vitiated co-flow. *Combustion Theory and Modelling*, **8**, 1–22.
- [33] Wu, Z., Starnner, S.H., Bilger, R.W., 2005, Lift-off heights of turbulent H₂/N₂ jet flames in a vitiated co-flow. in: D.R. Honnery (Ed.), *Proceedings of the 2003 Australian Symposium on Combustion and the Eighth Australian Flame Days*, The Combustion Institute.
- [34] Muradoglu, M., Pope, S.B., Caughey, D.A., 2001, The hybrid method for the PDF equations of turbulent reactive flows: consistency conditions and correction algorithms. *Journal of Computational Physics*, **172**, 841–878.
- [35] Wang, H., Pope, S.B., 2008, Time averaging strategies in the finite-volume/particle hybrid algorithm for the joint PDF equation of turbulent reactive flows. *Combustion Theory and Modelling* (DOI: 10.1080/13647830701847875).
- [36] Pope, S.B., 1997, Computationally efficient implementation of combustion chemistry using in situ adaptive tabulation. *Combustion Theory and Modelling*, **1**, 41–63.

- [37] Smith, G.P., Golden, D.M., Frenklach, M., Moriarty, N.W., Eiteneer, B., Goldenberg, M., Bowman, C.T., Hanson, R.K., Song, S., Gardiner Jr., W.C., Lissianski, V.V., Qin, Z., http://www.me.berkeley.edu/gri_mech/.
- [38] Li, J., Zhao, Z., Kazakov, A., Dryer, F.L., 2003, An updated comprehensive kinetic model for H_2 combustion. in: *Fall Technical Meeting of the Eastern States Section of the Combustion Institute*, Penn. State University, University Park, PA.
- [39] Lutz, A.E., Kee, R.J., Grcar, J.F., Rupley, F.M., 1997, OPPDIF: A Fortran Program for Computing Opposed-flow Diffusion Flames, Report No. SAND96-8243, Sandia National Laboratories.
- [40] Sung, C.J., Law, C.K., 2000, Structural sensitivity, response, and extinction of diffusion and premixed flames in oscillating counterflow. *Combustion and Flame*, **123**, 375–388.
- [41] Egolfopoulos, F.N., 2000, Structure and extinction of unsteady, counterflowing, strained, non-premixed flames. *International Journal of Energy Research*, **24**, 989–1010.
- [42] Lutz, A.E., Rupley, F.M., Kee, R.J., 1996, EQUIL: A CHEMKIN Implementation of STANJAN, for Computing Chemical Equilibria, Report No. SAND96-xxxx, Sandia National Laboratories.
- [43] Muradoglu, M., Pope, S.B., 2002, Local time-stepping algorithm for solving the probability density function turbulence model equations. *AIAA Journal*, **40**, 1755–1763.
- [44] Pantano, C., 2004, Direct simulation of non-premixed flame extinction in a methane-air jet with reduced chemistry. *Journal of Fluid Mechanics*, **514**, 231–270.
- [45] Hult, J., Meier, U., Meier, W., Harvey, A., Kaminski, C.F., 2005, Experimental analysis of local flame extinction in a turbulent jet diffusion flame by high repetition 2-D laser techniques and multi-scalar measurements. *Proceedings of the Combustion Institute*, **30**, 701–709.
- [46] Mastorakos, E., Baritaud, T.A., Poinot, T.J., 1997, Numerical simulations of autoignition in turbulent mixing flows. *Combustion and Flame*, **109**, 198–223.

Appendix: Particle trajectories in physical space

Figure 18 shows the particle trajectories in physical space for the Cabra H_2/N_2 lifted flame and for the Sandia flame E, from calculations using the EMST mixing model. The top border of the plot is the free-stream boundary. When the particles from the turbulent jet approach the non-turbulent free stream, their velocity should relax rapidly towards the free stream velocity. However, from Figure 18, it may be seen that some particles shoot into the free stream with little or no relaxation of velocity, and are then reflected off the free-stream boundary (according to

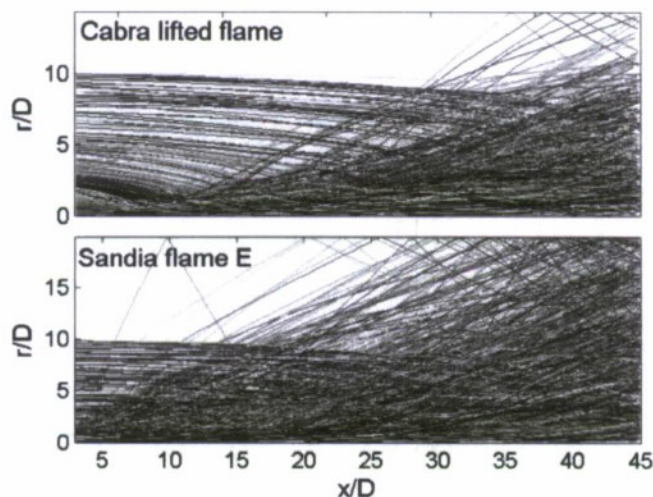


Figure 18. Particle trajectories in physical space for the Cabra H_2/N_2 lifted jet flame and for the Sandia flame E from the original turbulence frequency model.

the specified boundary condition). This non-physical behavior of the particles is not expected to occur when the conditional mean frequency Ω (Equation (7)) is used to define the time-scale in the stochastic turbulence frequency model (Equation (5)) [17]. The turbulence frequency in the turbulent region is much greater than that in the non-turbulent free stream. Ideally, if one turbulent fluid particle \mathcal{P} dives into one mesh cell \mathcal{C} in the laminar free stream environment, the turbulence frequency of particle \mathcal{P} will be the only frequency used to determine $\Omega (= C_\Omega \cdot \omega_{\mathcal{P}}^*)$, where $\omega_{\mathcal{P}}^*$ is the turbulence frequency of particle \mathcal{P} in cell \mathcal{C} according to Equation (7). From the Langevin model Equation (4), the velocity of particle \mathcal{P} will decay rapidly at rate Ω toward the free stream velocity. However, under certain circumstances, the particle \mathcal{P} is not the only particle chosen to determine the conditional mean frequency Ω . In the current situation (of a cylindrical coordinate system), the initial mass of a particle is linearly proportional to the particle's radial location. Compared to the particle mass in the free stream, the mass of the particle \mathcal{P} originating closer to the axis is much less. In this case, the mass-weighted mean frequency $\tilde{\omega}$ in cell \mathcal{C} is close to the mean frequency in the free stream. On the other hand, numerically the turbulence frequency for the particles in the free stream is not exactly the same, i.e., there are small fluctuations in particle turbulence frequency in the free stream. These fluctuations are caused by the Wiener process in Equation (5) and by the disturbance caused by the turbulent fluid particle \mathcal{P} . Assume that the maximum of the turbulence frequency in cell \mathcal{C} is ω_{m2}^* when particle \mathcal{P} is excluded. It may happen that ω_{m2}^* is greater than $\tilde{\omega}$, so that the possibly massive particle with frequency ω_{m2}^* is included in the calculation of Ω . Therefore the value of Ω is much less than the desired value $C_\Omega \cdot \omega_{\mathcal{P}}^*$. In another words, the value of Ω is greatly under-estimated, and so is the decaying rate of the velocity of the particle \mathcal{P} .

In spite of the non-physical behavior of the particles described above, it should be appreciated that this behavior occurs with low probability (less than 1% of the number of tracked particles in the Cabra lifted flame, and about 5% in the Sandia flame E). They do not influence the statistics significantly. Since the particle behavior is relatively more important in this work, we try to eliminate or reduce the non-physical behavior in the following *ad hoc* way. In the above discussed case, the particle \mathcal{P} should be chosen as the only particle to determine Ω , in spite of the small fluctuations of the turbulence frequency in the free stream. If we can identify this

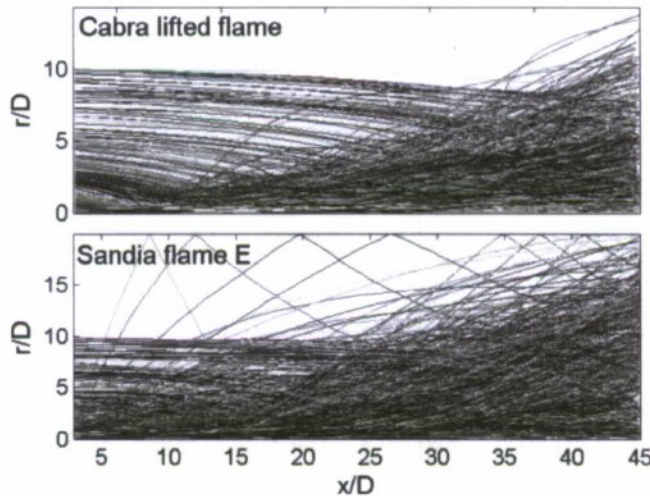


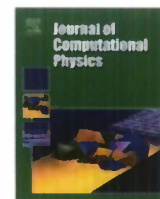
Figure 19. Particle trajectories in the physical space for the Cabra H_2/N_2 lifted jet flame and for the Sandia flame E with an *ad hoc* revision to the turbulence frequency model.

particular case, we can avoid this problem by calculating Ω using particle \mathcal{P} only. We use the following criteria to identify the case. If in one grid cell, the maximum turbulence frequency $\omega_{\mathcal{P}}^*$ of a particle \mathcal{P} is much greater than the Favre mean frequency $\tilde{\omega}$ ($\omega_{\mathcal{P}}^* > c_1 \cdot \tilde{\omega}$), and also much greater than the frequency of all other particles in the cell ($\omega_{\mathcal{P}}^* > c_2 \cdot \omega_{m2}^*$), and the mass of the particle $m_{\mathcal{P}}^*$ is much less than the average mass of the particles $\langle m \rangle$ ($m_{\mathcal{P}}^* < c_3 \cdot \langle m \rangle$), we then use particle \mathcal{P} exclusively to determine Ω . The constants are chosen as $c_1 = 15$, $c_2 = 8$, and $c_3 = 0.2$. The particle trajectories in physical space obtained with this special treatment of the frequency model are shown in Figure 19. The non-physical particles disappear in the Cabra lifted flame, and the number of the non-physical particles is significantly reduced in Sandia flame E. The special treatment improves the practical performance of the turbulence frequency model to some extent. The remaining non-physical particles in the Sandia flame E shown in Figure 19 are due to the limitation of the criteria. Using a different specification of c_1 , c_2 , and c_3 , we can eliminate the non-physical particles completely, but it also then affects the turbulence region. In this work, we use this *ad hoc* revision to reduce the number of non-physical particles. Those particles not caught by the criteria are removed from the particle subset in the discussion. This *ad hoc* revision to the frequency model does not change the statistics of the velocity and composition fields. We appreciate that the criteria does not guarantee the convergence of the method when the number of particles tends to infinity.



Contents lists available at ScienceDirect

Journal of Computational Physics

journal homepage: www.elsevier.com/locate/jcp

An accurate time advancement algorithm for particle tracking

Pavel P. Popov^{a,*}, Randall McDermott^b, Stephen B. Pope^a

^a Sibley School of Mechanical and Aerospace Engineering, Cornell University, 245 Upson Hall, Ithaca, NY 14853, USA

^b Building and Fire Research Laboratory, National Institute of Standards and Technology, Gaithersburg, MD 20899-8663, USA

ARTICLE INFO

Article history:

Received 25 January 2008

Received in revised form 12 June 2008

Accepted 19 June 2008

Available online 28 June 2008

Keywords:

Particle tracking

Time advancement

Turbulent reactive flow

Large eddy simulation

Particle method

Filtered density function

Second-order Runge–Kutta

ABSTRACT

We describe a particle position time advancement algorithm that is designed for use with several subgrid velocity reconstruction schemes used in LES/FDF methods, and potentially in other applications. These reconstruction schemes yield a subgrid velocity field with desirable divergence properties, but also with discontinuities across cell faces. Therefore, a conventional time advancement algorithm, such as second-order Runge–Kutta (RK2), does not perform as well as it does with a smooth velocity field. The algorithm that we describe, called Multi-Step RK2 (MRK2), builds upon RK2 by breaking up the time step into two or more substeps whenever a particle crosses one or more velocity discontinuities. When used in conjunction with the parabolic edge reconstruction method, MRK2 performs considerably better than RK2: both the final position of an advected particle, and the final area of a 2D infinitesimal area element are second-order accurate in time (as opposed to first-order accurate for RK2). Furthermore, MRK2 has the theoretical advantage that it better preserves the continuity of the mapping between initial and final particle positions.

© 2008 Elsevier Inc. All rights reserved.

1. Introduction

In this paper, we consider some aspects of particle tracking in hybrid finite-volume/particle PDF methods for turbulent reactive flows. In these methods, and potentially in other CFD applications, we have a large number of particles (on the order of 10^7) whose positions are initially random and evolve by the ODE:

$$\frac{d\mathbf{X}^*}{dt} = \mathbf{U}^* = \mathbf{U}(\mathbf{X}^*(t), t), \quad (1)$$

where $\mathbf{X}^*(t)$ is a particle's position as a function in time, and $\mathbf{U}(\mathbf{X}^*(t), t)$ is the velocity experienced by the particle. Usually, this velocity consists of a deterministic component and a random term which is part of the turbulence model [5]: in the present paper, we consider the deterministic part only. In general, velocity information is available at discrete locations on a finite-volume (FV) grid, and therefore a particle tracking algorithm consists of two parts: a velocity interpolation scheme which interpolates the FV velocity onto the particle locations, and a time advancement scheme which updates the particle locations, using the interpolated velocity.

In recent research on FV/particle PDF methods for reacting flows, accurate particle tracking has been recognized as an important condition for maintaining numerical consistency between the finite-volume and the particle aspects of the solution. Muradoglu et al. [2] define mean particle mass density, $q(\mathbf{x}, t)$, as the expectation of the total mass of particles in an infinitesimal region, normalized by that region's volume:

$$q \equiv \langle m^* \delta(\mathbf{X}^* - \mathbf{x}) \rangle \quad (2)$$

* Corresponding author.

E-mail address: ppp7@cornell.edu (P.P. Popov).

(where m^* denotes a particle's mass), and have shown that an important consistency condition is that the mean particle mass density should remain equal to the FV mean density:

$$q = \langle \rho \rangle, \quad (3)$$

provided that the initial conditions are consistent, $q(\mathbf{x}, 0) = \langle \rho(\mathbf{x}, 0) \rangle$. The meaning of Eq. (3) is that the expected mass of all particles inside a certain region S must be equal to the expected mass of fluid in S as given by the FV density field. In the incompressible case, for example, this means that if particles are initially uniformly distributed in the computational domain, then they should remain so for all time.

In order to satisfy the above consistency condition, Muradoglu et al. [2] employ a position-correction algorithm which introduces a small displacement in the particle positions after each time step, in order to enforce Eq. (3). A similar position-correction algorithm has been employed by Zhang and Haworth [4].

In a different approach, Jenny et al. [3] note that if particles move with a velocity:

$$\mathbf{U}^* = \tilde{\mathbf{U}} + \mathbf{u}^*, \quad (4)$$

where $\tilde{\mathbf{U}}$ is a deterministic component interpolated from the FV velocity, and \mathbf{u}^* is a random component with zero mean, then the following equation holds:

$$\left(\frac{\partial}{\partial t} + \tilde{\mathbf{U}} \cdot \nabla \right) \ln q = -\nabla \cdot \tilde{\mathbf{U}}, \quad (5)$$

which has the same form as the mean continuity equation:

$$\left(\frac{\partial}{\partial t} + \tilde{\mathbf{U}} \cdot \nabla \right) \ln \langle \rho \rangle = -\nabla \cdot \tilde{\mathbf{U}}, \quad (6)$$

where $\tilde{\mathbf{U}}$ is the mean velocity. Therefore, if Eq. (3) is satisfied at $t = 0$, it will also be satisfied implicitly at future time, provided that the velocity interpolation scheme yields accurate values for the reconstructed velocity and its divergence, and provided that an accurate time advancement scheme is used. Addressing the velocity interpolation issue, Jenny et al. [3] introduce a 2D velocity interpolation scheme with desirable divergence properties. McDermott and Pope [1] improve upon this scheme, and extend it to 3D, calling the new scheme the parabolic edge reconstruction method (PERM). It has been shown [1] that PERM performs better than standard multilinear interpolation in satisfying the above-mentioned consistency condition in the particle tracking limit (i.e., when there are no velocity fluctuations).

In the present work, we make a further improvement in particle tracking by using a time-stepping algorithm which has been specifically designed for use in conjunction with PERM. The new algorithm, called Multi-Step Runge–Kutta 2 (MRK2) is quite similar to the standard second-order Runge–Kutta (RK2), but it provides a more accurate treatment of particles which cross a velocity discontinuity. Although MRK2 is motivated by the PERM reconstruction, it can also be used as an alternative to RK2 in all applications in which particles need to be advected through a velocity field with discontinuities at known locations.

To illustrate the benefits of PERM and MRK2, Fig. 1 shows final particle distributions for a simple 2D incompressible test flow with a uniform initial particle distribution. In this case, the final particle distribution should be uniform as well. It can be seen in Fig. 1 that, when RK2 is used as the time advancement scheme, the PERM velocity interpolation yields a more uniform final particle distribution than standard bilinear interpolation. We can also see that the final particle distribution becomes even more uniform when the new time-stepping scheme, MRK2, is used in conjunction with the PERM velocity interpolation.

1.1. Properties of the PERM velocity reconstruction

The reader is referred to [1] for a thorough description of PERM and its properties – here we focus only on its aspects which are relevant to the MRK2 time-stepping scheme.

The PERM velocity reconstruction scheme uses discretized velocity information in the form of face-average velocity components in the direction normal to a given grid cell face (we shall refer to this as the 'FV velocity', for the sake of brevity). The PERM reconstructed velocity within a given grid cell depends only on the FV velocity on the faces of that cell and its nearest neighboring cells. Its functional form, in two dimensions (the extension to 3D is rather intuitive) is

$$\begin{aligned} u(q, r) &= (1-r) \left[\bar{u}_S + \left(q - \frac{1}{2} \right) \Delta_{u,S}^{(1)} + \frac{1}{2} \left\{ \left(q - \frac{1}{2} \right)^2 - \frac{1}{4} \right\} \Delta_{u,S}^{(2)} \right] + r \left[\bar{u}_N + \left(q - \frac{1}{2} \right) \Delta_{u,N}^{(1)} + \frac{1}{2} \left\{ \left(q - \frac{1}{2} \right)^2 - \frac{1}{4} \right\} \Delta_{u,N}^{(2)} \right] \\ v(q, r) &= (1-q) \left[\bar{v}_W + \left(r - \frac{1}{2} \right) \Delta_{v,W}^{(1)} + \frac{1}{2} \left\{ \left(r - \frac{1}{2} \right)^2 - \frac{1}{4} \right\} \Delta_{v,W}^{(2)} \right] + q \left[\bar{v}_E + \left(r - \frac{1}{2} \right) \Delta_{v,E}^{(1)} + \frac{1}{2} \left\{ \left(r - \frac{1}{2} \right)^2 - \frac{1}{4} \right\} \Delta_{v,E}^{(2)} \right] \end{aligned}$$

where u, v are respectively the horizontal and vertical velocity components, N, S, E, W is the standard compass convention for 2D grids, q, r are respectively the horizontal and vertical local coordinates (e.g., $q = 0$ on the West face and $q = 1$ on the East

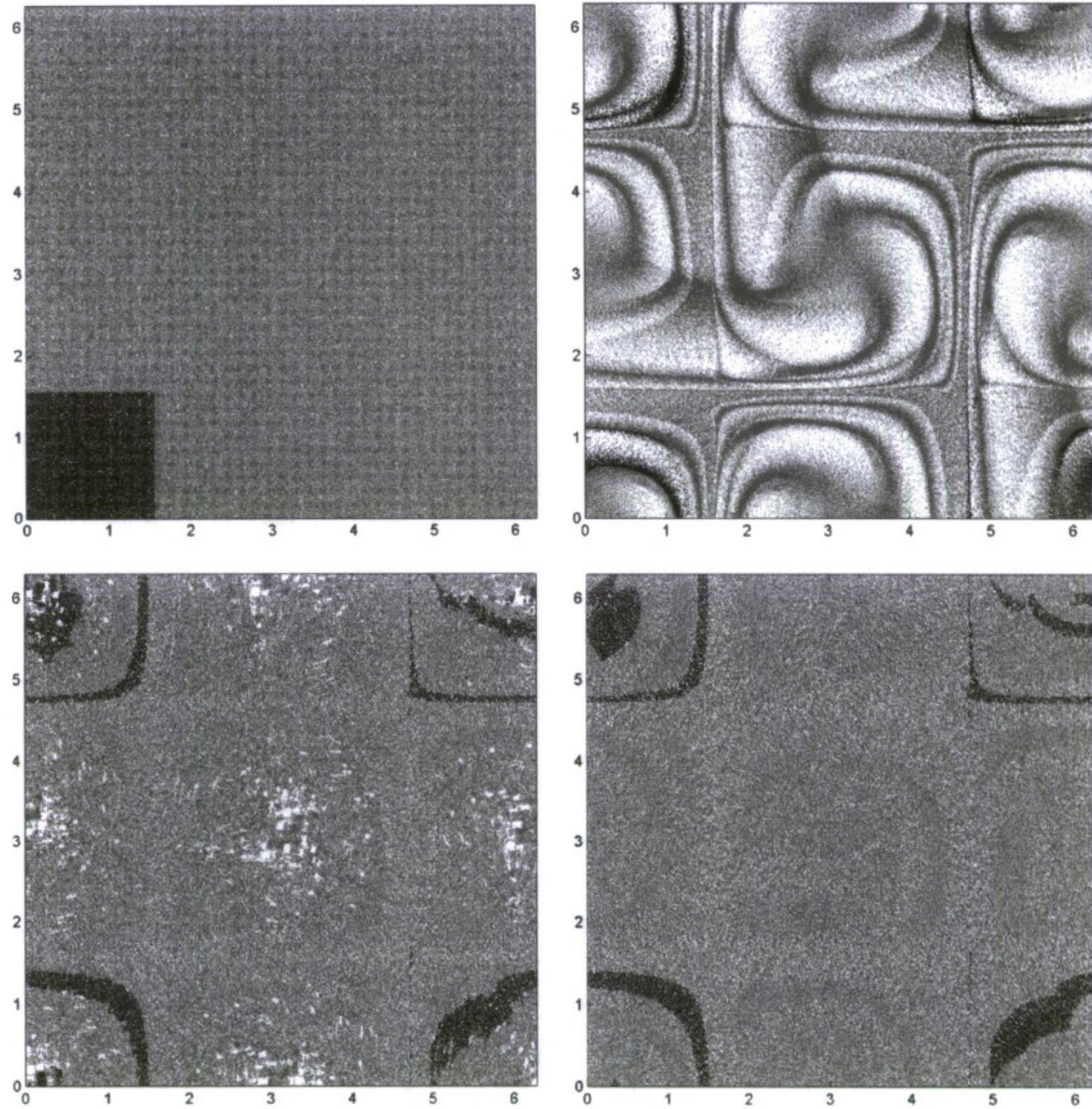


Fig. 1. Comparison between the performance of the bilinear and PERM velocity interpolation schemes, and between the RK2 and MRK2 time-stepping schemes. We consider the 2D, periodic incompressible flow field given by Eqs. (16) and (17) in Section 3. 409,600 particles are initially uniformly spaced inside the domain (top left). Each particle is represented by a light grey dot, except for those initially in the bottom left corner, which are dark grey, for visualization purposes. The particles are advected using different velocity interpolation and time integration schemes. Because the test flow is incompressible and the particles are initially uniformly distributed, they should remain so. Top right: final particle distribution using bilinear interpolation on a 4×4 grid and RK2 time integration. Bottom left: final particle distribution using PERM interpolation on a 4×4 grid and RK2 time integration. Bottom right: final particle distribution using PERM interpolation on a 4×4 grid and MRK2 time integration. It can be seen that the combination of PERM interpolation and MRK2 time stepping performs best at preserving the uniformity of the particle distribution.

face. Note that q as used here is different from the mean particle mass density defined in Eq. (2)), and $\bar{u}_S, \Delta_{u,S}^{(1)}, \Delta_{u,S}^{(2)}$, etc. are parameters which are determined by an algorithm described in [1].

Some of the important properties of PERM are enumerated below. They indicate why a standard time-stepping scheme, such as RK2, does not perform well with this particular velocity reconstruction. For simplicity, we consider here a grid composed of 2D or 3D cubes, of side Δx .

1. For a given velocity component, in the component direction, the reconstructed field is continuous, piecewise parabolic, and second-order accurate with respect to Δx .
2. The flux of the reconstructed velocity field through any given grid cell face is identically equal to the flux implied by the FV face-normal velocity.
3. For a given velocity component, in the component-normal directions, the reconstructed field is piecewise continuous, piecewise linear, and second-order accurate with respect to Δx .

4. The magnitudes of the velocity discontinuities implied by Property 3 are proportional to Δx^2 .
5. The divergence of the reconstructed velocity field is bi- or tri-linear, piecewise continuous, and second-order accurate with respect to Δx .
6. The magnitudes of the divergence discontinuities implied by Property 5 are proportional to Δx^2 .

It should be noted that, as described in [1], the PERM reconstruction scheme requires a Cartesian grid (either uniform or non-uniform in each coordinate). It is also possible to extend PERM to cylindrical coordinate grids.

Furthermore, it should be noted that for a velocity field with the functional form of PERM it is not possible to integrate Eq. (1) analytically – to see why this is so, note that any bi- or tri-linear velocity field is a particular case of a PERM field, and Eq. (1) cannot be integrated exactly for a general bi- or tri-linear velocity field, even if it is time-independent (the differential equation of the Lorentz attractor [6], for example, is a particular case of a tri-linear velocity field). Therefore, we have to utilize a numerical time-integration scheme for the integration of Eq. (1) – a natural candidate is second-order Runge–Kutta (RK2).

However, second-order time accuracy for the RK2 scheme requires that the velocity field is everywhere continuous, and differentiable (in both space and time) everywhere except on a set of measure zero. Therefore, due to the discontinuities in the PERM reconstructed velocity, an RK2 solution is only first-order accurate in time, for a fixed grid size. Also, applying RK2 to a discontinuous velocity field leads to the violation of an important continuity principle, namely: if two particles are initially infinitesimally close, they remain so. These two statements are demonstrated in the next section.

On the other hand, Items 4 and 6 above imply that for a fine mesh the discontinuities in velocity and divergence, and their detrimental effect on the performance of RK2, are negligible. More specifically, if we decrease both the grid size and time step, keeping the Courant number fixed, a solution which combines PERM and RK2 is second-order accurate. Nevertheless, it is often the case in large eddy simulation/filtered density function (LES/FDF) methods that the grid used provides only marginal resolution of the filtered velocity field, and hence the discontinuities in the PERM reconstructed velocity field should not be neglected.

2. Examination of RK2 for discontinuous velocity fields

Let us begin with a simple example of the problems that we encounter when we use RK2 on a discontinuous velocity field. Instead of thinking about a grid, consider an infinite, time-independent velocity field in 2D, which has the following form:

$$U(x, y) = 1, \quad (7)$$

$$V(x, y) = \begin{cases} 0, & \text{for } x < 0, \\ 1, & \text{for } x \geq 0. \end{cases} \quad (8)$$

Here, we can think of the regions $x < 0$ and $x > 0$ as two grid cells, with the region $x = 0$ as the face between them. Note that this velocity field has the kind of discontinuity which can be caused by PERM: U is continuous in the x -direction, and V is continuous in the y -direction, but V is not continuous in the x -direction, its component-normal direction. Now, consider two particles at time $t = 0$: one at $(X_{1,0}, Y_{1,0}) = (-\Delta t - \epsilon, 0)$ and the other at $(X_{2,0}, Y_{2,0}) = (-\Delta t + \epsilon, 0)$, where $0 < \epsilon \ll \Delta t$. An RK2 step of length Δt has the form:

$$\mathbf{X}^{(1)} = \mathbf{X}_0 + \Delta t \mathbf{U}(\mathbf{X}_0, 0), \quad (9)$$

$$\mathbf{X}_{\Delta t}^{\text{RK2}} = \mathbf{X}_0 + \frac{1}{2} \Delta t (\mathbf{U}(\mathbf{X}_0, 0) + \mathbf{U}(\mathbf{X}^{(1)}, \Delta t)). \quad (10)$$

Substituting their initial positions for \mathbf{X}_0 in Eqs. (9) and (10), we determine that the final positions of the two particles, after one RK2 step of length Δt , are $(X_{1,\Delta t}^{\text{RK2}}, Y_{1,\Delta t}^{\text{RK2}}) = (-\epsilon, 0)$ and $(X_{2,\Delta t}^{\text{RK2}}, Y_{2,\Delta t}^{\text{RK2}}) = (\epsilon, \Delta t/2)$. On the other hand, with perfect time advancement, the final particle positions at time Δt are $(X_{1,\Delta t}, Y_{1,\Delta t}) = (-\epsilon, 0)$ and $(X_{2,\Delta t}, Y_{2,\Delta t}) = (\epsilon, \epsilon/2)$. Therefore, we can see that the RK2 position of the second particle differs from the correct position by a distance of $(\Delta t - \epsilon)/2$. Keeping in mind that we set $\epsilon \ll \Delta t$, we have that this single time step introduces an $O(\Delta t)$ error in the final position of the second particle. Therefore, RK2 is first-order accurate in time overall, and for a time step that crosses a discontinuity it is zeroth-order accurate (in the sense that if all time steps introduced an error of the same magnitude as that introduced by a discontinuity-crossing step, the overall error in the final position of a particle would be $O(\Delta t^0)$).

Furthermore, if we take the limit as $\epsilon \rightarrow 0$, we can see that the distance between the initial positions of the two particles goes to zero, but the distance between the final positions after the RK2 step goes to $\Delta t/2$. As previously mentioned, this is a violation of a fundamental continuity principle, namely that if $\mathbf{X}(\mathbf{Y}, t)$ is the Lagrangian mapping between a particle's initial and final positions (i.e., if a particle is at \mathbf{Y} at time 0, it will be at $\mathbf{X}(\mathbf{Y}, t)$ at time t), then $\mathbf{X}(\mathbf{Y}, t)$ is continuous in both \mathbf{Y} and t , except at regions where there is a velocity discontinuity and the face-normal velocity is zero.

The considerable RK2 position error for the second of the two particles is introduced by the following fact: even though under perfect time advancement the second particle is in the region $x > 0$ only for a time $\epsilon \ll \Delta t/2$, the corrected velocity of the RK2 step $(\mathbf{U}(\mathbf{X}_{2,0}, 0) + \mathbf{U}(\mathbf{X}_2^{(1)}, \Delta t))/2$, is the average velocity that the particle would experience if it were in that region for a time $\Delta t/2$. In other words, RK2 does not account for how much time a particle spends on each side of a discontinuity. This is the motivation for the Multi-Step RK2 scheme, which we now describe in detail.

2.1. Description of MRK2

In this section, we present a description of a Multi-Step RK2 time step. We consider a particle that is initially at the position \mathbf{X}_0 at time 0, and which is to be advected for a time step of length Δt . For the moment, let us consider the case in which there is only one velocity discontinuity, as in the example above.

First, we take an RK2 predictor step, according to Eq. (9):

$$\mathbf{X}^{(1)} = \mathbf{X}_0 + \Delta t \mathbf{U}(\mathbf{X}_0, 0).$$

If \mathbf{X}_0 and $\mathbf{X}^{(1)}$ are in the same cell, then we take the remainder of a standard RK2 time step, according to Eq. (10), which gives the final result:

$$\mathbf{X}_{\Delta t}^{\text{MRK2}} = \mathbf{X}_{\Delta t}^{\text{RK2}} = \mathbf{X}_0 + \Delta t (\mathbf{U}(\mathbf{X}_0, 0) + \mathbf{U}(\mathbf{X}^{(1)}, \Delta t)) / 2.$$

Otherwise, let \mathbf{X}' be the point where the ray from \mathbf{X}_0 to $\mathbf{X}^{(1)}$ first intersects a cell face. For Cartesian, cylindrical and unstructured tetrahedral grids, in order to determine \mathbf{X}' we have to identify the faces of the current grid cell, each of which is a piece of a plane or a cylinder in 2D or 3D, and identify the points where the ray from \mathbf{X}_0 to $\mathbf{X}^{(1)}$ crosses each of them, if it does (a simple problem in analytic geometry). Out of these points, \mathbf{X}' is the one closest to \mathbf{X}_0 .

We make the following second-order accurate estimate for the time, Δt_1 , that it takes for the particle to reach this discontinuity:

$$\Delta t_1 = \Delta t \|\mathbf{X}' - \mathbf{X}_0\| / \|\mathbf{X}^{(1)} - \mathbf{X}_0\|, \quad (11)$$

where $\|\cdot\|$ denotes the 2-norm. Next, we break up the RK2 predictor step into two substeps. The first predictor substep, from time 0 to Δt_1 , and from \mathbf{X}_0 to \mathbf{X}' , accounts for the advection of the particle before it reaches the discontinuity. The second predictor substep, which accounts for advection after the particle crosses the discontinuity, takes the particle from time Δt_1 to Δt and from \mathbf{X}' to $\mathbf{X}^{(2)}$, where $\mathbf{X}^{(2)}$ is given by

$$\mathbf{X}^{(2)} = \mathbf{X}' + (\Delta t - \Delta t_1) \mathbf{U}^+(\mathbf{X}', 0). \quad (12)$$

There are two possible definitions of velocity at \mathbf{X}' , where the velocity field is discontinuous. The value $\mathbf{U}^+(\mathbf{X}', 0)$ denotes the velocity experienced by the particle after it has crossed the discontinuity. Similarly, below we use $\mathbf{U}^-(\mathbf{X}', 0)$ to denote the velocity experienced by the particle before it crosses the discontinuity. (We have assumed, for the moment, that the particle does not cross another discontinuity between \mathbf{X}' and $\mathbf{X}^{(2)}$.)

Next, we make second-order linear approximations in time to estimate the velocities at \mathbf{X}' at the intermediate time Δt_1

$$\mathbf{U}^-(\mathbf{X}', \Delta t_1) \approx \hat{\mathbf{U}}^-(\mathbf{X}', \Delta t_1) = [(\Delta t - \Delta t_1)/\Delta t] \mathbf{U}^-(\mathbf{X}', 0) + [\Delta t_1/\Delta t] \mathbf{U}^-(\mathbf{X}', \Delta t), \quad (13)$$

$$\mathbf{U}^+(\mathbf{X}', \Delta t_1) \approx \hat{\mathbf{U}}^+(\mathbf{X}', \Delta t_1) = [(\Delta t - \Delta t_1)/\Delta t] \mathbf{U}^+(\mathbf{X}', 0) + [\Delta t_1/\Delta t] \mathbf{U}^+(\mathbf{X}', \Delta t). \quad (14)$$

Finally, we calculate the corrected velocities for each of the two substeps, and obtain the final particle position

$$\mathbf{X}_{\Delta t}^{\text{MRK2}} = \mathbf{X}_0 + (\Delta t_1/2)(\mathbf{U}(\mathbf{X}_0, 0) + \hat{\mathbf{U}}^-(\mathbf{X}', \Delta t_1)) + ((\Delta t - \Delta t_1)/2)(\hat{\mathbf{U}}^+(\mathbf{X}', \Delta t_1) + \mathbf{U}(\mathbf{X}^{(2)}, \Delta t)). \quad (15)$$

As already mentioned, for a particle which crosses the discontinuity, we break up the time step into two substeps. The two terms added to \mathbf{X}_0 in Eq. (15) are respectively the contributions of each of those two substeps to the advancement of the particle. For simplicity's sake, the algorithm presented above allows for two substeps at most, and can therefore deal with at most one velocity discontinuity crossed by a particle during a time step. By allowing for a greater number of substeps (e.g., breaking up the substep from Δt_1 to Δt into two substeps if the ray from \mathbf{X}' to $\mathbf{X}^{(2)}$ crosses another discontinuity), the algorithm is extended to deal with an arbitrary number of discontinuities crossed by a particle in one time step.

Below, we make a few important observations about MRK2:

1. The MRK2 procedure is almost the same as taking two RK2 steps – one from 0 to Δt_1 and one from Δt_1 to Δt – with the one difference being that the MRK2 procedure does not require knowledge of the velocity field at the intermediate time Δt_1 , and uses instead a linear interpolation in time between the velocity fields at time 0 and Δt . This difference is essential in an LES/FDF context, because during each time step a fraction, approximately equal to the Courant number, of the total number of particles in the domain cross a cell face. For a typical LES/FDF calculation with 10^7 particles and a Courant number of 0.1, this means that for each time step there would be approximately 10^6 particles crossing a cell face, each at a different intermediate time Δt_1 . It would be extremely inefficient, if not infeasible, to calculate the whole reconstructed velocity field at each of the (of order 10^6) intermediate times. Instead, MRK2 uses just two fields to obtain the needed local information with the required accuracy.
2. For a fixed grid size, and subject to a condition which is described in the next item, it can be shown analytically that an MRK2 step which crosses a discontinuity introduces an $O(\Delta t^2)$ error in the final particle position, and preserves the continuity of the Lagrangian mapping $\mathbf{X}(\mathbf{Y}, \Delta t)$. Therefore, MRK2 preserves continuity (in a restricted sense) and is second-order accurate in time, since the number of discontinuities crossed by a particle does not increase with decreasing time step.

3. The condition necessary for Item 2 is that the velocity normal to a face (discontinuity) is not identically zero. MRK2 does not preserve the continuity of $\mathbf{X}(\mathbf{Y}, \Delta t)$ where the face-normal velocity is zero. To see this, consider a velocity field similar to the example at the beginning of Section 2, this time with $U(x, y) = 0$, and consider two particles: one at $(X_{1,0}, Y_{1,0}) = (-\epsilon, 0)$ and the other at $(X_{2,0}, Y_{2,0}) = (\epsilon, 0)$. The result of an MRK2 time step is the same as that of an RK2 time step, and of perfect time advancement: $(X_{1,\Delta t}, Y_{1,\Delta t}) = (-\epsilon, 0)$ and $(X_{2,\Delta t}, Y_{2,\Delta t}) = (\epsilon, \Delta t)$. Taking limits as $\epsilon \rightarrow 0$, we can see why continuity is violated. Note that this is a property of the particular velocity field considered, not a shortcoming of MRK2 (i.e., even with perfect time advancement there is a continuity violation).
4. The MRK2 procedure is applicable to a wide variety of grids – it has only two grid-dependent aspects, namely the evaluation of the interpolated velocity at an arbitrary point in space, and the determination of the point \mathbf{X}' where the ray from \mathbf{X}_0 to $\mathbf{X}^{(1)}$ first intersects a cell face. The first of these aspects, the ability to evaluate interpolated velocity at an arbitrary point, is a general requirement for any reasonable velocity interpolation scheme. The second aspect, the ability to determine efficiently \mathbf{X}' , depends on the grid geometry and, as mentioned in the description of MRK2, reduces to a set of simple analytic geometry problems, such as finding the intersection of a ray with a plane (or cylinder). Therefore, in addition to Cartesian and cylindrical grids, MRK2 in itself is also applicable all grids with planar or cylindrical cell faces (e.g., unstructured tetrahedral grids). However, we should also keep in mind that the PERM velocity interpolation scheme, which is the primary motivation for the modification from RK2 to MRK2, has currently been developed only for Cartesian and cylindrical grids.

3. Comparison between the performance of RK2 and MRK2 when applied to a PERM reconstructed velocity field

In this section, we apply both RK2 and MRK2 to a 2D test problem, and compare the performance of the two time-stepping schemes based on three criteria: preservation of continuity, accuracy relative to perfect time advancement, and the maintaining of a consistent subgrid particle distribution.

We use the following problem framework: we have a 2D domain, $[0, 2\pi] \times [0, 2\pi]$, with periodic boundary conditions. We consider two 2D periodic flows. Flow 1 is incompressible, given by the formula

$$U(x, y, t) = 1 - 2 \cos(x - t) \sin(y - t), \quad (16)$$

$$V(x, y, t) = 1 + 2 \sin(x - t) \cos(y - t). \quad (17)$$

Flow 2 is compressible, given by

$$U(x, y, t) = 1 - 2 \cos(x - t) \sin(y - t) + \frac{1}{2} \sin(x) \cos(2t), \quad (18)$$

$$V(x, y, t) = 1 + 2 \sin(x - t) \cos(y - t) + \frac{1}{2} \sin(y) \cos(2t). \quad (19)$$

Streamline plots of these two test flows, for $t = 0$, are shown in Fig. 2.

In order to compute the reconstructed field, the PERM reconstruction scheme uses values of U (according to Eq. (16) or (18)) at the centers of the vertical cell faces, and values of V (according to Eq. (17) or (19)) at the centers of the horizontal cell faces – this simulates FV velocity information. Once the subgrid velocity is reconstructed by PERM, the respective time advancement scheme is used to advect the particles. The time step Δt is directly proportional to the Courant number (C), which is defined here as

$$C = \max(\max(U(x, y, t)\Delta t/\Delta x), \max(V(x, y, t)\Delta t/\Delta x)), \quad (20)$$

where Δx is the side of a grid cell, and the latter two maxima are over x, y, t .

3.1. Preservation of continuity, and a qualitative analysis of particle distributions

Here, we present results for the incompressible Flow 1, Eqs. (16) and (17). One of the beneficial properties of PERM is that if the velocity field is divergence free at the FV level, then the subgrid reconstructed velocity is also divergence free. Therefore, applying PERM to Flow 1, we obtain a subgrid velocity field that is divergence free, and so (with perfect time advancement) a particle distribution which is initially uniform remains uniform.

Here, we advect 409,600 particles which are initialized in the following manner: the domain is broken up into 640×640 squares of equal size, and a single particle is placed randomly, with uniform probability density, in each square. This allows for an initial particle distribution which is both very uniform and does not degenerate when a large value of strain is applied to it. Note that the number of particles that we are using is extremely large – 25,600 particles per cell, for a 4×4 grid. Naturally, in practical LES/FDF applications this number is much smaller. The reason why we are using so many here is for the reader to be able to better visualize the mappings $\mathbf{X}(\mathbf{Y}, t)$ between initial and final particle positions. In the following figures, each of the particles is shown as a single light grey dot, except for those which are initially in the region $[0, \pi/2] \times [0, \pi/2]$, at the lower-left corner. These particles are dark grey, in order to help visualize the strain of the particle distribution.

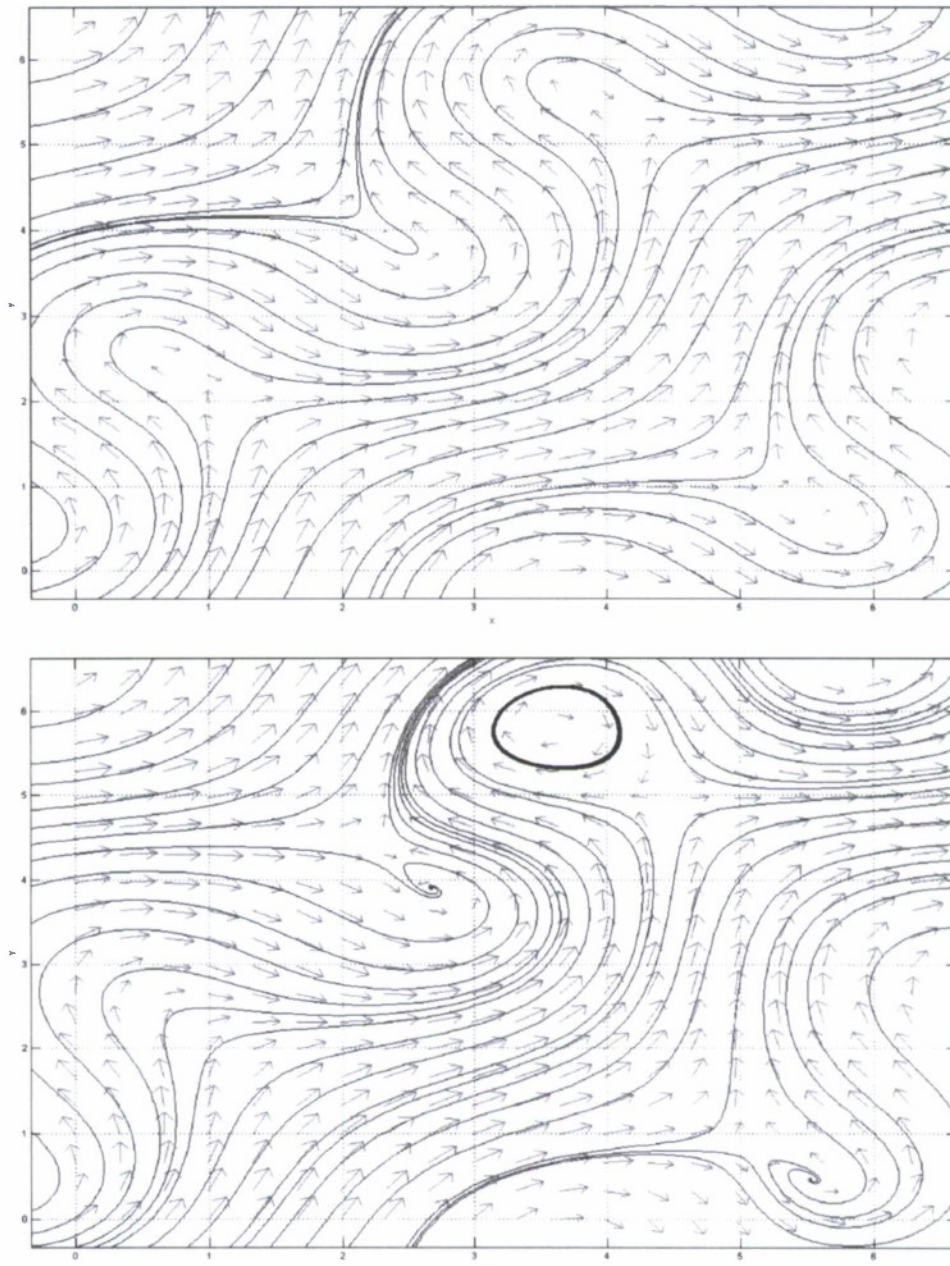


Fig. 2. Top: streamlines, at $t = 0$, of the incompressible Flow 1 (Eqs. (16) and (17)). Bottom: streamlines, at $t = 0$ of the compressible Flow 2 (Eqs. (18) and (19)).

Fig. 3 shows results for a 4×4 grid, with $C = 1$. We note that this is a rather large Courant number – it is used mainly to emphasize the effects of both time advancement schemes. After a single time step, we can see that the RK2 distribution (top left of Fig. 3) has considerable voids where there are no particles at all – this indicates that the mapping $\mathbf{X}(\mathbf{Y}, \Delta t)$ is not surjective (onto), since there are values of \mathbf{X} which cannot be attained for any value of \mathbf{Y} . We can also see regions in the RK2 distributions where the particles are twice as dense – this indicates that the mapping $\mathbf{X}(\mathbf{Y}, \Delta t)$ is not injective (one-to-one), since regions which were initially separate are mapped on top of each other. This is a serious problem – it introduces error in the subgrid particle distribution (as we will see later on) and violates the fundamental principle that for a periodic flow $\mathbf{X}(\mathbf{Y}, \Delta t)$ is both injective and surjective.

A single MRK2 time step, too, has these problems, but to a much lesser extent – we can see (from the top right of Fig. 3) four elongated gaps where there are no particles, but the size of these gaps is much smaller than the size of the holes in the particle distribution created by RK2. These gaps in the MRK2 distribution are to be expected – they correspond to regions where the face-normal velocity is zero, as explained in Section 2. Comparing the particle distributions after one flow-through

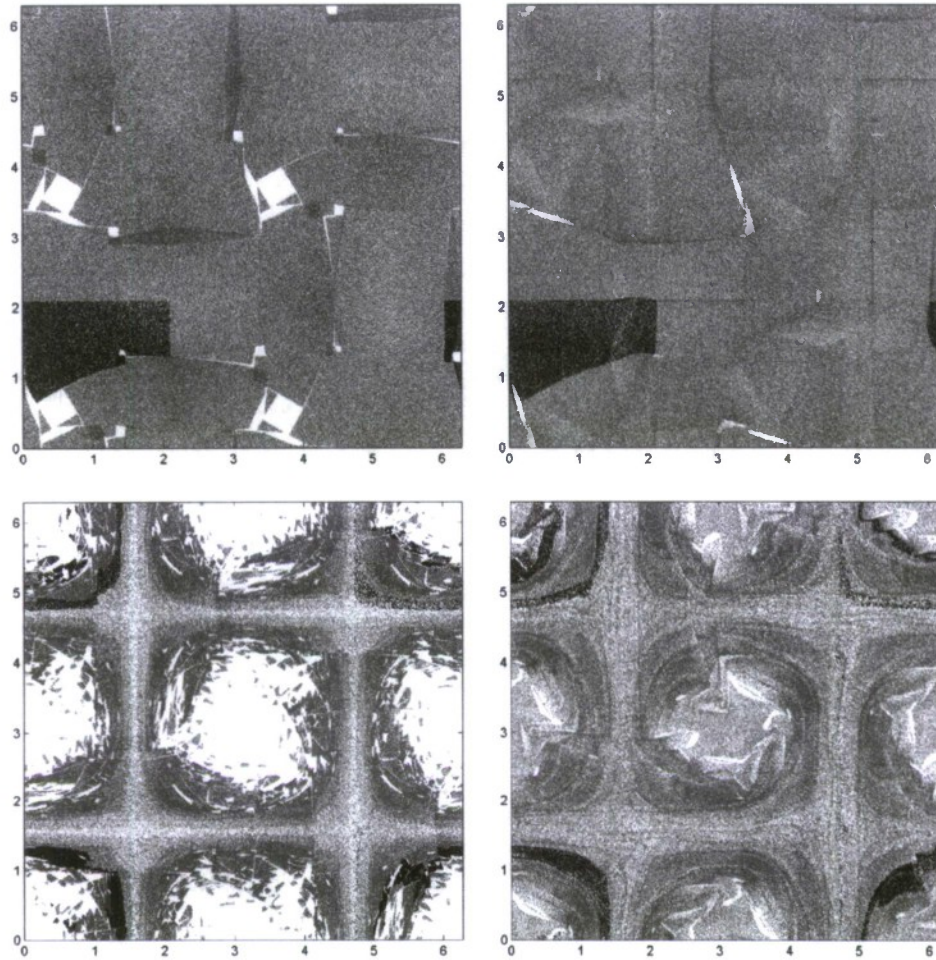


Fig. 3. Particle distributions in Flow 1 for a 4×4 grid, $C = 1$. Top left: RK2, one time step ($\Delta t = 0.448$); top right: MRK2, one time step; bottom left: RK2, one flow-through time (12 time steps); bottom right: MRK2, one flow-through time. The dark grey particles are those that are in the lower-left corner of the domain at $t = 0$.

time (12 time steps), we can see the same differences but with greater magnitude. Whereas, MRK2 does not preserve the uniformity of the particle distribution very well, it does much better than RK2, where there are considerably larger void regions.

Fig. 4 shows results for the same value of the Courant number, $C = 1$, but for a finer 8×8 grid. Because the magnitudes of the discontinuities in PERM are $O(\Delta x^2)$ [1], the velocity discontinuities in this case are theoretically smaller by a factor of four, and RK2 does almost as well as MRK2.

Fig. 5 shows results for a 4×4 grid, with a smaller Courant number, $C = 0.25$. We can again see that RK2 does not preserve continuity very well – there are noticeable voids in the RK2 distribution, both after one time step and after one flow-through time. Although we know theoretically that there are also voids in the MRK2 distributions, these cannot be perceived on the plots. We also note that MRK2 performs better at preserving the sharp interface between the light and dark grey regions.

Fig. 6 shows results for an 8×8 grid, $C = 0.25$. We cannot perceive a difference between the two particle distributions, which suggests that, due to the smaller value of velocity discontinuities, the performance of RK2 is similar to that of MRK2.

From these comparisons of particle distributions produced by RK2 and MRK2, we conclude that when the velocity discontinuities yielded by the reconstruction are considerable (as for the 4×4 grid), MRK2 performs better than RK2 at preserving the continuity of the particle distribution and the consistency between the subgrid particle distribution and the LES filtered density.

3.2. Accuracy relative to perfect time advancement

As we are focused on developing and demonstrating an effective time advancement scheme for a given velocity reconstruction, we are interested in the error of a given solution relative to perfect time advancement. Since we do not have

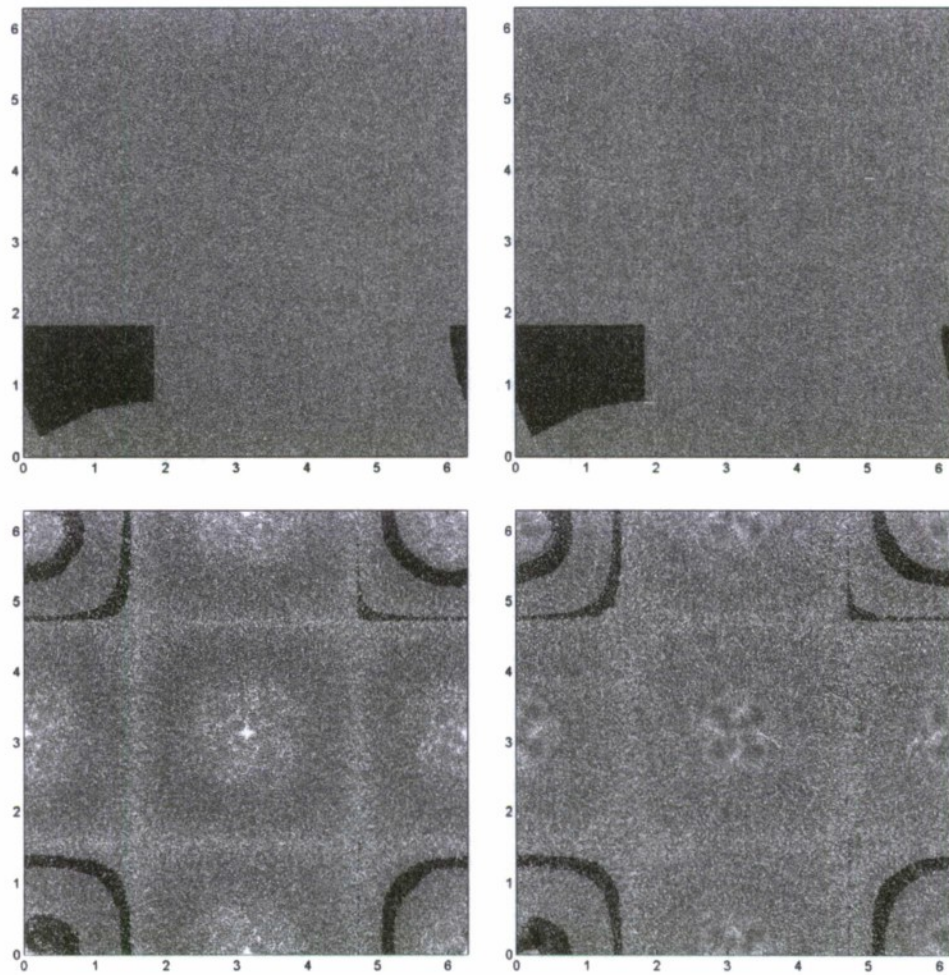


Fig. 4. Particle distributions in Flow 1 for an 8×8 grid, $C = 1$. Top left: RK2, one time step ($\Delta t = 0.224$); top right: MRK2, one time step; bottom left: RK2, one flow-through time (24 time steps); bottom right: MRK2, one flow-through time. The dark grey particles are those that are in the lower-left corner of the domain at $t = 0$.

an exact perfect time advancement solution, we use instead an MRK2 solution with a very low Courant number ($C = 1/512$) as an approximation.

First of all, we consider position error. We use $N = 256$ particles, uniformly distributed across the domain at time 0. We denote by $\mathbf{Y}^{(i)}$ the initial position of the i th particle, and we denote by $\mathbf{X}^{\text{RK2}}(\mathbf{Y}^{(i)}, t)$, $\mathbf{X}^{\text{MRK2}}(\mathbf{Y}^{(i)}, t)$, and $\mathbf{X}(\mathbf{Y}^{(i)}, t)$ the corresponding Lagrangian position mappings yielded by RK2, MRK2 and perfect time advancement, respectively. The position error of a given RK2 solution is then defined as

$$\epsilon_x^{\text{RK2}} = \frac{1}{N} \left(\sum_{i=1}^N \|\mathbf{X}^{\text{RK2}}(\mathbf{Y}^{(i)}, t) - \mathbf{X}(\mathbf{Y}^{(i)}, t)\| \right). \quad (21)$$

The MRK2 position error is defined analogously. As we already mentioned, it can be shown analytically that, with Δt being the length of the time step, the RK2 position error is of order $O(\Delta t)$, and the MRK2 position error is of order $O(\Delta t^2)$.

We also consider error of infinitesimal volume expansion (which we will refer to as dV error, for the sake of brevity). Note that we refer here to two-dimensional volume, i.e., area. For an infinitesimal material element whose initial volume is dV_0 , and whose initial position is \mathbf{Y} , the final volume, dV_t , is given by

$$dV_t = dV_0 \det \left(\frac{\partial X_j(\mathbf{Y}, t)}{\partial Y_k} \right), \quad (22)$$

where $\mathbf{X}(\mathbf{Y}, t)$ is the Lagrangian position mapping previously mentioned. This is the basis of the change of variables formula, which in this context tells us that the volume at time t of a set S is

$$V_t = \int_S \det \left(\frac{\partial X_j(\mathbf{Y}, t)}{\partial Y_k} \right) |d\mathbf{Y}|, \quad (23)$$

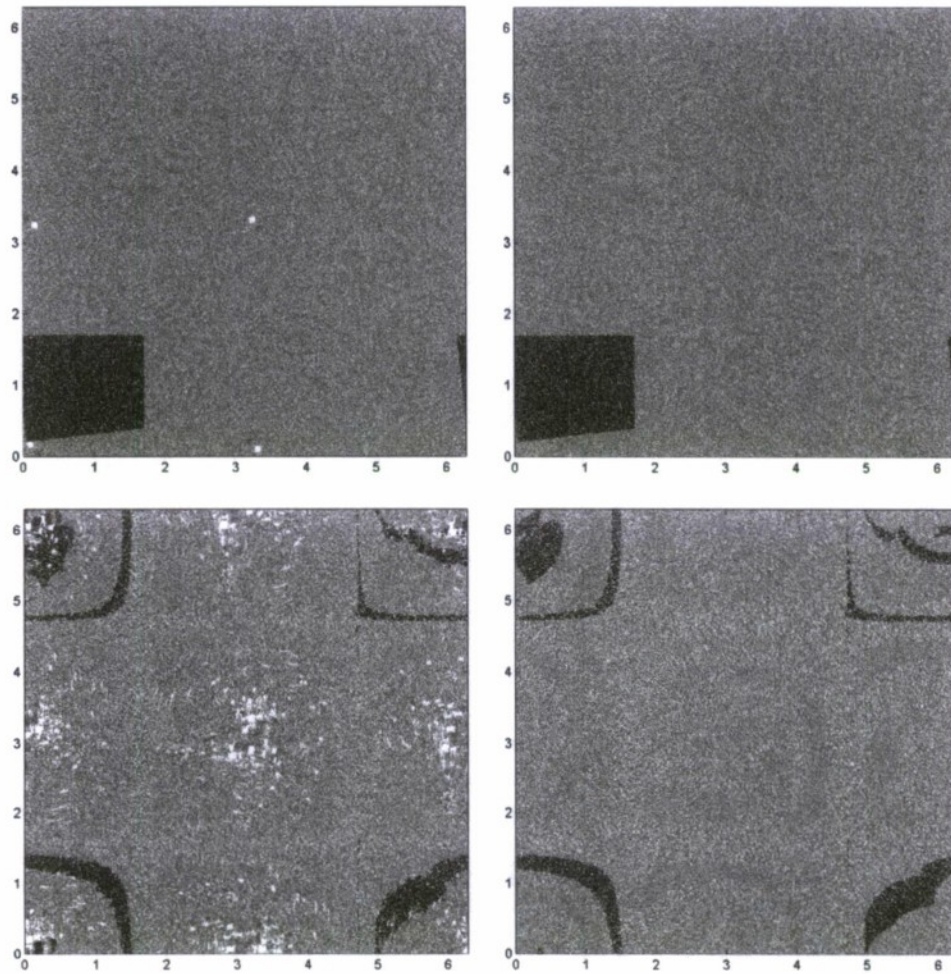


Fig. 5. Particle distributions in Flow 1 for a 4×4 grid, $C = 0.25$. Top left: RK2, one time step ($\Delta t = 0.112$); top right: MRK2, one time step; bottom left: RK2, one flow-through time (48 time steps); bottom right: MRK2, one flow-through time. The dark grey particles are those that are in the lower-left corner of the domain at $t = 0$.

provided that the mapping $\mathbf{X}(\mathbf{Y}, t)$ is one-to-one. Therefore, accurate values of $\det(\partial X_j / \partial Y_k)$ are essential for achieving an accurate subgrid particle distribution. We also note that $\mathbf{X}(\mathbf{Y}, t)$ may not be one-to-one if its continuity is violated (such as in Fig. 3, where particles are twice as dense in some places, because certain regions are mapped on top of each other), and therefore continuity of the position mapping, which is considered in the previous subsection, is just as essential for getting the right value of V_t as are accurate values of $\det(\partial X_j / \partial Y_k)$.

With this in mind, we define dV error of a given RK2 solution as

$$\epsilon_{dV}^{\text{RK2}} = \frac{1}{N} \sum_{i=1}^N \left| \det \left(\frac{\partial X_j^{\text{RK2}}(\mathbf{Y}^{(i)}, t)}{\partial Y_k} \right) - \det \left(\frac{\partial X_j(\mathbf{Y}^{(i)}, t)}{\partial Y_k} \right) \right|. \quad (24)$$

The MRK2 dV error is similarly defined. For RK2, it can be proven analytically that the dV error is $O(\Delta t^2)$ when the divergence of the PERM reconstructed field is continuous everywhere, and $O(\Delta t)$ when the divergence is discontinuous from cell to cell, which is the case for all compressible flows.

Here, we cannot calculate the necessary Jacobians exactly, but a sufficiently accurate numerical estimate which we use is

$$\det \left(\frac{\partial X_j}{\partial Y_k} \right) \approx A_t / A_0, \quad (25)$$

where A_0 is the initial area of a triangle initially of sides 10^{-8} formed by three particles at time 0, and A_t is the area of the triangle formed by those three particles at time t .

Here, we present results for the compressible Flow 2, Eqs. (18) and (19). Fig. 7 shows plots of position error and dV error for 4×4 and 8×8 grid solutions, with the Courant number ranging from 1 down to $1/32$. For both position error and dV error, RK2 exhibits first-order behavior, whereas MRK2 exhibits second-order behavior. This is consistent with previously

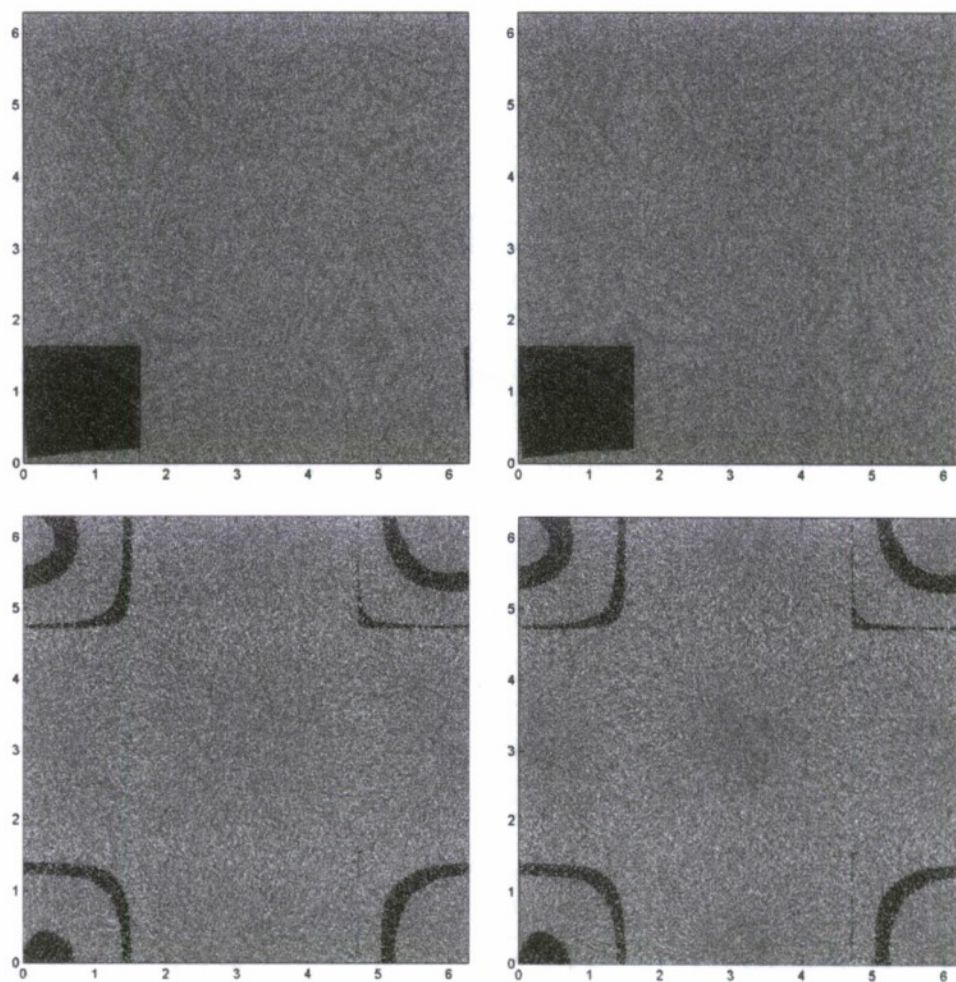


Fig. 6. Particle distributions in Flow 1 for an 8×8 grid, $C = 0.25$. Top left: RK2, one time step ($\Delta t = 0.056$); top right: MRK2, one time step; bottom left: RK2, one flow-through time (96 time steps); bottom right: MRK2, one flow-through time. The dark grey particles are those that are in the lower-left corner of the domain at $t = 0$.

stated analytic results, and it also indicates that for MRK2, dV error is $O(\Delta t^2)$ – a result which we have not been able to prove rigorously.

It should also be noted that, for larger values of C , MRK2 is computationally slower than RK2. In order to compare the efficiency of MRK2 with that of RK2, Fig. 8 shows plots of the position and dV errors from Fig. 7 versus simulation time, for a simulation with 1600 particles per cell, instead of just the 256 particles (for the entire domain) that we used to determine the errors. We use a larger number of particles here to ensure that the cost of all the operations other than particle advection (such as the determination of the PERM coefficients) is negligible.

From Fig. 8 we see that MRK2 becomes more efficient as the error (and hence the Courant number) decreases – for the 4×4 grid, MRK2 is more efficient for $C \leq 1/2$, and for the 8×8 grid, MRK2 is more efficient for $C \leq 1/4$. On the other hand, Fig. 8 takes into account only the computational cost for particle advection – if we also consider the cost of chemistry calculations, which is usually much higher than the cost of particle advection, we conclude that MRK2 may be more efficient than RK2 even for larger values of C .

Table 1 shows values of the error, as well as simulation time for a 1600-particles-per-cell simulation, for $C = 1$ and for $C = 0.25$. For both values of C , and for both meshes, MRK2 has a smaller position error: $\epsilon_x^{\text{MRK2}} / \epsilon_x^{\text{RK2}} < 0.69$. For both meshes, the MRK2 dV error is less than the RK2 dV error for $C = 0.25$, but for $C = 1$ and the 8×8 mesh, the MRK2 dV error is greater than the RK2 dV error. This, however, is not a major concern, because as we already noted, $C = 1$ is a very large value for the Courant number – in most applications, we expect a smaller value, such as 0.25, to be used.

3.3. Accuracy of the subgrid particle distribution

Previously, McDermott and Pope [1] have shown that a PERM reconstructed velocity field, with RK2 as the time-stepping scheme, performs much better than linear interpolation in maintaining a subgrid particle distribution which is consistent

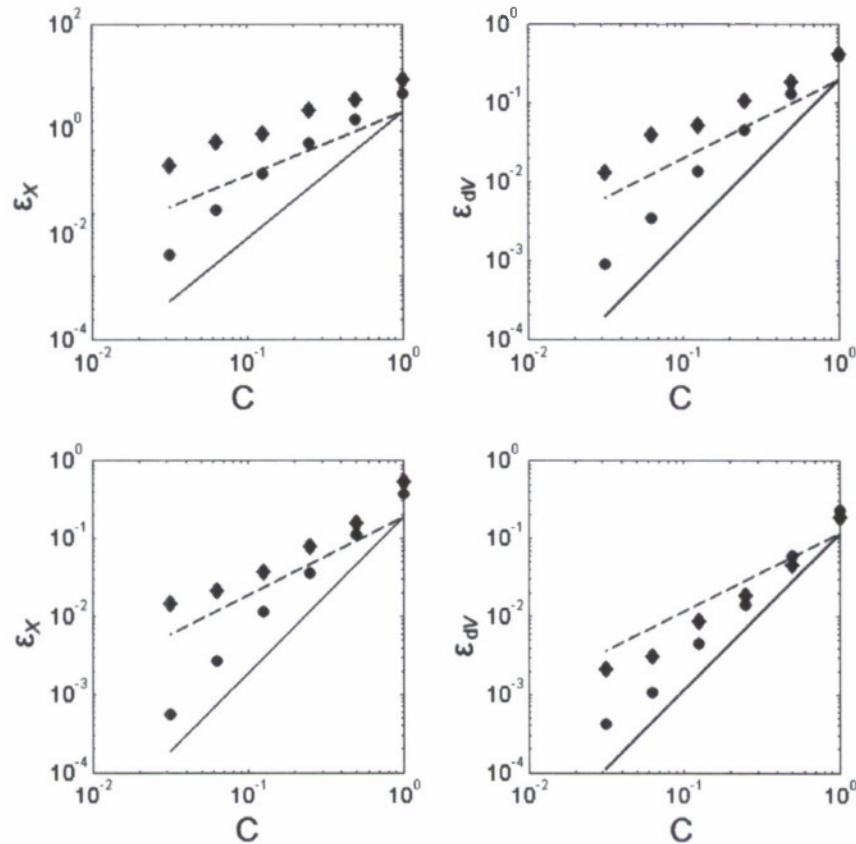


Fig. 7. Results for position and dV error in Flow 2 at $t = 8.97$. Top left: position error for a 4×4 grid; top right: dV error for a 4×4 grid; bottom left: position error for a 8×8 grid; bottom right: dV error for a 8×8 grid. The diamonds denote RK2 error, the circles denote MRK2 error. The dashed line indicates first-order convergence, and the solid line indicates second-order convergence.

with the LES filtered density. Here, we demonstrate that this consistency becomes even better when MRK2 is used as the time-stepping scheme.

For the present tests, we use the incompressible Flow 1, Eqs. (16) and (17). The particles are initialized in a manner similar to that in Section 3.1 (by breaking up the domain into as many squares as there are particles, and initializing a single particle randomly into each square). Then the mean particle mass density is initially the same everywhere in the flow, and it remains so under perfect time advancement, for a divergence-free velocity field such as the one we consider. Hence, the expected number of particles in a set S is directly proportional to the area of S .

We quantify the accuracy of the subgrid particle distribution in the following way: we break up the domain into equal sized squares, which we call sampling squares. We use sampling squares of three different sizes, with sides $\pi/4$, $\pi/8$, and $\pi/16$ (respectively $1/2$, $1/4$ and $1/8$ of the sidelength of a grid cell, for a 4×4 grid). At any given timestep, let N_i be the number of particles in the i th sampling square, let N_{mean} be the expected number of particles for a square of this size, and let N_{sq} be the number of sampling squares in the domain. The subgrid particle distribution error is then defined as

$$\epsilon_{\text{SG}} = \left(\sum_{i=1}^{N_{\text{sq}}} |N_i - N_{\text{mean}}| / N_{\text{mean}} \right) / N_{\text{sq}}. \quad (26)$$

This subgrid distribution error has two contributions: first, a probabilistic error, due to the random particle initialization; and, second, a bias error, due to the particle advection scheme (an example of this are the considerable voids in the particle distribution left by RK2 at $C = 1$). For this test flow, the PERM reconstructed velocity field has zero divergence, and therefore a perfect time advancement solution contains only the probabilistic component of the error. Therefore, we compare the subgrid distribution errors given by the MRK2, RK2 and perfect time advancement solutions, making the assumption that whatever is in excess of the perfect time advancement error is mostly bias error.

Fig. 9 shows results for 65,536 particles, $C = 0.25$ and a 4×4 grid. As may be seen, the MRK2 subgrid distribution error is much closer to the perfect time advancement error than is the RK2 error. From this we deduce that, for the coarse 4×4 grid, the bias error caused by MRK2 is smaller than the bias error caused by RK2.

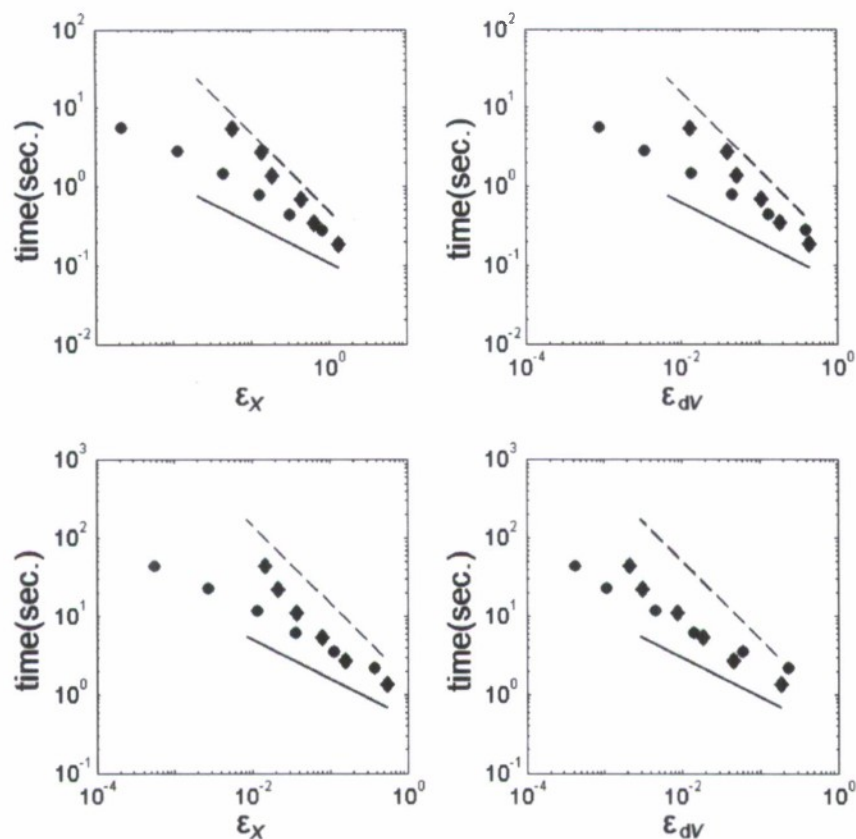


Fig. 8. Comparison between the efficiency of MRK2 and RK2, based on position and dV error, and the computational cost of particle advection for a 1600-particles-per-cell simulation of Flow 2 at $t = 8.97$. Top left: position error for a 4×4 grid; top right: dV error for a 4×4 grid; bottom left: position error for a 8×8 grid; bottom right: dV error for a 8×8 grid. The diamonds denote RK2 error, the circles denote MRK2 error. The dashed line indicates first-order convergence, and the solid line indicates second-order convergence.

Table 1

Summary of position and dV errors for Flow 2 at $t = 8.97$

Case	ϵ_x		ϵ_{dV}	
	RK2	MRK2	RK2	MRK2
$4 \times 4, C = 1$	1.32×10^0	8.17×10^{-1}	4.35×10^{-1}	3.97×10^{-1}
$4 \times 4, C = 0.25$	4.35×10^{-1}	1.29×10^{-1}	1.07×10^{-1}	4.56×10^{-2}
$8 \times 8, C = 1$	5.47×10^{-1}	3.80×10^{-1}	1.88×10^{-1}	2.33×10^{-1}
$8 \times 8, C = 0.25$	7.83×10^{-2}	3.55×10^{-2}	1.84×10^{-2}	1.41×10^{-2}

Fig. 10 shows results for 65,536 particles, $C = 0.5$ and a 8×8 grid. The time step is the same as for the results on Fig. 6, but the velocity field is better resolved by PERM. Here, the MRK2, RK2 and perfect time advancement errors are much closer together, and MRK2 does not provide a big advantage over RK2. Again, we observe that for a finer grid RK2 does not perform considerably worse than MRK2, because the discontinuities in velocity are smaller.

3.4. Computational cost

We have seen that MRK2 has superior accuracy than RK2, and has better performance in preserving the consistency between the subgrid particle distribution and the filtered LES density. One disadvantage that MRK2 has over RK2 is that it is slower – this was mentioned in Section 3.2, where we compared the efficiency of MRK2 with that of RK2.

For the well-optimized Fortran 90 implementation of MRK2 which we used to obtain the results in the previous sections, each additional substep after the first one costs approximately 1.5 times the cost of an RK2 step. In other words, if the total time for one RK2 time step for one particle is t_{step} , the total time for an MRK2 time step, for a particle which crosses n discontinuities, is approximately $t_{\text{step}}(1 + 1.5n)$. Therefore, for a flow in which each particle crosses one discontinuity per time

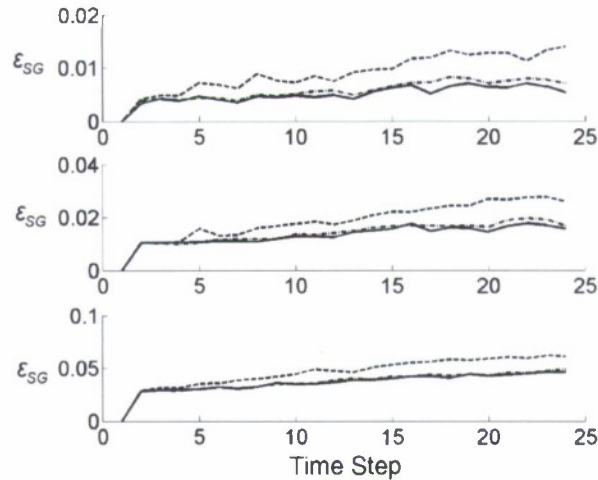


Fig. 9. Results for subgrid particle distribution error for Flow 1. $C = 0.25$, $(\Delta t = 0.112)$, 4×4 grid top: error for sampling squares of side $\pi/4$; middle: error for sampling squares of side $\pi/8$; bottom: error for sampling squares of side $\pi/16$. The errors for the RK2, perfect time advancement, and MRK2 solutions are shown respectively by the dashed, solid, and dash-dot curves.

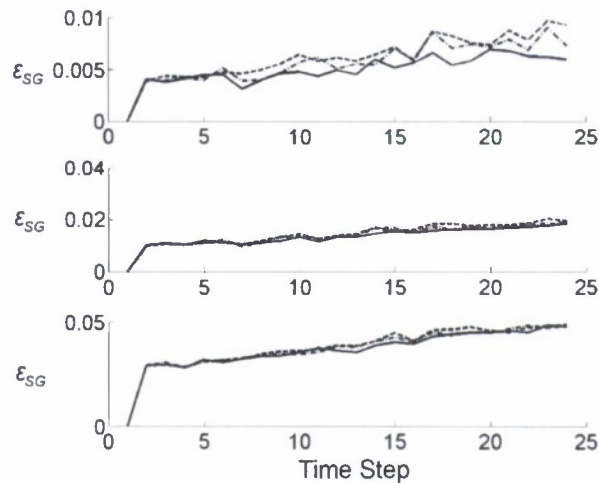


Fig. 10. Results for subgrid particle distribution error for Flow 1. $C = 0.5$, $(\Delta t = 0.112)$, 8×8 grid top: error for sampling squares of side $\pi/4$; middle: error for sampling squares of side $\pi/8$; bottom: error for sampling squares of side $\pi/16$. The errors for the RK2, perfect time advancement, and MRK2 solutions are shown respectively by the dashed, solid, and dash-dot curves.

step (hence requiring two substeps per time step) an MRK2 calculation would require 2.5 times more time than an RK2 calculation would.

Fortunately, in most flows of practical interest the number of particles which require two or more substeps is generally small. For the test cases from the previous sections, the MRK2 calculations have a 70% computational overhead at $C = 1$, and a 20% computational overhead at $C = 0.25$, relative to the RK2 calculations. For smaller values of C the computational overhead is even smaller, since the ratio between the number of particles which cross a discontinuity and the number of particles which do not cross one decreases with decreasing Courant number.

4. Conclusions

We have outlined a new time-stepping scheme, based on second-order Runge–Kutta, which is particularly suited for advection of a large number of particles through a discontinuous velocity field, such as the one yielded by the parabolic edge reconstruction method (PERM). We have demonstrated that the new scheme, MRK2, preserves better than RK2 the continuity of the Lagrangian mapping between initial and final positions. We have also shown that MRK2 is second-order accurate in time, as opposed to RK2, which is first-order accurate for a discontinuous velocity field. Additionally, we have shown that MRK2 preserves better than RK2 the consistency between the subgrid particle distribution and the LES filtered density.

On the other hand, we have seen that the advantages of MRK2 over RK2 diminish when a more refined grid is used for velocity reconstruction, and that MRK2 has a computational overhead relative to RK2 (20% at $C = 0.25$) which is not negligible. Therefore, whereas RK2 is sufficiently accurate (and faster) for problems with a fine mesh, it is preferable to use MRK2 in problems where the mesh provides only marginal resolution of the velocity, which is often the case in LES/FDF methods.

Finally, it should be noted that the main principle of MRK2 – breaking up a step into two or more substeps every time a velocity discontinuity is encountered – can be applied in a straightforward manner to time advancement schemes other than RK2. The Midpoint Euler scheme, for example, can be modified to deal with velocity discontinuities similarly to the way MRK2 does. This would be preferable in a situation where velocity information is known at the middle of the time step.

Acknowledgments

This work is supported by the Air Force Office of Scientific Research, Grant FA9550-06-1-0048. This work was performed while the second author held a National Research Council Postdoctoral Research Associateship at the National Institute of Standards and Technology.

References

- [1] R. McDermott, S.B. Pope, The parabolic edge reconstruction method (PERM) for Lagrangian particle advection, *Journal of Computational Physics* 227 (2008) 5447–5491.
- [2] M. Muradoglu, S.B. Pope, D.A. Caughey, The hybrid method for the PDF equations of turbulent reactive flows: consistency conditions and correction algorithms, *Journal of Computational Physics* 172 (2001) 841–878.
- [3] P. Jenny, S.B. Pope, M. Muradoglu, D.A. Caughey, A hybrid algorithm for the joint PDF equation of turbulent reactive flows, *Journal of Computational Physics* 166 (2001) 218–252.
- [4] Y.Z. Zhang, D.C. Haworth, A general mass consistency algorithm for hybrid particle/finite-volume PDF methods, *Journal of Computational Physics* 194 (2004) 156–193.
- [5] S.B. Pope, *Turbulent Flows*, Cambridge University Press, Cambridge, UK, 2000.
- [6] E.N. Lorenz, Deterministic nonperiodic flow, *Journal of the Atmospheric Sciences* 20 (1963) 130–141.